

Ternary Organic Solar cells incorporating Organic and Two-dimensional materials.

Pavlos E. Tzourmpakis



University of Crete

Department of Materials Science & Technology

Master Thesis

Heraklion, June 2017

Preface

The presented Master thesis was carried out at Nanomaterials and Organic Electronics Laboratory, TEI Crete, Heraklion and Institute of Electronic Structure and Laser (IESL) from September 2015 to June 2017 under supervision and guidance of Prof. George Kioseoglou (Department of Materials Science & Technology, UOC), Prof. Emmanuel Kymakis (TEI of Crete) and Prof. Konstantinos Petridis (TEI of Crete).

Abstract

Three different ternary bulk-heterojunction (BHJ) organic Photovoltaic (OPV) devices were systematically studied. First, a 2D-nanomaterial, (Tungsten Diselenide, WSe₂) and a small molecule (Compound T) were added into the PTB7:PC₇₁BM binary device, forming a Ternary device. A maximum PCE of 8.78% was achieved upon the incorporation of M-WSe₂ flakes having lateral size in the 30-50 nm range, which is one of highest PCE reported for OPVs with PTB7 as the polymer donor. The enhancement is primarily attributed to the synergistic effect of complementary absorption and charge transfer processes. Excitons can be also generated inside the M-WSe₂ nanoflakes, increasing the overall exciton generation due to the complementary absorption bands of PTB7 and WSe₂. Next, a conjugated small molecule 4,7-dithienbenzothiadiazole (T) was incorporated as the third component, PCE was improved by 5.5% reaching a maximum value of 8.11%, due to cascade charge transfer. Finally, the photovoltaic parameters of six novel Low Band gap (LBG) polymers were determined for the first time. In this context, RGO nanoflakes were incorporated to dope the most efficient LBG polymer among these, resulting to conductivity increase by 60% and a PCE of 4.5%, improved by 8.5%, compared to the reference cell. The improved conductivity was the motivation for a future hybrid integrated solar cell fabrication, where this ternary active layer would be undoubtedly applied as a second active material onto the highly efficient perovskite wide band gap layer.

Abbreviations and Symbols

OSCs	Organic Solar Cells
OPVs	Organic Photovoltaics
PV	Photovoltaic
DSSCs	Dye-sensitized solar cells
PSCs	Perovskite Solar cells
IHSC	Integrated hybrid solar cell
J_{sc}	Short Circuit Current Density
V_{oc}	Open Circuit Voltage
FF	Fill Factor
PCE	Power Conventional Efficiency
EQE	External Quantum Efficiency
IPCE	Incident photon to current conversion efficiency
IQE	Internal Quantum Efficiency
HTL/EBL	Hole transport layer/Electron blocking layer
ETL/HBL	Electron transport layer/Hole blocking layer
AL	Active layer
TCO	Transparent conducting oxide
PC ₇₁ BM	Phenyl-C71-butyric-acid-methyl-ester
PC ₆₀ BM	[6,6]-phenyl-C60-butyric acid methylester
CB	Chlorobenzene
ITO	Indium tin oxide
PEDOT:PSS	Poly(3,4-ethylenedioxythiophene) poly(styrenesulfonate)
PCs	Polycarbazoles
NS	Nanosheets
TMD	Transition metal dichalcogenide

Spiro-OMeTAD	2,2',7,7'-tetrakis[N,N-di(4-methoxyphenyl)amino]-9,9'-spirobifluorene
MAPbI ₃	Methylammonium lead iodide
FAPbI ₃	Formamidinium lead iodide
L _D	Diffusion length
VTE	Vacuum Thermal Evaporation
TFD	Thin Film Deposition
HOMO	Highest occupied molecular orbital
LUMO	Lowest unoccupied molecular orbital
EA	Electron affinity
VB	Valence band
CB	Conduction band
E _g	Band gap
OPDs	Organic Photodetectors
PTB ₇	Poly({4,8-bis[(2-ethylhexyl)oxy]benzo-[1,2-b:4,5 b']dithiophene-2,6-diyl}){3 fluoro - 2-[(2ethylhexyl)carbonyl]thieno -[3,4-b]thiophenedi-yl)}
MoS ₂	Molybdenum disulfide
WS ₂	Tungsten disulfide
WSe ₂	Tungsten diselenide
DPP	Diketopyrrolopyrrole
DPPTT-T	Thieno[3,2-b]thiophene–diketopyrrolopyrrole
DPP4T	cc72
DPP4Ta	cc52
DPP4Tb	cc44
DPP2TT2Ta	SD6
DPP2TT2Tb	SD5
DPPTT-T	C1/cc165
SM	Small molecule
ECT	Electron-cascade transfer

PFN	Poly-[(9,9-bis(3'-(N,N-dimethylamino)propyl)-2,7-fluorene)-alt-2,7-(9,9-dioctyl-fluorene)]
DMF	Dimethylformamide
DMSO	Dimethyl sulfoxide
AA	Acetic acid
SCLC	Space-charge-limited-current
OFETs	Organic field effect transistors
TOF	Time-offlight
CELIV	Charge extraction by linearly increasing voltage
AFM	Atomic force microscopy
TEM	Transmission electron microscopy
SPM	Scanning probe microscopy
LPE	Liquid-phase-exfoliation
SBS	Sedimentation-based-separation

Acknowledgements

I would like to express my deepest gratitude to my supervisors, Prof. George Kioseoglou, Prof. Emmanuel Kymakis and Prof. Constantinos Petridis, for giving me the opportunity to carry out this project in their group and for their supervision and guidance along the project. I genuinely thank them for their continuous positive and encouraging attitude and for always being great leaders to look up to. I finally thank them for all the projects, tasks and challenges that have been given to me and that helped me expand significantly my knowledge in the field.

Moreover, I would like to give my thanks to all my colleagues from NANO lab, Minas Stylianakis, Dimitrios Konios, George Kakavelakis, Miron Krassas, Temur Maksudov and Anna Orfanoudaki, for their support.

Finally, I would like to give all my gratitude to a very important person of my life, my girlfriend Irakleia Kouidi, who was always there for me with a smile every time I felt disappointed.

Αφιερωμένο στη μνήμη του πολυαγαπημένου αδελφού μου, Ιωάννη Τζουρμπάκη..

Επίσης, στην οικογένειά μου, Ευάγγελος Τζουρμπάκης, Ζαχαρένια Κελαϊδή και Γεώργιος Τζουρμπάκης..

Dedicated in memory of my beloved brother, Ioannis Tzourmpakis..

As well, to my family, Evaggelos Tzourmpakis, Zaharenia Kelaidi and Georgios Tzourmpakis..

Table of Contents

Contents

Chapter 1: Introduction	10
1.1 Solar Energy	10
1.2 Solar Cell Generations	11
1.2.1 First generation (1G)	11
1.2.2 Second generation (2G)	13
1.2.3 Third generation (3G), Emerging PVs	13
1.2.4 Hybrid (Inorganic – Organic) Solar cells	19
1.3 State of the Art	21
Chapter 2: Materials	23
2.1 Materials used as Electrodes	23
2.1.1 Anode/Positive (Top) electrode material	23
2.1.2 Cathode/Negative (Bottom) Electrode material	24
2.1.2.1 Deposition of Cathode electrode material via Thermal Vacuum Evaporation method	25
2.2 Photo-active layer materials	25
2.2.1 Conjugated Polymers/Electron Donor materials	26
2.2.2 Low Band Gap (LBG) Polymers	30
2.2.3 Small Molecules	35
2.2.4 Fullerenes, Fullerene Derivatives/Electron Acceptor materials	37
2.3 Buffer layers	39
2.3.1 Electron Transport/Hole Blocking material	40
2.3.2 Hole transport/Electron Blocking material	41
Chapter 3: Organic Solar Cells	42
3.1 Structure and general operating principles of OPVs	42
3.1.1 Device structure	42
3.1.2 Device operation	43
3.2 Parameters of Device Characterization	46
3.2.1 Short Circuit Current, I_{sc}/Density of Short Circuit Current, J_{sc}	47
3.2.2 Open circuit voltage, V_{oc}	48
3.2.3 Fill factor, FF	49
3.2.4 Power conversion efficiency, PCE	50
3.2.5 External quantum efficiency, EQE or Incident photon-to-current efficiency, IPCE	50

Chapter 4: Introduction to 2D Materials	52
4.1 Graphite-Graphite Oxide-Graphene Oxide-Reduced Graphene Oxide	52
4.2 Two-Dimensional (2D) Transition Metal Dichalcogenides (TMDs)	56
4.2.1 Tungsten Diselenide, WSe₂	59
Chapter 5: Ternary Organic Solar Cells	61
Chapter 6: Experimental Procedure	64
6.1 Basics	64
6.2 Substrate Cleaning Process	65
6.3 Deposition of Electron transport layer (ETL), PFN	66
6.3.1 Solutions of HTL, PEDOT:PSS, and HTL, PFN	66
6.3.2 Spin-coating technique	67
6.4 Blends and deposition of the Active layer (A.L)	68
6.4.1 Solutions' Preparation	68
6.4.2 Deposition of the Active layer (A.L)	70
6.5 Deposition of Ca, MoO₃ Interface layers and Al negative electrode using Vacuum Thermal Evaporation (VTE) method	71
6.6 Device Characterization	71
6.6.1 Optical absorption spectroscopy (OAS)	73
6.6.2 (I-V) measurement	73
6.6.3 External Quantum Efficiency measurement	74
6.6.4 Calculation of Hole/Electron mobilities via SCLC method	74
6.6.5 Conductivity measurement	75
6.6.6 Atomic Force Microscopy	75
Chapter 7: Results and Discussion	78
7.1 PROJECT 1: PTB₇:WSe₂:PC₇₁BM	78
7.2 PROJECT 2: PTB₇:Compound_T:PC₇₁BM	85
7.3 PROJECT 3: Integrated Hybrid Solar cells (IHSCs)	89
7.3.1 A] cc44/cc52/cc72/SD5/SD6:PC₇₁BM	90
7.3.2 B] cc165:PC₇₁BM, cc165:RGO:PC₇₁BM	95
Chapter 8: Conclusions	102
Chapter 9	103
9.1 Present research	103
9.2 Recommendations for future work	103
Chapter 10	104
10.1 List of Publications	104
10.2 Presentations in Conferences	104

Chapter 1: Introduction

1.1 Solar Energy

When global warming and depletion of common energy sources, such as fossil fuels started threatening the balance of human life, great attention was given to the renewable energy sources. In those alternative energy sources where wind energy, hydroelectric energy, biomass, geothermal energy and solar energy are included, solar energy has the highest amount potentially available. It should be noted, that a very small amount of sun power is capable to cover the whole energy demand worldwide. Considering that there are countries, like Greece, where almost the 8 of the 12 months per year are full of sunny days, research community should focus on the investigation of solar energy production in order to sufficiently cover their needs for energy consumption.

Solar power is a clean, green, endless and therefore promising energy source, which is under really big investigation worldwide. As well, it can be produced by different kind of solar devices which are grouped in three different categories accordingly to the materials used inorganic, organic and hybrid (combination of organic and inorganic, e.g. perovskites). Each category has special characteristics and for historical reasons, inorganic solar cells are the most famous as they were first used for solar energy production. Technically, the efficiency of solar power can be attributed to the Photovoltaic (PV) Effect, a physical process where the semiconductor material converts electromagnetic radiation (sunlight) into Electrical Power. PV effect was first discovered by French physicist A. E. Becquerel¹ in 1839.

The still unreachable goal of all research groups worldwide is to construct a solar cell which would be power efficient and stable, low cost manufactured and long living (lifetime). Those three parameters (efficiency, cost, lifetime) characterize and classify every solar device and are equally important for an efficient solar device.



Figure 1.1 The critical triangle for photovoltaics with the three key factors².

¹ A. E. Becquerel, *Comptes Rendus De L'Académie Des Sciences*, 1839, 9, 145.

² <http://www.dyesol.com/posts/what-is-levelised-cost-of-energy-february-2012-enewsletter/>

1.2 Solar Cell Generations

So far photovoltaic devices (solar cells) have been categorized in three generations according to the time sequence they started playing big role in the solar cell field. In particular:

1.2.1 First generation (1G)

First category includes silicon (Si)-based PV cells that about 86 % of the current photovoltaic production is based on. Si wafers are used for those solar cells and they are dominant because of their high efficiency. The efficiency of the single junction cells has a theoretical limit of about 34% (the *Shockley–Queisser* limit)³. Till now, the biggest disadvantage of 1G solar cells is the cost of production. In particular, the cost per produced Watt of power is nearly 4 times higher than conventional energy prices due to the high cost of the material⁴ (half of the cost of 1G devices is the Si wafer) and cost of production technologies (transformation of amorphous Si to semicrystalline/crystalline). Although, the price continuously goes down along with the progress of the technology, the 1G products will probably reach their price limit before achieving the competitive level in the market^{5,6}. Generally Si based solar cells are more efficient and longer lasting than non-Si based cells. However, they are more at risk to lose some of their efficiency at higher temperatures, than thin-film solar cells (2G).

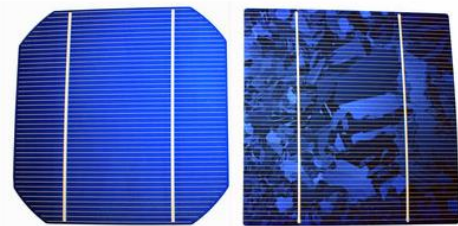


Figure 1.2 From left to right, images of a Monocrystalline and a Polycrystalline Si-based solar cell⁷.

There are currently four types of silicon based cells used in the production of solar panels for residential use. The types are based on the type of silicon used, specifically:

- ***Monocrystalline Silicon Cells***⁸: The first solar cell technology and still the most popular and efficient are solar cells made from thin wafers of silicon. These are called monocrystalline solar cells because the cells are sliced from large single crystals that have been painstakingly grown under carefully controlled conditions. Typically, the cells are a few inches across, and a number of cells are laid out in a grid to create a panel. Relative to the other types of cells, they have a higher efficiency up to 25% with the highest reported efficiencies from *Amonix* reaching 27.6% (single crystal concentrator) and from NREL reaching

³ W. Shockley and H. J. Queisser, Detailed Balance Limit of Efficiency of P-N Junction Solar Cells, *J.Appl.Phys.*, 1961, 32, 510.

⁴ <http://www.solarpanelscostguide.com/>

⁵ <http://solar.calfinder.com/blog/solar-information/solar-genealogy-on-three-generations-of-solar-cells/>

⁶ S. A. Gevorgyan, Production, Characterization and Stability of Organic Solar Cell Devices, PhD Thesis, January 2010.

⁷ <http://www.tindosolar.com.au/poly-vs-mono-crystalline/>

⁸ <http://exploringgreentechnology.com/solar-energy/technology/monocrystalline-solar-cells/>

25% (single crystal non-concentrator) (Fig. 1.12) , meaning you will obtain more electricity from a given area of panel. However, growing large crystals of pure silicon is a difficult and very energy-intensive process, so the production costs are the highest of all the solar panel types. Another issue to keep in mind about panels made from monocrystalline silicon cells is that they lose their efficiency as the temperature increases about 25°C, so they need to be installed in such a way as to permit the air to circulate over and under the panels to improve their efficiency.

- **Polycrystalline Silicon Cells**⁹: It is cheaper to produce silicon wafers in molds from multiple silicon crystals rather than from a single crystal as the conditions for growth do not need to be as tightly controlled. In this form, a number of interlocking silicon crystals grow together. Panels based on these cells are cheaper per unit area than monocrystalline panels - but they are slightly less efficient with values up to 20%. Trina Solar has the highest one with 21.2% (Fig. 1.12).

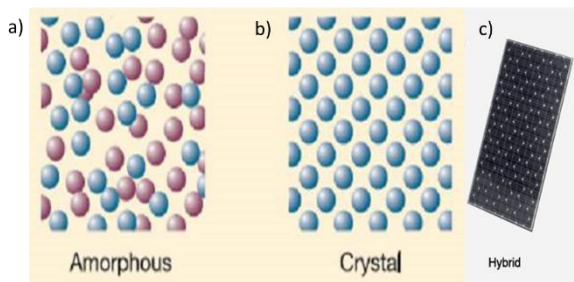


Figure 1.3: A closer look at energy harvesting of a) an amorphous solar cell whose irregular shape of the amorphous silicon cell allows higher light absorption, letting these cells get very thin and even flexible, b) a crystal solar cell and c) a hybrid solar cell (latest category of Si-based solar cells)^{10,11}.

- **Amorphous Silicon Cells**¹²: Instead of growing silicon crystals as is done in making the two previous types of solar cells, silicon is deposited in a very thin layer on to a backing substrate – such as metal, glass or even plastic, with many applications in everyday devices (e.g. calculators, small electronic devices etc.) Sometimes several layers of Si, doped in slightly different ways to respond to different wavelengths of light, are laid on top of one another to improve the efficiency. The production methods are complex, but less energy intensive than crystalline panels and prices have been coming down as panels are mass-produced using this process. One advantage of using very thin layers of silicon is that the panels can be made flexible. The disadvantage of amorphous panels is that they are much less efficient per unit area (up to 10%, AIST 13.6%, Fig. 1.12) and are generally not suitable for roof installations you would typically need nearly double the panel area for the same power output. However, their flexibility makes them an excellent choice for use in making building integrated PV (e.g., roofing shingles), for use on curved surfaces, or even attached to a flexible backing sheet so that they can

⁹ http://pv.energytrend.com/research/Polysilicon_Manufacturing_20111117.html

¹⁰ <http://www.c-changes.com/types-of-solar-panel>

¹¹ <http://www.digikey.com/en/articles/techzone/2012/sep/a-closer-look-at-energy-harvesting-the-cymbet-energy-harvesting-development-kit>

¹² <http://energyinformative.org/amorphous-silicon-solar-panels/>

even be rolled up and used when going camping/ backpacking, or put away when they are not needed!

- **Hybrid Silicon cells^{13,14}**: One recent trend in the industry is the emergence of hybrid silicon cells and several companies are now exploring ways of combining different materials to make solar cells with better efficiency, longer life, and at reduced costs. Recently, Sanyo introduced a hybrid cell whereby a layer of amorphous silicon is deposited on top of single crystal wafers¹⁵. The result is an efficient solar cell that performs well in terms of indirect light and is much less likely to lose efficiency as the temperature climbs.

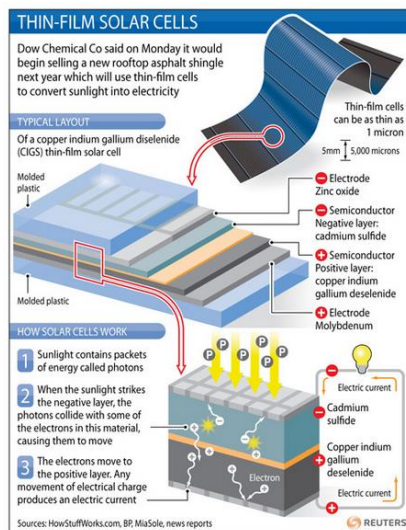


Figure 1.4 Structure of a thin-film solar cell¹⁶.

1.2.2 Second generation (2G)

Second generation or *thin-film* solar cells have lower production cost than 1G but, they have lower efficiencies. The superior characteristic of thin-films offers the great property of *flexibility* which dictates the availability of almost any shape surface application. Thin-film technology has spurred lightweight, aesthetically pleasing solar innovations such as solar shingles and solar panels. The 2G is predicted to be the new dominant of solar market with higher efficiencies and that's because of the

worldwide interest in our days. Different techniques are utilized for production process such as solution deposition, vapor deposition, electroplating and etc. Most successful materials for 2G are amorphous silicon, CuIn(Ga)Se_2 (CIGS), CdTe/CdS , which are being deposited on thin substrates. Devices based on these materials can deliver lab efficiencies up to 20% (ZSW 21.7%, First Solar 21.5%, Fig. 1.12), but the module efficiencies are reaching only 14 % due to difficulties in producing large scale uniform films¹⁷. Although thin film technology can significantly decrease the prices for PVs, 2G solar cells will also hit certain price limits per watt due to efficiency limits and the material costs.

1.2.3 Third generation (3G), Emerging PVs

A generation beyond silicon-based solar cells. Specifically, 3G includes solar cells which do not use the p-n junction structure that is used in traditional semiconductor, Si-based solar cells.

¹³ <http://web.stanford.edu/group/mcgehee/publications/NL2012b.pdf>

¹⁴ <http://cleantechnica.com/2011/06/27/hybrid-monocrystalline-and-multicrystalline-solar-cells/>

¹⁵ http://www.jointsolarpanel.nl/fileadmin/jointsolarpanel/user/documents/seminar2009/4_Miro_Zeman_Delft_University_of_Technology.pdf

¹⁶ <http://blogs.reuters.com/from-reuterscom/2009/10/06/graphic-thin-film-solar-cells/>

¹⁷ M. A. Green, K. Emery, Y. Hishikawa, and W. Warta, Solar Cell Efficiency Tables (Version 34), Prog. Photovolt: Res. Appl. , 2009, 17, 320.

Third generation contains a wide range of potential and efficient solar innovations including: Dye-sensitized nanocrystalline TiO₂ solar cells (DSSCs)^{18,19}, molecular organic solar cells (MOSCs) and polymer organic solar cells (PSCs)²⁰.

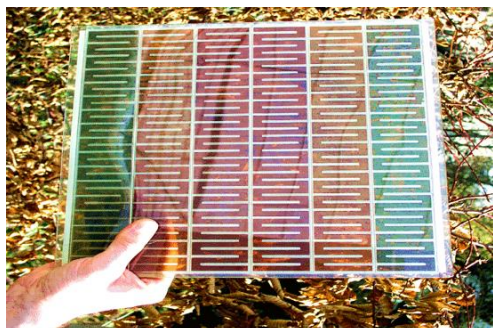


Figure 1.5 A Dye-sensitized solar cell using Algae Technology²¹.

- **Dye-sensitized solar cells (DSSCs):** are based on combination of dyes with metal oxides and electrolyte. Dye-sensitized solar cells (DSSCs) have many advantages over their silicon-based counterparts. They offer transparency, low cost, and high power conversion efficiencies under cloudy and artificial light conditions. However, until now their overall efficiency has been lower than silicon-based solar cells, mostly because of the inherent voltage loss during the regeneration of the sensitizing dye. The efficiencies of DSSC are in the range of 12% (Fig.1.12) for small lab scale devices, while the lifetime of the devices is rather low compared to inorganic solar cells. In a DSSC, an organic dye adsorbed at the surface of an inorganic wide band gap semiconductor is used for absorption of light and injection of the photoexcited electron into the conduction band of the semiconductor. The research on DSSCs gained considerable impulse, when Grätzel and co-workers greatly improved the interfacial area between the organic donor and inorganic acceptor by using nanoporous titanium dioxide (TiO₂)²².
- **Perovskite-Sensitized Solar cells (PSSCs):** In a Nature publication²³ Professor Michael Graetzel (G24 Power advisory board member) and his team at École Polytechnique Fédérale de Lausanne (EPFL), have developed a state solid version of the DSSC that is fabricated by a new two-step process raising their efficiency up to 15%, with a confirmed record of 14.1% but, without sacrificing stability. The new solid-state embodiment of the DSSC uses a perovskite (CaTiO₃) material as a light harvester and an organic hole transport material to replace the cell's electrolyte. Typical fabrication of this new DSSC involves depositing a perovskite material directly onto a metal-oxide film. The problem is that adding the entire material together often causes wide variation in the morphology and the efficiency of the resulting solar cell, which makes it

¹⁸ M. Grätzel, J. Photochem. Photobiol. C: Photochem. Rev., 2003, 4, 145.

¹⁹ P. Chawla, M. Tripathi, Int. J. Energy Res., 2015.

²⁰ G. Li, R. Zhu, Y. Yang, Nat. Photon., 2013, 6, 153.

²¹ <http://www.celsias.com/article/algae-technology-makes-solar-cells-3x-efficient/>

²² B. O'Regan, M. Grätzel, Nature, 1991, 335, 737.

²³ J. Burschka, N. Pellet, S. J. Moon, R. Humphry-Baker, P. Gao, M. K. Nazeeruddin, M. Grätzel, Nature, 2013, 499, 316.

difficult to use them in everyday applications. Michael Grätzel's team at EPFL has now solved the problem with a two-step approach: First, one part of the perovskite is deposited in to the pores of the metal-oxide scaffold. Second, the deposited part is exposed to a solution that contains the other component of the perovskite. When the two parts come into contact, they react instantaneously and convert into the complete light-sensitive pigment, permitting much better control over the morphology of the solar cell. The new method raises DSSC power-conversion efficiency up to a record 15%, exceeding the power conversion efficiencies of conventional, amorphous silicon-based solar cells. The authors believe that it will open a new era of DSSC development, featuring stability and efficiencies that equal or even surpass today's best thin-film photovoltaic devices.

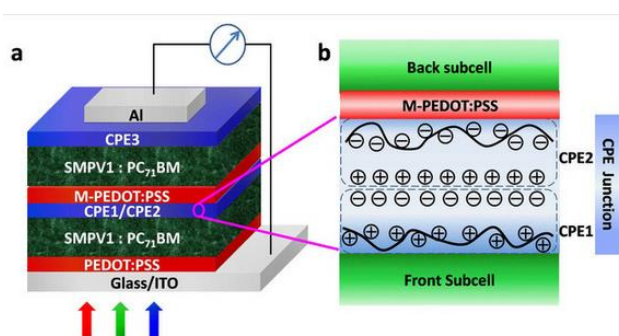


Figure 1.6 a), b) Structure of layers of a small-molecule solar cell²⁴.

- **Molecular organic solar cells**²⁵ These small molecules offer advantages over their polymeric counterparts: (a) their structures are well defined and exhibit no molecular weight dependence, leading to improved purity and limiting batch-to-batch variation and (b) they typically exhibit more organized nanostructures, leading to higher charge carrier mobilities (p-type or n-type). Additionally, small molecule architectures are sensitive to subtle structure changes thus, electronic energy levels, optical absorption, and self-assembly tendencies can be systemically tuned to maximize device performance. Many small molecular p-type semiconductors have been studied for decades. Among these molecules, only a small fraction has been applied successfully as electron donors in OPV devices due to the various optical, electrical, and stability requirements demanded of the chosen materials. Except the aforementioned properties, small molecules offer, exciton diffusion length, thin film morphology, frontier energy level alignment, band gap, and absorption coefficient, all greatly affect the performance of OPV device. When coupled with fullerene electron acceptors such as [6,6]-phenyl- C_{71} -butyric acid methyl ester ($PC_{71}BM$), small molecule-based solar cells have achieved record PCEs over 8%^{26,27}.

²⁴ Y. Liu, C.-C. Chen, Z. Hong, J. Gao, Y. M. Yang, H. Zhou, L. Dou, G. Li and Y. Yang, *Sci. Rep.* 2013, 3, 3356.

²⁵ Y. Lin, Y. Lia and X. Zhan, *Chem. Soc. Rev.*, 2012, 41, 4245-4272.

²⁶ V. Gupta, A. K. K. Kyaw, D. H. Wang, S. Chand, G. C. Bazan, A. J. Heeger, *Sci. Reports*, 2013, 3.

²⁷ J. Zhou, Y. Zuo, X. Wan, G. Long, Q. Zhang, W. Ni, Y. Liu, Z. Li, G. He, C. Li, B. Kan, M. Li, Y. J. Chen, *Am. Chem. Soc.* 2013, 135, 8484.

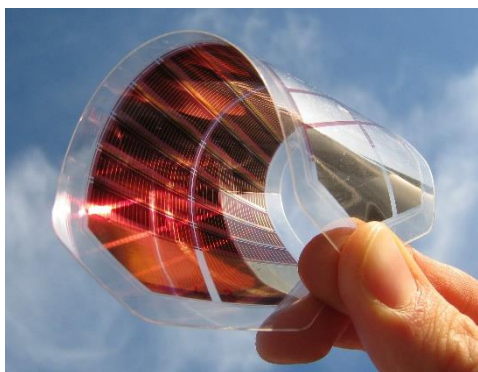


Figure 1.7 A flexible, 3-D printed, organic polymer solar cell²⁸.

- **Polymer Organic Solar Cells:** OSC technologies are under continuous development as that interest stems from their great characteristics including: fabrication with flexible substrates, lightweight, and production by inexpensive, low temperature deposition techniques such as spin-coating and printing, solution processed, transparent and use of cheap raw materials.

Especially in the last decade the field of OPVs has been growing really fast and showing promising potential for rather cheap PV technology. For that reason, in recent years OPVs became one of the most fascinating fields of research. Historically, anthracene was the first organic compound in which photoconductivity have been observed by Pochettino in 1906²⁹ and which started a new era for studying organic compounds for electronic applications. There are three subcategories of polymer organic solar cells:

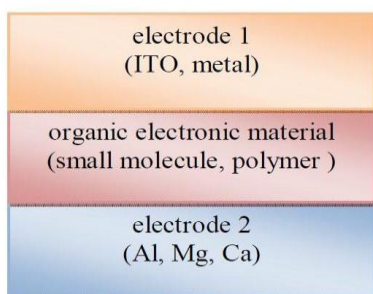


Figure 1.8 A typical single-layer solar cell³⁰.

- **Single-layer OSCs:** Single layer organic photovoltaic cells are the simplest form. The first attempts to create all-organic solar cells were made by sandwiching a layer of organic electronic materials between two metallic conductors (Fig. 1.8), typically a layer of indium tin oxide (ITO) with high band and a layer of low work function metal such as Aluminum (Al), Magnesium (Mg) or Calcium (Ca). In these cells, the photovoltaic properties strongly depend on the nature of the electrodes. Heavily doped conjugated materials resulted in reasonable power conversion efficiencies up to 0.3%.

²⁸ <http://3dprint.com/1666/scientists-3d-print-new-solar-panels-which-work-best-when-cloudy/>

²⁹ A. Pochettino, Acad. Lincei Rend. , 1906, 15, 355.

³⁰ <http://www.brighthub.com/environment/renewable-energy/articles/95572.aspx>

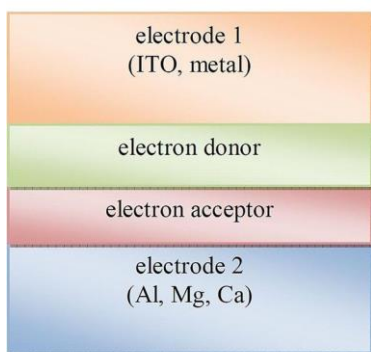


Figure 1.9 A typical bi-layer solar cell³¹.

- ***Bi-layer OSCs***: In the double-layer structure (Fig. 1.9) the photo-excitations in the photoactive material have to reach the p-n interface where charge transfer can occur, before the excitation energy of the molecule is lost via intrinsic radiative and non-radiative decay processes to the ground state. Because the exciton diffusion length of the organic material is in general limited to 5-10nm, only

absorption of light within a very thin layer around the interface contributes to the photovoltaic effect. This limits the performance of double-layer devices, because such thin layer can impossibly absorb all the light. A strategy to improve the efficiency of the double-layer cell is related to structural organization of the organic material to extend the exciton diffusion length and, therefore, create a thicker photoactive interfacial area.

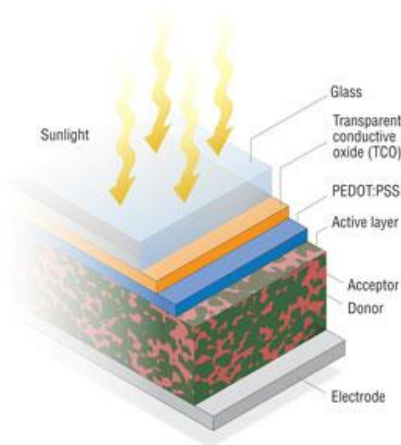


Figure 1.10 A typical Bulk-heterojunction solar cell³².

- ***Bulk Heterojunction or Microphase Separated material OSCs***: The bulk heterojunction is presently the most widely used photoactive layer. The name bulk-heterojunction solar cell has been chosen, because the interface (heterojunction) between both components is all over the bulk (Fig. 9), in contrast to the classical (bilayer) heterojunction. As a result of the intimate mixing, the interface where charge transfer can occur has increased enormously. The

exciton (hole-excited electron pair), created after the absorption of light, has to diffuse towards this charge-transfer interface for charge generation to occur. The diffusion length of the exciton in organic materials, however, is typically 5-10 nm³³. This means that for efficient charge generation after absorption of light, each exciton (hole-electron pair) has to find a Donor:Acceptor (D:A) interface within a few nm to dissociate otherwise, it will be lost (emission/losses) without charge generation. An intimate bi-continuous network of donor and acceptor materials in the nanometer range should suppress exciton loss prior to charge generation. Control of morphology is not only required for a large charge-generating interface and suppression of exciton loss, but also to ensure percolation pathways for both electron and hole transport to the collecting electrodes respectively. In combining electron donating (p-type) and electron

³¹ <http://www.brighthub.com/environment/renewable-energy/articles/95572.aspx>

³² <http://photovoltaicell.com/polymer-based-organic-photovoltaic-opv-cells/>

³³ M. Sim, J. Shin, C. Shim, M. Kim, S. B. Jo, J.-H. Kim and K., Cho J. Phys. Chem. C 2014, 2, 118.

accepting (n-type) materials in the active layer of a solar cell, care must be taken that excitons created in either material can diffuse to the interface, to enable charge separation. Due to their short lifetime and low mobility, the limited diffusion length of excitons in organic semiconductors, imposes an important condition to efficient charge generation. Anywhere in the active layer, the distance to the interface should be on the order of the exciton diffusion length. Despite their high absorption coefficients, exceeding 10^5 cm^{-1} , a 20 nm double layer of donor and acceptor materials (bi-layer) would not be optical dense, allowing most photons to pass freely. The solution to this dilemma is elegantly simple. By simple mixing the p and n-type materials and relying on the intrinsic tendency of polymer materials to phase separate on a nanometer dimension, junctions throughout the bulk of the material are created that ensure quantitative dissociation of photo-generated excitons, irrespective of the thickness. Polymer-fullerene solar cells were among the first to utilize this bulk-heterojunction principle. Nevertheless, this attractive solution poses a new challenge. Photo-generated charges must be able to migrate to the collecting electrodes through this intimately mixed blend. Because holes are transported by the p-type semiconductor and electrons by the n-type material, these materials should be preferably mixed into a bi-continuous, interpenetrating network in which inclusions, barrier layers are avoided. When such a bulk-heterojunction is deposited on an ITO substrate and capped with a metal back electrode, working photovoltaic cells can be obtained.

- **Tandem solar cells**: Typically, for a double-junction cell, such a tandem structure consists of a front cell with a high-bandgap material, an interconnecting layer, and a rear cell with a low-bandgap (LBG) material.^{34,35,36,37} Compared with a single-junction device using low-bandgap materials, the multi-junction/tandem structure can reduce thermalization loss of photonic energy during the photon to electron conversion process, and maximize the open circuit voltage (V_{oc}). The high bandgap material in the front cell, which is responsible for the absorption of high-energy photons provide higher V_{oc} than the low bandgap material. Therefore, by adopting polymers with matched absorption spectra, a tandem solar cell can effectively utilize the photonic energy and optimize open-circuit voltage, which leads to high PCE. In serial connected tandem solar cell, it is very obvious that subcell current balancing is critical for achieving high efficiency.³⁸

³⁴ J. Yuan, J. Gu, G. Shi, J. Sun, H.-Q. Wang, W. Ma, *Sci. Rep.*, 2016, 6, 26459.

³⁵ T. Ameri et al., *Energy Environ. Sci.*, 2009, 2, 347.

³⁶ S. Sista et al., *Adv. Mater.*, 2010, 22, 380.

³⁷ J. Yang, et al., *Adv. Mater.*, 2011, 23, 3465.

³⁸ J. Gilot, M. M. Wienk, R. A. J. Janssen, *Adv. Mater.*, 2010, 22, E67.

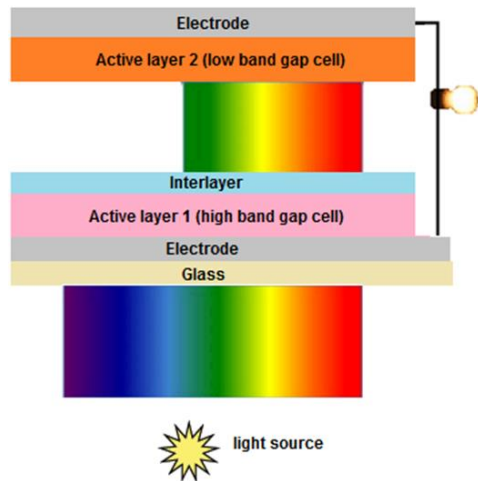


Figure 1.11 Tandem solar cell structure consisting of two photovoltaic cells having different band gaps³⁹.

Inorganic multijunction/tandem solar cells have gone a long way and the latest cell efficiency of 46% have been certified⁴⁰, which shows the great potential of tandem solar cell. For polymer tandem solar cells, Hadipour et al.⁴¹ demonstrated a polymer tandem solar cell consisting of two subcells with two different materials with about 0.57% efficiency in 2006, which is higher than each of the subcell's efficiencies. In 2007, Kim et al. used a new interconnecting layer structure to bridge two higher

performance single junction polymer PV cells to realize a tandem structure with 6.5% PCE⁴². More recently, Janssen et al.⁴³ has studied the effect of current matching on the tandem device performance, which provides more insight to achieve high-performance tandem PSC. However, the polymer tandem solar cells' performance has been limited to around 7% efficiency in the last 4 years mainly due to the lack of high performance low bandgap polymers⁴³ with high V_{oc} and high external quantum efficiency (EQE) at long wavelengths. Recently, Chen and coworkers demonstrated a solution-processed tandem OSC with a PCE with power conversion efficiencies >12% (verified 12.70%), which represents a new level of capability for solution-processed, OSCs.⁴⁴

1.2.4 Hybrid (Inorganic – Organic) Solar cells

Decrypting the title of this part, it is understood that this is not a separate category but, a combination of the previous ones. Specifically, a hybrid solar cell consists of both an organic and an inorganic material therefore, combines the unique properties of inorganic semiconductors with the film forming properties of the conjugated polymers. A special subcategory of this technology is:

- **Perovskite Solar cells (PSCs)**: PSCs have been characterized as the most potentially promising solar cell technology from the solar cell research community that has exhibited a meteoric rise in their efficiency through the last 5 years, resulting in performances comparable with current state of the art polycrystalline silicon (Fig. 1.12). Hybrid metal halide perovskites have

³⁹ <http://www.intechopen.com/books/global-warming-impacts-and-future-perspective/alternative-resources-for-renewable-energy-piezoelectric-and-photovoltaic-smart-structures>

⁴⁰ <https://www.ise.fraunhofer.de/en/press-media/press-releases/2014/new-world-record-for-solar-cell-efficiency-at-46-percent.html>

⁴¹ Hadipour, A. et al., *Adv. Funct. Mater.*, 2006, 16, 1897.

⁴² J. Y. Kim et al., *Science*, 2007, 317, 222.

⁴³ J. Gilot, M. M. Wienk, R. A. J. Janssen, *Adv. Mater.*, 2010, 22, E67.

⁴⁴ Y. Chen et al., *Nat. Photonics*, 2017, 11, 85.

some remarkable properties, such as the medium optical bandgap and strong absorption coefficients⁴⁵, the long carrier diffusion lengths⁴⁶, the low recombination losses^{47,48} and bandgap tunability⁴⁹, therefore they have attracted great interest presenting the potential to be established as an efficient, low cost and flexible, large-scale PV technology.

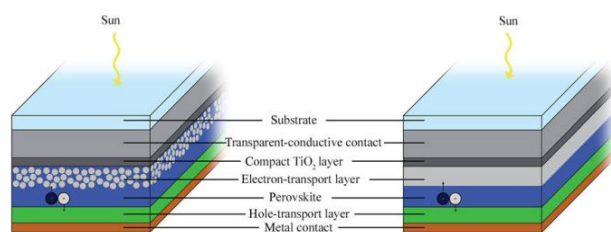


Figure 1.12 Two perovskites solar cell structures. Comparison of the mesoporous (left) and planar (right) architectures used in perovskite solar cells. Most devices with high efficiency use glass /FTO /TiO₂ /CH₃NH₃PbI₃ /Spiro-OMeTAD/Au

defined.

In 2009, Miyasaka and co-workers pioneered the first photovoltaic results for CH₃NH₃PbI₃ based perovskite with power conversion efficiency (PCE) of 3.8%.⁵⁰ In late 2012, Gratzel and Park et al. used CH₃NH₃PbI₃ as a light harvester in combination with the 2,2',7,7'-tetrakis[N,N-di(4-methoxyphenyl)amino]-9,9'-spirobifluorene (spiro OMeTAD) hole transport materials on mesoporous TiO₂, which led to a PCE of up to 9.7%.⁵¹ In the past three years, the PCE of larger than 15%^{52,53} has been reported by different groups as new materials and engineering process improved and led to efficiencies up to 22% nowadays⁵⁴.

However, most state-of-the-art efficient PSCs based on methylammonium lead iodide (MAPbI₃) or formamidinium lead iodide (FAPbI₃) only utilize solar radiation below a wavelength of ≈ 800 nm, leaving the majority of the near-infrared (NIR) range unused.^{55,56} Therefore, if PSC researchers are able to find a way to utilize NIR solar radiation efficiently, it is possible to further improve the PCE to values approaching the Shockley–Queisser limit.⁵⁷

⁴⁵ N. K. Kumawat, M. N. Tripathi, U. Waghmare, D. Kabra, *J. Phys. Chem. A*, 2016, 120, 3917.

⁴⁶ S. D. Stranks, G. E. Eperon, G. Grancini, C. Menelaou, M. J. P. Alcocer, T. Leijtens, L. M. Herz, A. Petrozza, H. J. Snaith, *Science*, 2013, 342, 341.

⁴⁷ Y. H. Lee, J. Luo, R. Humphry-Baker, P. Gao, M. Grätzel, M. K. Nazeeruddin, *Adv. Funct. Mater.*, 2015, 25, 3925.

⁴⁸ G. Kakavelakis, T. Maksudov, D. Konios, I. Paradisanos, G. Kioseoglou, E. Stratakis, E. Kymakis, *Adv. Energy Mater.*, 2017, 7, 1602120.

⁴⁹ T.-B. Song, Q. Chen, H. Zhou, C. Jiang, H.-H. Wang, Y. Yang, Y. Liu, J. You, Y. Yang, *J. Mater. Chem. A*, 2015, 3, 9032.

⁵⁰ A. Kojima, K. Teshima, Y. Shirai, T. J. Miyasaka, *J. Am. Chem. Soc.*, 2009, 131, 6050.

⁵¹ Kim et al., *Sci. Rep.*, 2012, 2, 591.

⁵² Xiao et al., *Energy Environ. Sci.*, 2014, 7, 2619.

⁵³ N. J. Jeon, J. H. Noh, Y. C. Kim, W. S. Yang, S. Ryu, S. I. Seok, *Nat. Mater.*, 2014, 13, 897.

⁵⁴ A. Kojima, K. Teshima, Y. Shirai, T. Miyasaka, *J. Am. Chem. Soc.*, 2009, 131, 6050.

⁵⁵ N. J. Jeon, J. H. Noh, W. S. Yang, Y. C. Kim, S. Ryu, J. Seo, S. I. Seok, *Nature*, 2015, 517, 476.

⁵⁶ J.-W. Lee, D.-J. Seol, A.-N. Cho, N.-G. Park, *Adv. Mater.*, 2014, 26, 4991.

⁵⁷ P. K. Nayak, D. Cahen, *Adv. Mater.*, 2014, 26, 1622.

- **Parallel-like tandem or Integrated Solar cells:** One promising approach to broadening the absorption range of PSCs above 800 nm is to integrate perovskite and a bulk-heterojunction (BHJ) as an interlayer-free, parallel-like tandem cell, a so-called perovskite/organic “integrated” hybrid solar cell (IHSC).⁵⁸ In general, the BHJ in ISC is a photoactive layer composed of an NIR absorbing conjugated polymer (low band gap or small molecule) and a fullerene derivative typically used in organic solar cells (mostly PC₇₁BM). Because both films (perovskite and BHJ) have ambipolar charge transporting properties, the electrons and holes generated in both films can be collected at each electrode, as in two-terminal parallel tandem devices. Therefore, by combining a perovskite as a UV–vis absorber (higher band gap material) and a BHJ layer as an NIR absorber in IHSCs, it could be possible to harvest full-range light, covering the UV to NIR solar spectrum (Fig. 1.12).

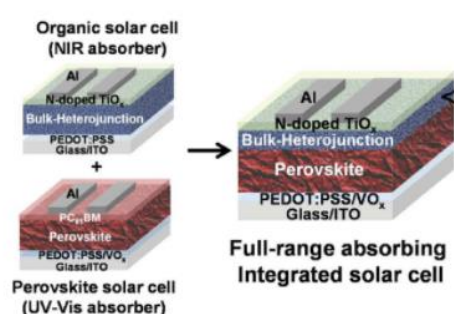


Figure 1.13 Device architecture of the P-I-N type integrated solar cell obtained from organic and perovskite solar cells.

Moreover, in contrast to conventional series/parallel tandem devices, ISCs can be easily fabricated by monolithically stacking perovskite and BHJ without interlayers because of their mutual solvent orthogonality. Furthermore, IHSCs do not suffer from

thermalization losses originating from the current and/or voltage mismatch among sub cells, as encountered in conventional series and parallel tandem cells.⁵⁹ Unfortunately, there have been only two reports which studied on the IHSC devices until now, and the device performances of the ISCs are relatively lower than those of typical PSCs.^{43,59} Especially, their low fill factors (FFs), which are far below the typical values ($\approx 80\%$) of conventional PSCs, and inefficient NIR harvesting hinder further enhancement of the ISC performance. Considering the excellent charge transport property and long exciton diffusion length (L_D) of the perovskites, the low performance of the IHSCs seems to originate from the poor charge transport and short L_D of the organic components in the non-optimized BHJ films.^{60,61}

1.3 State of the Art

⁵⁸ C. Zuo, L. Ding, J. Mater. Chem. A, 2015, 3, 9063.

⁵⁹ L. T. Dou et al., J. Am. Chem. Soc., 2012, 134, 10071.

⁶⁰ S. H. Park et al., Nat. Photon., 2009, 3, 297.

⁶¹ J. Kim et. al., Adv. Mater., 2016, 28, 3159.

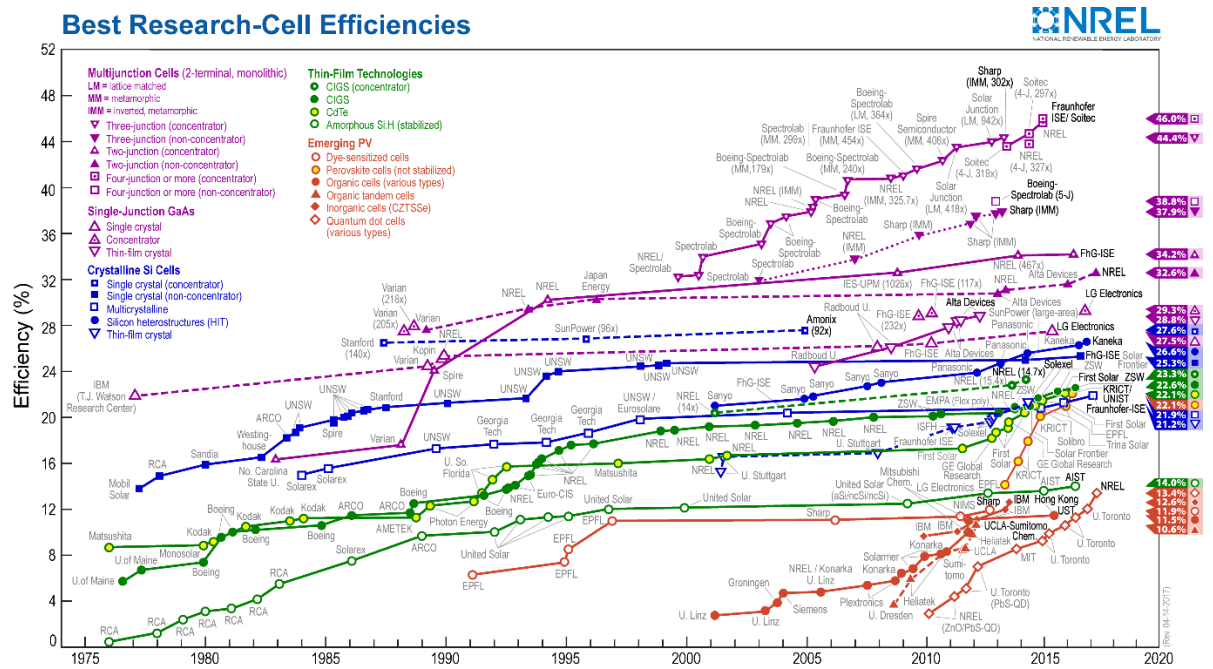


Figure 1.14 Best research solar cell efficiencies⁶².

⁶² <https://www.nrel.gov/pv/assets/images/efficiency-chart.png>

Chapter 2: Materials

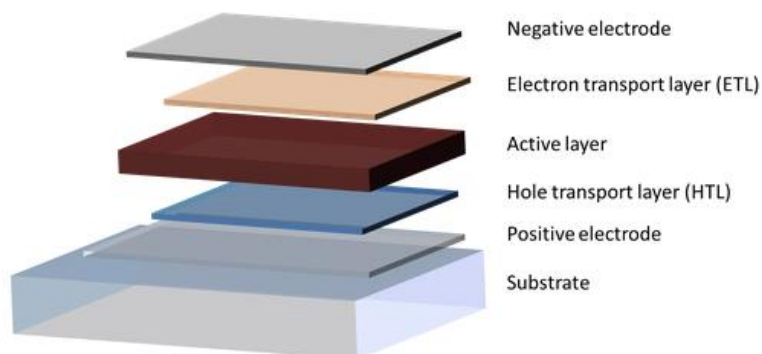


Figure 2.1 The different layers of an OSC⁶³.

As initially referred, in this thesis the **Ternary** BHJ SC project will be presented. A Ternary structure, which is in

detail described in Ch. 6, is a typical structure but with an extra third component added inside the active layer.

2.1 Materials used as Electrodes

The role of the electrodes in a solar cell device is the efficient collection and extraction of charges.

2.1.1 Anode/Positive (Top) electrode material

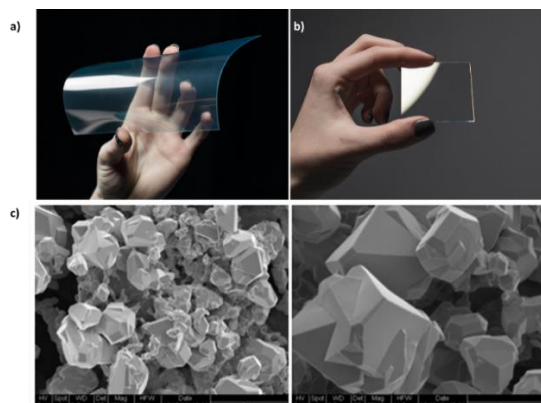


Fig. 2.2 a) ITO Coated PET Plastic⁶⁴, b) ITO Coated Glass⁶⁵c) Crystals of ITO. Image courtesy of Arnold Forman (Jaramillo Group, Stanford)⁶⁶.

Transparent conducting oxides (TCOs) are widely used as electrodes in a large variety of optoelectronic devices due to their unique combination of optical and electrical properties (superior stability, high transparency in the visible range and high electrical conductivity).⁶⁷ Superior stability, transparency and conductivity are the main characteristics a TCO must have and nowadays, indium tin oxide (ITO) is the most popular commercial TCO.

⁶³ <http://plasticphotovoltaics.org/lc/lc-polymersolarcells/lc-layer.html>

⁶⁴ <http://www.adafruit.com/products/1309>

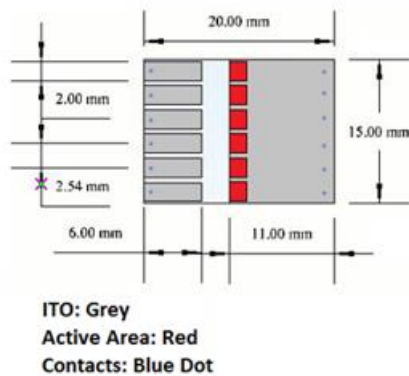
⁶⁵ <https://www.adafruit.com/products/1310>

⁶⁶ <https://snsf.stanford.edu/equipment/eim/magellan.html>

⁶⁷ X. Yu, T. J. Marks, A. Facchetti, 2016, Nat. Mater., 15, 383.

In this project, glass substrates coated with ITO have dimensions of 20x15x1.1 mm size (Fig. 2.3) were purchased by Luminescence Technology Corp. The ITO layer has about 100nm thickness and a surface resistance of $\sim 20 \Omega/\text{sq}$.

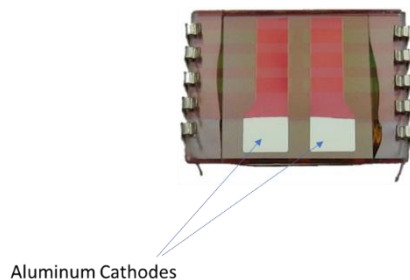
Figure 2.3 Schematic drawing shows physical dimensions of patterned ITO glass.



2.1.2 Cathode/Negative (Bottom) Electrode material

Usually, in both Conventional and Inverted devices, Aluminum (Al) is used as the metallic Cathode material because it matches with ITO Anode as it has a lower (absolute value) Work Function (4.3, ITO has 5.1). Some advantages of Al cathodes⁶⁸:

1. Lower voltage required to do the same work compared to the other materials (Au or Ag).
2. Long life (some cathodes in service over 3 years for encapsulated devices).
3. No undesirable metals to contaminate the anodizing bath.
4. High surface area per cathode.
5. Easily replaced.
6. Uses less tank space.
7. Less heat build up.
8. Overall lower operating cost.
9. Simpler to change the cathode area.



⁶⁸ A. K. Pandey, P. E. Shaw, D. W. Samuel, J.-M. Nunzi, Appl. Phys. Lett., 2009, 94, 103303.

Figure 2.4 Al cathodes of an OSC⁶⁹.

2.1.2.1 Deposition of Cathode electrode material via Thermal Vacuum Evaporation method

One of the common methods of Physical Vapor Deposition (PVD) is Vacuum Thermal Evaporation (VTE). This is a form of Thin Film Deposition (TFD), which is a vacuum technology for applying coatings of pure materials to the surface of various objects. The coatings, also called films, are usually in the thickness range of angstroms (Å) to microns (µm) and can be a single material, or can be multiple materials in a layered structure. The materials to be applied can be pure atomic elements including both metals and non-metals, or can be molecules such as oxides and nitrides. The object to be coated is referred to as the substrate, and can be any of a wide variety of things such as: semiconductor wafers, solar cells, optical components, or many other possibilities. VTE involves heating a solid material inside a high vacuum chamber, taking it to a temperature which produces some vapor pressure. Inside the vacuum, even a relatively low vapor pressure is sufficient to raise a vapor cloud inside the chamber. This evaporated material now constitutes a vapor stream, which traverses the chamber and hits the substrate, sticking to it as a coating or film. Since, in most cases, the material is heated to its melting point and is liquid, it is usually located in the bottom of the chamber, often in some sort of upright crucible. The vapor then rises above this bottom source, and the substrates are held inverted in appropriate fixtures at the top of the chamber. The surfaces intended to be coated are thus facing down toward the heated source material to receive their coating (Fig. 2.5). Steps may have to be taken to assure film adhesion, as well as control various film properties as desired. Fortunately, evaporation system design can allow adjustability of a number of parameters (evaporation rate, sensors for film thickness accuracy) in order to give process engineers the ability to achieve desired results for such variables as thickness, uniformity, adhesion strength, stress, grain structure, optical or electrical properties, etc.

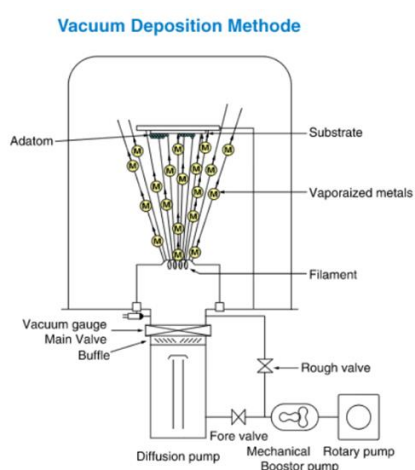


Figure 2.5 A schematic of thermal evaporation equipment. Under the high vacuum atmosphere, heated materials will evaporate and deposit onto our substrate⁷⁰.

2.2 Photo-active layer materials

Organic semiconductors can be categorized into two major classes, namely small molecules and macromolecules (or polymers).⁷¹ Both are conjugated systems consisting of a delocalized p-

⁶⁹ <http://spie.org/x37692.xml>

⁷⁰ http://www.osaka-vacuum.com/0101vacuum_d.html

⁷¹ M. Schwoerer, H.C. Wolf, *Organic Molecular Solids*, Weinheim, 2007.

electron system along their backbones, but different in the overall size. Polymers are molecules made up of repeating structural units, or monomers and are referred to macromolecules because of their large in size.⁷² When all the repeating units along a chain are of the same chemical type, the resulting polymer is called a homo-polymer while polymerization of more than one type of monomers results into a copolymer (i.e. when chains contain two or more different repeating units). In each of the polymer molecules, the atoms are bound together by covalent inter-atomic bonds and can form chemical structures that are linear, cyclic or branched. Some polymers have semiconducting properties due to their unique macromolecular structure characterized by the formation of alternating single and double bonds between the adjacent carbon atoms. These polymers are known as π -conjugated polymers.

In OSCs the main difference between the three different structures (Single layer, Binary, Bulk-heterojunction) is the “design” of the photo-active layer. All devices that fabricated during the experiments were in the category of bulk-heterojunction OSCs, where in that case the polymer and fullerene are mixed (blend). The photo-active material is consisted of an electron donor (conjugated polymers, small molecules) and an electron acceptor, the fullerene derivative (mostly PC₇₁BM). Fullerene derivatives have been the electron-acceptor components in state-of-the-art performing polymer solar cells since 1995,⁷³ while π -conjugated polymers act as electron-donors and the main absorbers, given the poor optical absorption of fullerene in the visible range of the spectrum. Indeed, ultrafast photo-induced electron transfer occurs in a number of conjugated polymer/fullerene pairs, with a quantum efficiency for charge separation close to 100%.⁷⁴

2.2.1 Conjugated Polymers/Electron Donor materials

In semiconductor physics, a donor is a dopant atom that when added to a semiconductor (e.g. Si lattice) can form an n-type region as the number of electrons in the conduction band increase. An impurity atom in a semiconductor which can contribute or donate one or more conduction electrons to the crystal by becoming ionized and positively charged. For example, an atom of column 5 of the periodic table substituting for a regular atom of a germanium (Ge) or silicon (Si) crystal is a donor because it has one or more valence electrons which can be detached and added to the conduction band of the crystal. In organic chemistry and in OSC technology, the donor is the light absorbing material, a polymer or small molecule, in which an electron is excited and transferred to the acceptor.

Historically, in 2000, *A.J. Heeger*, *A. G. MacDiarmid* and *H. Shirakawa* were awarded with the Nobel Prize in chemistry as they first discovered in 1977^{75,76} that chemical doping of conjugated polymers results in an increase of the latter’s electronic conductivity by several orders of magnitude. Conjugated polymers are a new class of organic materials with promising

⁷² W.D. Callister, D.G. Rethwisch, *Materials Science and Engineering: An Introduction*, 2006.

⁷³ G. Yu, J. Gao, J. C. Hummelen, F. Wudl and A. J. Heeger, *Science*, 1995, 270, 1789.

⁷⁴ C. J. Brabec, G. Zerza, G. Cerullo, S. De Silvestri, S. Luzzati, J. C. Hummelen and N. S. Sariciftci, *Chem. Phys. Lett.*, 2001, 340, 232.

⁷⁵ Shirakawa H., Louis E.J., Macdiarmid A.G., et al. *J.C.S. Chem. Comm.*, 1977, 16, 578.

⁷⁶ C. K. Chiang, C. R. Fincher, Y. W. Park, A. J. Heeger, H. Shirakawa, E. J. Louis, S. C. Gau, A. G. MacDiarmid, *Phys. Rev. Lett.*, 1977, 39, 1098.

electronic properties. In their pristine form they behave as an insulator or a semiconductor, while in their doped form they become semi-conducting. Together with these electrical properties come the intrinsic advantages of polymers, such as low cost, low toxicity and ease of manufacture over large area on low weight and flexible substrates. Most organic semiconductor materials are conjugated polymers that essentially consist of a linear framework of alternating single and double bonds between the carbon atoms along the polymer backbone. Conjugated polymers are nowadays used in various electronic applications, like transistors, photodiodes, light emitting diodes, solar cells, etc.

Semiconducting behavior in Organic Semiconductors

Originally, it is demonstrated that Carbon atom (C-atom) is the main element constituting polymer materials. The type of bonds between two adjacent C-atom formed by their valence electrons determines the overall electronic properties of a given polymer. Those chemical bonds could be either saturated or unsaturated bonds. Saturated polymers are insulators since all the four valence electrons of C-atom are used for the formation of covalent bonds (i.e. sp^3 hybridization orbitals), while most conductive polymers have unsaturated conjugated structure. The electronic configuration of π -conjugated polymers stems from their alternated single and double carbon-carbon bonds. Therefore, the fundamental source of the semiconducting property of conjugated polymers originates from the overlapping between the molecular orbitals formed by the valence electrons of chemically bonded C-atoms. It is arisen from the π -delocalization of single $2p_z$ valence electrons along the polymer backbone. This phenomenon is occurring when one $2s$ orbital in C-atom is mixed with two of the $2p$ orbitals of C-atom to forms 3 sp^2 hybrid orbitals, leaving one p -orbital in C-atom unhybridized. The sp^2 carbon hybrid orbitals are known to form a different bond length, strength and geometry when compared to other hybridized molecular orbitals. The sp^2 hybridization has one unpaired electron (π -electron) per C-atom. The three sp^2 hybrid orbitals ($2p_x$, $2p_y$, $2s$) of a C-atom arrange themselves in three-dimensional space to attain stable configuration. Therefore five σ -bonds are formed, one with neighbor carbon atom and one with the two hydrogen atoms for each of the carbons (2 carbons with 2 Hydrogens each one). Their geometry is trigonal planar geometry, where the bond angle between the sp^2 hybrid orbitals is 120° . The unmixed pure p_z orbital lies perpendicular to the plane of the three sp^2 -hybrid orbitals. The remaining out of plane (delocalized) p_z -orbitals, each occupied by one e^- , overlap with neighboring p_z orbitals to form π -bonds (π -bonds are not as strong as σ -bonds) along the entire polymer backbone, which is the reason for the conducting properties of conjugated polymers. The overlapping of p_z -orbitals creates a system of delocalized π - e^- s, which can result in interesting and useful optical and electronic properties. Furthermore, the π - e^- s can be easier moved from one bond to the other, what makes conjugated polymers to be two-dimensional (2-D) semiconductors.⁷⁷

For example, the carbon-carbon double bond in ethene consists of one σ -bond, formed by the overlap of two sp^2 orbitals, and a π -bond, which is formed by the side-by-side overlap of the two unhybridized $2p_z$ orbitals from each carbon (Figure 1.2a). If the numbers of carbon atoms are increased as in the case of conjugated polymers (e.g. polyacetylene, Figure 1.2b), it forms a continuous band-like (π -band) behavior. The wave function of each $2p_z$ electron overlaps together and gives a delocalized π -band that stretches over a segment of the polymer

⁷⁷ J. Weidner, *Organic Semiconductor Materials and Devices*, 25, 2005.

backbone. The π -bonds are, thus, considered as the basic source of charge transport band in the conjugated systems. [5][6]

That overlap of p_z orbitals forms two molecular orbitals, a bonding π -orbital which is the highest occupied molecular orbital (HOMO) and an antibonding π^* -orbital which is the lowest unoccupied orbital (LUMO). The π and π^* -orbital are equivalent to the valence band (VB) and conduction band (CB) of an inorganic semiconductor, respectively.

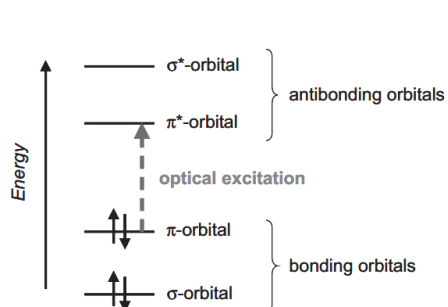


Figure 2.6 The energy levels of a π -conjugated molecule. The lowest electronic excitation is between the bonding π -orbital and the antibonding π^* -orbital⁷⁸.

The difference between the HOMO and LUMO is called band gap (E_g) of the organic material. The optical and electrical properties of an organic material are mostly determined by its E_g . In addition,

E_g is reduced when the polymer chain is getting longer. The chemical structure and schematic drawing of ethane is illustrated in Figure 2.6, which is the simplest example of a conjugated molecule.

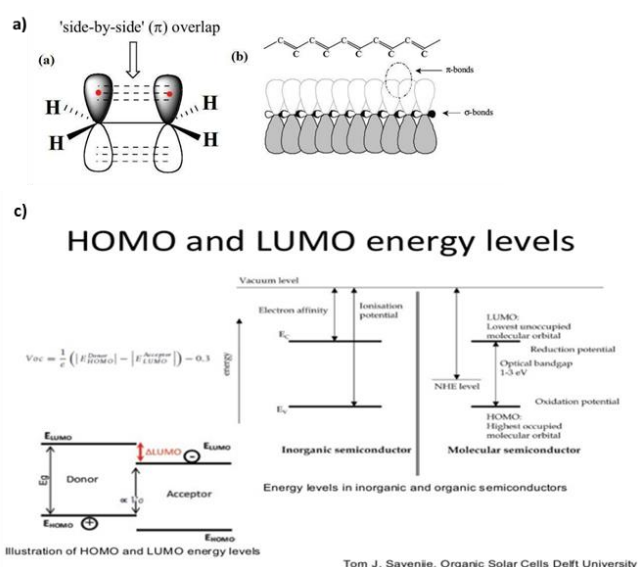


Figure 2.7 (a) The side-by-side overlaps of the two unhybridized $2p_z$ orbitals in ethane. (b) The molecular structure of polyacetylene (top), for clarity hydrogen atoms are not shown. The alternating double and single bonds indicate that the polymer is conjugated. The schematic representation of the electronic bonds in polyacetylene is depicted in the bottom panel. The p_z -orbitals overlap to form π - bonds and (c) schematic HOMO and LUMO levels of C.

The VB and CB are characterized by their ionization potential and electron affinity, respectively (Figure 2.7c). The ionization potential (IP) refers to the upper state of the valence band (π -state; the energy required to pull an electron from the highest point) and corresponds to the highest occupied molecular orbital (HOMO). Similarly, the electron affinity (EA) of a semiconducting polymer corresponds to the lowest state of the conduction band (π^* state the energy required to inject an electron) or the lowest unoccupied molecular orbital (LUMO)

The energy levels of these bands are reliant on the length of the conjugated segments. Figure 2.8 indicates how the band-gap of organic materials varies with respect to the number of carbon atoms participating to the conjugation length. Nevertheless, parameters such as chain defects, metallic impurities and the structure of the polymer affect the energy levels or the

⁷⁸ K.P.C. Vollhardt, Organische Chemie, Weinheim, 1990.

value of the band-gap of a given polymer. Depending on the structure, the type and amount of impurities, the band-gap of semiconducting polymers varies from 0.8 up to 4 eV. If the band gap of a polymer is much greater than 3 eV, the polymer is considered as insulator and therefore electron transfer between the bands are very limited.

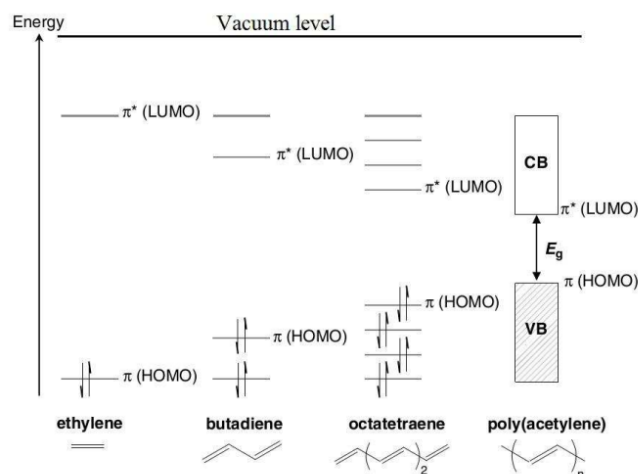


Figure 2.8 The evolution of the molecular orbital diagram (π -levels) with the number of monomer units⁷⁹.

The energy gap of conjugated polymers can be determined from optical, electrochemical and other spectroscopic measurements.⁷⁹ Most semiconducting conjugated polymers have band gaps of the order of those detailed in Table 2.1. The band gaps indicated in Table 1 are well correlated for absorption

of visible light. This means that the electrons can interact with light, and it is this property that is exploited in many optoelectronic applications, particularly in OPVs.

Table 2.1: The band gap of some conjugated polymers.⁸⁰

Polymer	Band gap (eV)
<i>Trans</i> -polyacetylene	1.4 – 1.5
Polythiophene	2.0 – 2.1
Poly(<i>p</i> -phenylene)	2.7
Poly(<i>p</i> -phenylenevinylene)	2.5
Polypyrrole	3.2
Poly[3,4-(ethylenedioxy)thiophene]	1.6

Another example of conjugated polymers is depicted in Figure 2.9, which represents the chemical structure of Poly({4,8-bis[(2-ethylhexyl)oxy]benzo-[1,2-b:4,5 b']dithiophene-2,6-diyl}{3 fluoro -2-[(2ethylhexyl)carbonyl]thieno -[3,4-b]thiophenedi-yl}) (PTB₇) polymer

which, was used in a big amount of fabricated devices as the electron donor material.

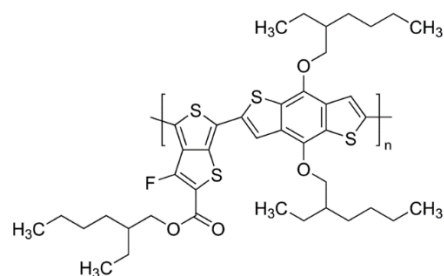


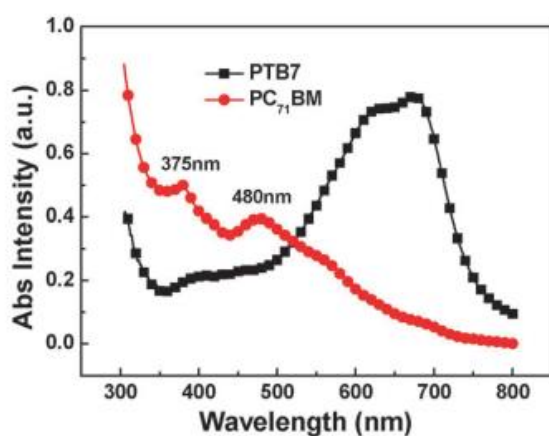
Figure 2.9 Molecular type of PTB₇ polymer.⁸¹

⁷⁹ W.R. Salaneck, R.H. Friend, J.L. Bredas, Phys. Rep., 1999, 319, 231.

⁸⁰ A. de Cuendias, R.C. Hiorns, E. Cloutet, L. Vignau, H. Cramail, Polymer Int. 2010, 59, 1452.

⁸¹ http://www.sigmaaldrich.com/catalog/product/aldrich/772410?lang=en®ion=GR&gclid=Cj0KEQjwi7vIBRDp09W8y7Ct6ZcBEiQA1CwV2Ees_HZcwXDtemRiODKR1JRb5UjLBNqs9rMIWoH2C9saAts-8P8HAQ

PTB₇ belongs in the family of novel semiconducting polymers based on alternating ester substituted thieno[3,4-b]thiophene and benzodithiophene units.⁸² These polymers exhibit a synergistic combination of properties that lead to an excellent photovoltaic effect. The



stabilization of quinoidal structure from thieno-[3,4-b]thiophene results in a low bandgap of the polymer of about 1.6 eV, showing efficient absorption around the region with the highest photon flux of the solar spectrum (about 700 nm), as shown in Figure 2.10.

Figure 2.10 Absorption spectra of PTB₇ pure polymer film and blend acceptor material PC₇₁BM.⁸³

The rigid backbone results in a good hole mobility of the polymer, and the side chains on the ester and benzodithiophene enable good solubility in organic solution and suitable miscibility with the fullerene acceptor. The introduction of fluorine into the thieno[3,4-b]thiophene provides the polymer with a relatively low-lying highest occupied molecular orbital (HOMO) energy level, which offers enhanced V_{oc} . All these advantages of thieno[3,4-b]thiophene and benzo-dithiophene polymers (PTBs) make them good candidates for BHJ polymer/fullerene solar cell application. PTB₇ exhibits an excellent photovoltaic effect therefore it is the first polymer that has reached a PCE over 7% (in a solution with the fullerene derivative phenyl-C₇₁-butyric acid-methyl-ester or PC₇₁BM as the electron acceptor), about 7.4%. The branched side chains in ester and benzo-dithiophene render the polymer good solubility in organic solvents. The HOMO and LUMO energy levels of PTB₇ are -5.15 eV and -3.31 eV. Although the side chains are branched, the PTB₇ has a relatively high hole mobility⁸³. The absorption spectrum of pure PTB₇ film is showed in Figure 2.10. The polymer shows strong absorption from 550 to 750 nm. However the absorption from 300 to 500 nm is relatively weak. To compensate the absorption of PTB₇, PC₇₁BM, which has strong absorption in the visible range is used as the acceptor, as previously mentioned. The resulting PTB₇/PC₇₁BM blend film exhibits a strong absorption covering a range from 300 to about 800 nm (Fig. 2.10).

2.2.2 Low Band Gap (LBG) Polymers

Low band gap (LBG) semiconducting polymers, with an absorption cut-off in the NIR region are of great interest for organic photovoltaics (OPV), organic photodetectors (OPDs), ambipolar

⁸² Y. Liang, Y. Wu, D. Feng, S.-T. Tsai, H.-J. Son, G. Li, L. Yu, J. Am. Chem. Soc., 2009, 131, 56.

⁸³ D. Huang, Y. Li, Z. Xu, S. Zhao, L. Zhao, J. Zhao, Phys. Chem. Chem. Phys., 2015, 17, 8053.

field-effect transistors (FETs) and bio-imaging applications.^{84,85,86,87,88} Intense efforts have been devoted of synthesizing new polymers for such applications, and tremendous progress has been made. Among the various classes of LBG conjugated polymers, diketopyrrolopyrrole (DPP) polymers have attracted considerable attention, and new materials were designed resulting in PCEs above 8% in polymer solar cells^{89,90,91} and in hole and electron mobilities of 17,8 and 6,3 $\text{cm}^2\text{V}^{-1}\text{s}^{-1}$ in FETs.^{92,93} Despite these efforts, it is notoriously difficult to establish thorough structure-property relationships that will be required to further optimize existing high-performance polymers to their intrinsic limits. Especially, the DPP polymers can be tuned via their aromatic substituents, their alkyl side chains, and the nature of the π -conjugated segment linking the units along the polymer chain.^{88,94}

The rigid backbone of conjugated polymers and their characteristic feature to aggregate via π - π stacking impart a reduced solubility on these materials in common organic solvents.⁹⁵ In general, to address these difficulties in the field of polymeric semiconductors various alkyl side chains are screened and employed in the polymer backbone.⁹⁶ Alkyl chains are the most commonly used side chains in polymeric semiconductors and initially their role was as solubilizing groups to ensure polymer solubility in organic solvents and easy processability towards thin film formation.⁹⁷ However, more and more studies have demonstrated the substantial impact of the flexible chains in the supramolecular self-assembly through different intermolecular interactions of the polymer chains^{98,99} and consequently on their charge transporting properties and device performances. Even a subtle change of the flexible chains may result in a great influence on device performance.^{100,101,102} Some parameters that contribute on the different molecular packing include the length of the side chains^{103,104} as well

⁸⁴ Z. Guo, S. Park, J. Yoon and I. Shin, *Chem. Soc. Rev.*, 2014, 43, 16.

⁸⁵ J. D. Yuen, R. Kumar, D. Zakhidov, J. Seifter, B. Lim, A. J. Heeger and F. Wudl, *Adv. Mater.*, 2011, 23, 3780.

⁸⁶ L. Dou, Y. Liu, Z. Hong, G. Li and Y. Yang, *Chem Rev.*, 2015, 115, 12633.

⁸⁷ X. Guo, M. Baumgarten and K. Müllen, *Prog. Polym. Sci.*, 2013, 38, 1832.

⁸⁸ C. B. Nielsen, M. Turbiez and I. McCulloch, *Adv. Mater.*, 2013, 25, 1859.

⁸⁹ K. H. Hendriks, G. H. L. Heintges, V. S. Gevaerts, M. M. Wienk and R. A. J. Janssen, *Angew. Chem. Int. Ed.*, 2013, 52, 8341.

⁹⁰ H. Choi, S.-J. Ko, T. Kim, P.-O. Morin, B. Walker, B. H. Lee, M. Leclerc, J. Y. Kim and A. J. Heeger, *Adv. Mater.*, 2015, 27, 3318.

⁹¹ R. S. Ashraf, I. Meager, M. Nikolka, M. Kirkus, M. Planells, B. C. Schroeder, S. Holliday, M. Hurhangee, C. B. Nielsen, H. Sirringhaus and I. McCulloch, *J. Am. Chem. Soc.*, 2015, 137, 1314.

⁹² B. Sun, W. Hong, Z. Yan, H. Aziz and Y. Li, *Adv. Mater.*, 2014, 26, 2636.

⁹³ J. Y. Back, H. Yu, I. Song, I. Kang, H. Ahn, T. J. Shin, S.-K. Kwon, J. H. Oh and Y.-H. Kim, *Chem. Mater.*, 2015, 27, 1732.

⁹⁴ W. Li, K. H. Hendriks, M. M. Wienk and R. A. J. Janssen, *Acc. Chem. Res.*, 2016, 49, 78.

⁹⁵ C. L. Chochos and S. A. Choulis, *Prog. Polym. Sci.*, 2011, 36, 1326.

⁹⁶ T. Lei, J.-Y. Wang and J. Pei, *Chem. Mater.*, 2014, 26, 594.

⁹⁷ C. Wang, H. Dong, W. Hu, Y. Liu and D. Zhu, *Chem. Rev.*, 2012, 112, 2208.

⁹⁸ L. Ding, H.-B. Li, T. Lei, H.-Z. Ying, R.-B. Wang, Y. Zhou, Z.-M. Su and J. Pei, *Chem. Mater.*, 2012, 24, 1944.

⁹⁹ W. Li, K. H. Hendriks, A. Furlan, W. S. C. Roelofs, S. C. J. Meskers, M. M. Wienk and R. A. J. Janssen, *Adv. Mater.*, 2014, 26, 1565.

¹⁰⁰ L. Biniek, S. Fall, C. L. Chochos, D. V. Anokhin, D. A. Ivanov, N. Leclerc, P. Lévêque and T. Heiser, *Macromolecules*, 2010, 43, 9779.

¹⁰¹ T. Lei, J.-H. Dou and J. Pei, *Adv. Mater.*, 2012, 24, 6457.

¹⁰² C. L. Chochos, A. Katsouras, N. Gasparini, C. Koulogiannis, T. Ameri, C. J. Brabec and A. Avgeropoulos, *Macromol. Rapid Commun.*, 2017, DOI:10.1002/marc.201600614.

¹⁰³ H. Bronstein, D. S. Leem, R. Hamilton, P. Woebkenberg, S. King, W. Zhang, R. S. Ashraf, M. Heeney, T. D. Anthopoulos, J. deMello and I. McCulloch, *Macromolecules*, 2011, 44, 6649.

¹⁰⁴ X.-Y. Wang, F.-D. Zhuang, X. Zhou, D.-C. Yang, J.-Y. Wang and J. Pei, *J. Mater. Chem. C*, 2014, 2, 8152.

as substitution position,^{100,105} density^{106,107} and bifurcation point of branched alkyl chains.^{96,108} The optimum choice of alkyl side chain is not universal though for each polymer semiconductor and intensive screening is required during the chemical structure optimization. Specifically, for the DPP based conjugated polymers very few studies in alkyl side chain optimization have been presented so far in the fields of OPVs.^{97,109,110,111}

Another approach for DPP polymers is the systematically moving the alkyl-chain branching position away from the polymer backbone, which afforded to a new family of DPP polymers, the thieno[3,2-b]thiophene-diketopyrrolopyrrole or (DPPTT-T) polymers. By moving the branching point from its regular position relatively close to the polymer backbone, as in the original DPPTT-T polymer (**C1**), to positions further from the backbone, I. Meager and coworkers¹¹² aimed to determine whether the π - π stacking distance could be influenced and to evaluate the effect that this would have on the crystallinity, morphology, and photovoltaic properties. In this project **only C1** was tested as the host donor, where **Cn** refers to the number of linear carbon atoms between the alkylated nitrogen and the alkyl-chain branching point (see Fig. 2.11), were synthesized by copolymerization of their respective monomeric units with thiophene. The monomers were synthesized by alkylation of the DPPTT core with the corresponding alkyl iodide. All of the alkyl chains were synthesized from commercially available 2-octyl-1-dodecanol.

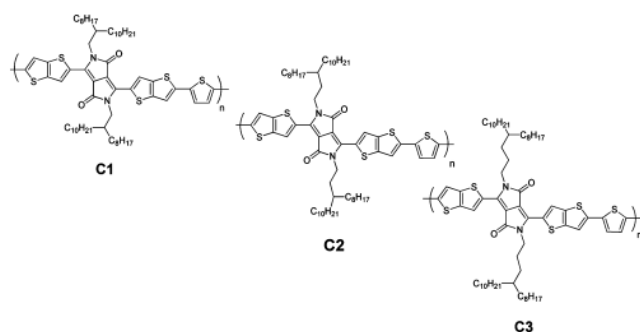


Figure 2.11 Chemical structures of DPPTT-T family polymers C1, C2, C3.

Low band gap polymers absorb light with wavelengths longer than 650 nm corresponding to a band gap lower than 2 eV. This means that they have a better overlap with the solar spectrum and can potentially

absorb more photons than common conjugated polymers (like P3HT) and thereby increase the current and efficiency of the solar cell.¹¹³ First, a comparison of the solar spectrum, shown as sun irradiance, with the absorption spectra of a low band gap polymer and commonly applied polymers in OPV, i.e. MEH-PPV and P3HT is shown in Figure 2.12.

¹⁰⁵ Wu, M. Wang, X. Qiao, Y. Xiong, Y. Huang, X. Gao and H. Li, *Macromolecules*, 2013, 46, 3887.

¹⁰⁶ R. J. Kline, D. M. DeLongchamp, D. A. Fischer, E. K. Lin, L. J. Richter, M. L. Chabinyc, M. F. Toney, M. Heaney and I. McCulloch, *Macromolecules*, 2007, 40, 7960.

¹⁰⁷ L. Biniek, S. Fall, C. L. Chochos, N. Leclerc, P. L  v  que and T. Heiser, *Org. Electron.*, 2012, 13, 114.

¹⁰⁸ I. Meager, R. S. Ashraf, S. Mollinger, B. C. Schroeder, H. Bronstein, D. Beatrup, M. S. Vezie, T. Kirchartz, A. Salleso, J. Nelson and I. McCulloch, *J. Am. Chem. Soc.*, 2013, 135, 11537.

¹⁰⁹ S. Y. Qu and H. Tian, *Chem. Commun.*, 2012, 48, 3039.

¹¹⁰ Y. Li, P. Sonar, L. Murphy and W. Hong, *Energy Environ. Sci.*, 2013, 6, 1684.

¹¹¹ M. A. Naik and S. Patil, *J. Polym. Sci. Part A: Polym. Chem.*, 2013, 51, 4241.

¹¹² I. Meager et al., *J. Am. Chem. Soc.*, 2013, 135, 31, 11537.

¹¹³ Bungaard et. al., *Solar Energy Materials and Solar Cells*, 2007, 91, 11, 954.

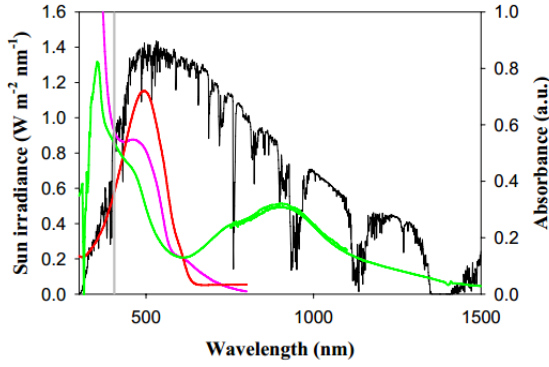


Figure 2.12. AM1.5 solar spectrum (black) and the film absorption spectra of MEH-PPV (pink), P3HT (red) and a low band gap polymer (green) from 300 to 1500 nm.⁴ The absorption below 400 nm is ascribed to the substrate (marked with the grey line).

When the photon flux is plotted as a function of the wavelength the maximum is shifted towards longer wavelengths, and hence, to absorb more photons a polymer that absorbs light at longer wavelengths

should be used (see Fig. 2.13). The photon flux ($f(\lambda)$) is achieved from the sun irradiance using equation 2.1, where $I_s(\lambda)$ is the sun irradiance in $\text{W m}^{-2} \text{nm}^{-1}$ and $E_\lambda(\lambda)$ is the photon energy in J determined from equation. 2.2.

$$f(\lambda) = \frac{I_s(\lambda)}{E_\lambda(\lambda)} \quad (2.1)$$

$$E_\lambda(\lambda) = h\nu = \frac{hc}{\lambda} \quad (2.2)$$

where, h is Planck constant ($6.626 \cdot 10^{-34} \text{ J*s}$), c is the speed of light ($2.998 \cdot 10^8 \text{ m s}^{-1}$) and λ is the wavelength in nm. The integrated photon flux ($F(\lambda)$) is calculated from the *photon flux* $f(\lambda)$ by equation 2.3, where A_s is the area under the sun irradiance curve determined from equation 2.4. The marginal values from 280 to 4000 nm are chosen, because the sun irradiance is close to zero beyond these limits.

$$F(\lambda) = \frac{\int_{\lambda=280}^{\lambda} f(\lambda) d\lambda}{A} = \frac{\Delta\lambda \cdot \sum_{\lambda=280}^{\lambda} f(\lambda)}{A} \quad (2.3)$$

$$A_s = \int_{\lambda=280}^{\lambda=4000} f(\lambda) d\lambda = \Delta\lambda \cdot \sum_{\lambda=280}^{\lambda=4000} f(\lambda) \quad (2.4)$$

The $F(\lambda)$ is then transformed into the **maximum theoretical current** (*integrated current*, I_t) by equation 2.5 assuming that one photon is converted to one electron in the OPV. So:

$$I_t = F(\lambda) * e \quad (2.5)$$

where, e is the elementary charge ($1.602 \cdot 10^{-19} \text{ C}$). The photon flux, the integrated photon flux and the integrated current are plotted as a function of the wavelength and we see that absorption at longer wavelengths results in a higher maximal theoretical current (see Figure 2.14).

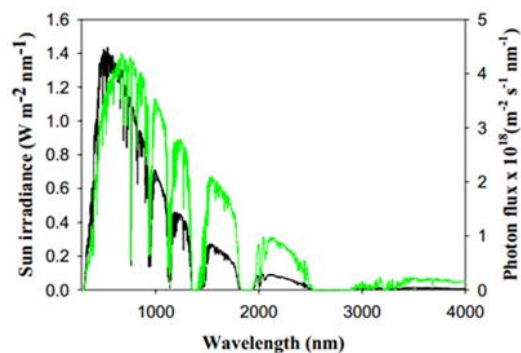


Figure 2.13 Solar irradiance (black) and photon flux (green) as a function of wavelength.

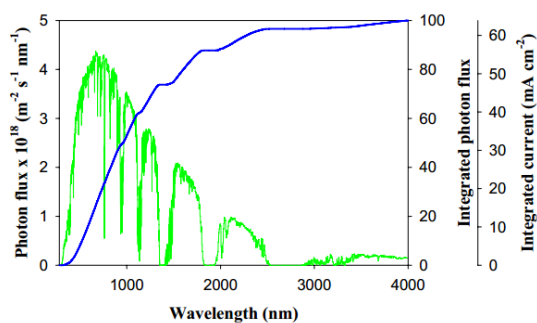


Figure 2.14 Photon flux as a function of wavelength (green). The integral (blue) is shown with two axes, one showing the integrated photons and one the theoretical current.

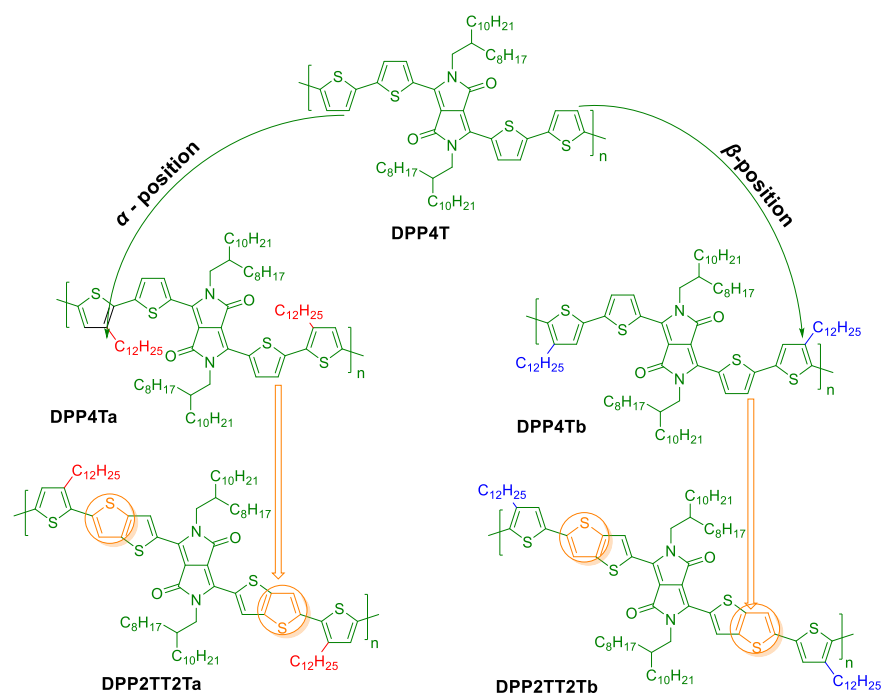
This phenomenon is illustrated with the example of two polymers, A and B. Polymer A absorbs light with wavelengths up to 500 nm and polymer B absorbs light with wavelengths up to 1000 nm. Figure 2.11 shows that polymer A absorbs $\approx 20\%$ of the photons and that polymer B absorbs almost $\approx 50\%$ of the photons in the solar spectrum. The maximum theoretical current, which can be achieved, is thus $\approx 12 \text{ mA cm}^{-2}$ for polymer A and $\approx 34 \text{ mA cm}^{-2}$ for polymer B. These values are all based on the assumption that the polymers absorb all the light from 280 to 600 and 1000 nm, respectively. This clearly shows that the low band gap polymers are of great importance, when the maximum theoretical current of the OPV, and hence the efficiency, has to be increased. In addition, by examining the solar irradiance and the absorption spectra of low band gap polymers (Fig. 2.13), it can be concluded that a higher short circuit current of OPV devices can be achieved (Fig. 2.14).

Therefore, using all those as a motivation, low band gap polymers have received more attention the past few years, since it is believed that they can improve the efficiency of the photovoltaic devices, due to a better overlap between the absorption spectra of the polymer and the solar spectrum.^{114,115} However, there are several other factors which affect the efficiency of an OPV device (see Chapter 3). Taking all these into consideration, in this part of the project, the efforts towards the establishment of a structure-photophysical properties-OPV performance and stability study has been accomplished in terms of alkyl side chain positioning and aromatic substituents optimization in LBG DPP based conjugated polymers¹¹⁶. In order to achieve this, the influence of anchoring two linear dodecyl side chains in two different positions namely alpha (α) and beta (β) at the two outer thiophene units in the backbone of a quaterthiophene based DPP copolymer (DPP4T) was examined by the synthesis of DPP4Ta (α -position) and DPP4Tb (β -position) (Scheme 1). Then, in order to study the impact of the flanked aromatic substituent of DPP, the thiophene rings have been replaced with the thieno[3,2-b]thiophene units through the synthesis of the DPP2TT2Ta and DPP2TT2Tb copolymers (Scheme 1).

¹¹⁴ A. Dhanabalan, J. K. J. van Duren, P. A. van Hal, J. L. J. van Dogen, R. A. J. Janssen, *Adv. Funct. Mater.*, 2001, 11, 255.

¹¹⁵ H. Neugebauer, C. J. Brabec, N. S. Sariciftci, R. Kiebooms, F. Wudl, S. Luzzati, *J. Chem. Phys.*, 1999, 110, 12108.

¹¹⁶ C. Magliione, A. Carella, R. Centore, P. Chávez, P. Lévêque, S. Fall, N. Leclerc, *Dyes Pigm.*, 2017, 141, 169.



Scheme 2.1. General chemical structures of the studied LBG DPP-based polymers.

The above LBG polymers have encoded names for pronunciation simplicity, so:

Table 2.1 The encoded names of the 5 different LBG polymers used.

Long name	Encoded name
DPP4T	cc72
DPP4Ta	cc52
DPP4Tb	cc44
DPP2TT2Ta	SD6
DPP2TT2Tb	SD5
DPPTT-T	C1 or cc165

2.2.3 Small Molecules

Solution-processed organic solar cells (OSCs) are drawing more and more attention currently because of the potential as a promising technology of green energy with the significant advantages of low cost, lightweight, and high mechanical flexibility.^{117,118,119} Meanwhile, solution-processed small molecule-based solar cells (SMSCs) are emerging as a competitive alternative to their polymer counterparts due to some promising advantages, including low molecular weight, weak intermolecular interaction,¹²⁰ well-defined structure thus less batch-

¹¹⁷ H. X. Zhou, L. Q. Yang, W. You, *Macromolecules*, 2012, 45, 607.

¹¹⁸ Y. Z. Lin, Y. F. Li, X. W. Zhan, *Chem. Soc. Rev.*, 2012, 41, 4245.

¹¹⁹ Y. J. Cheng, S. H. Yang, C. S. Hsu, *Chem. Rev.*, 2009, 109, 5868.

¹²⁰ Y. Yang, G. Li, *Fundamentals, Materials, Devices and Fabrication*, 2015.

to-batch variation,^{121,120} versatile molecular structure, and easier band structure control.¹²² As well, in most cases solubilizing side chains are required that allow solution-processing for solar cells. Recently, prominent efficiencies with 6–7% have been achieved for small molecule bulk hetero-junction (SM BHJ) solar cells,¹²³ which is closing the performance gap with the best PSCs. However, SM BHJ solar cells have not been investigated as intensively as PSCs, and their overall performances are still behind those of their polymer counter-parts. Furthermore, many techniques for polymer-based BHJ solar cells could be applied for SM BHJ devices.

Currently, the active materials, especially the donor materials are still the most important key factor for high PCEs of SMSC devices. To address this issue, it is believed that several requirements should be considered collectively to design small molecules for high performance and solution processed SMSCs. These include: excellent film formation ability, wide and efficient absorption, matched energy levels with acceptors, planar structure for high hole mobility, and good solubility and chemical and thermal stability. It is important to note that the design of small molecules with good film formation ability is a prerequisite for high performance solution-processed BHJ devices, since it has been generally difficult for small molecules to form comparably good quality film as polymers, especially those molecules with relatively low molecular weights and rigid planar structures owing to their intrinsic aggregation.¹²⁴

During the experiments, the conjugated small molecule (CSM) named compound T (see Scheme 2.2), which contained 4,7-dithienbenzothiadiazole as central unit, thiophene rings as the terminal and cyanovinylene bonds, was used as the third component into the standard PTB7:PC₇₁BM active layer (Reference). That CSM was successfully prepared by a five-step synthetic route and it is consisted of donor–acceptor segments. In particular, the central 4,7-dithienbenzothiadiazole unit was connected with two phenyl or thiophene rings via a cyanosubstituted vinylene bond. This approach is widely utilized to reduce the band gap of conjugated molecules.^{125,126} Inverted Ternary (see Ch. 5) Bulk heterojunction organic solar cells (ITBHJSCs) were fabricated and evaluated. Related compounds containing benzothiadiazole and thiophene moieties have been used recently as electron donors for BHJSCs.^{127,128}

¹²¹ T. Vangerven et. al., *Chem. Mater.*, 2016, 28, 24, 9088.

¹²² J. Zhao et. al., *RSC Adv.*, 2016, 6, 60595.

¹²³ L. Lisheng, L. Xiao, H. Qin, K. Gao, J. Peng, Y. Cao, F. Liu, T. P. Russell, X. Peng, *ACS Appl. Mater. Interfaces*, 2015, 7, 38, 21495.

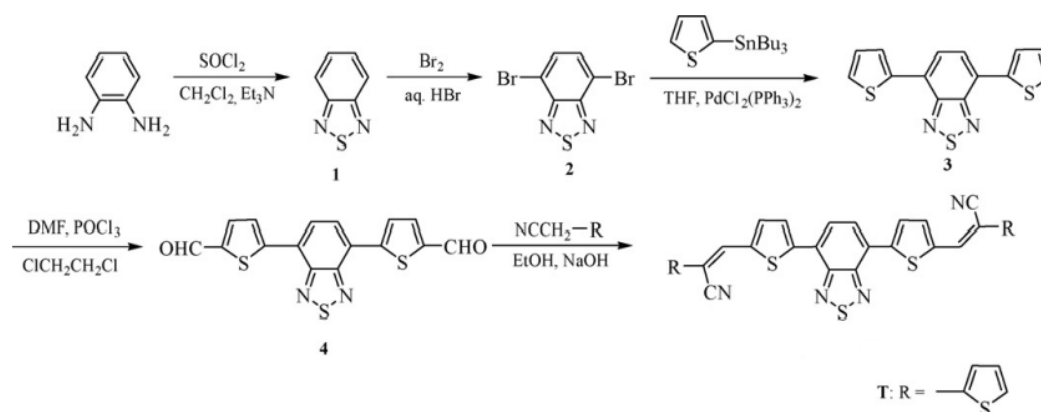
¹²⁴ H. Usta, A. Facchetti, A. *Polymeric and Small-Molecule Semiconductors for Organic Field-Effect Transistors, in Large Area and Flexible Electronics*, 2015.

¹²⁵ A. Kraft, A.C. Grimsdale, A.B. Holmes, *Angew. Chem. Int. Ed.*, 1998, 37, 402.

¹²⁶ N.S. Cho, D.H. Hwang, B.J. Jung, J. Oh, H.Y. Chu, H.K. Shim, *Synth. Met.*, 2004, 143, 277.

¹²⁷ Y. Jeon, T.-M. Kim, J.-J. Kim J.-I. Hong, *New J. Chem.*, 2015, 39, 9591.

¹²⁸ P. Zhou, Z.-G. Zhang, Y. Li, X. Chen, J. Qin, *Chem. Mater.*, 2014, 26, 11, 3495.



Scheme 2.2. Synthesis of compound T.¹²⁹

2.2.4 Fullerenes, Fullerene Derivatives/Electron Acceptor materials

Electron acceptor: A molecule that receives or accepts electrons from the donor and thus ensures charge separation.

In 1985, fullerenes discovered by researchers at Rice University. They are a category of carbon allotropes named after *Buckminster Fuller*.¹³⁰ They are molecules composed entirely of carbon, in the form of a hollow sphere, ellipsoid, or tube. Spherical fullerenes are sometimes called bucky balls, the C₆₀ variant is often compared to a typical white and black soccer football. Cylindrical fullerenes are called bucky tubes. Recently discovered is the "bucky egg", by researchers at UC Davis.¹³¹ Fullerenes are similar in structure to graphite, which is composed of a sheet of linked hexagonal rings, but they contain pentagonal (or sometimes heptagonal) rings that prevent the sheet from being planar. Some significant properties of Fullerenes are: high symmetry, thus exhibit very high values of electron-affinity,¹³² ability to stabilize negative charge¹³³ very high electron mobility¹³⁴), making some of its soluble derivatives the best electron-acceptors currently available for polymer photovoltaics.¹³⁵

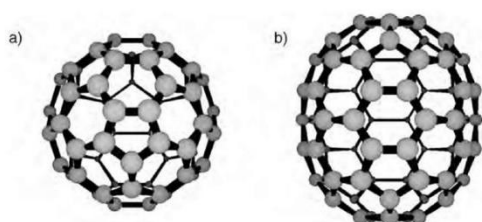


Figure 2.8 The two most common used fullerenes: a) C₆₀ and b) C₇₀.¹³⁶

Structurally, Fullerene C₆₀ has well-symmetric structure and exhibits good electron mobility, and as known, one molecule of C₆₀ can receive four electrons. Therefore, C₆₀ and its derivatives can be

¹²⁹ J. A. Mikroyannidis, M. M. Stylianakis, Q. Dong, Y. Zhou, W. Tian, *Synth. Mat.*, 2009, 159, 14, 1471.

¹³⁰ Jean-François Nierengarten, *Fullerenes and Other Carbon-Rich Nanostructures*, 2014.

¹³¹ UC Davis news, <http://www.news.ucdavis.edu>

¹³² P.-M. Allemand, A. Koch, F. Wudl, *J. Am. Chem. Soc.*, 1991, 113, 1050.

¹³³ J. Chlistunoff, D. Cliffl and A. J. Bard, *Organic Conductive Molecules and Polymers*, Chichester, 1997, 1, 7, 333.

¹³⁴ E. Frankevich, Y. Maruyama and H. Ogata, *Chem. Phys. Lett.*, 1993, 214, 39.

¹³⁵ *Organic Photovoltaics: Materials, Device Physics, and Manufacturing Technologies*, C. J. Brabec, V. Dyakonov U. Scherf, Weinheim, 2008.

¹³⁶ <http://what-when-how.com/nanoscience-and-nanotechnology/fullerenes-chemistry-nanotechnology/>

used as electron acceptor materials. In 1992, *Sariciftci et al.* first used C_{60} as electron acceptor¹³⁷ and discovered the photo-induced ultrafast electron transfer between electron donor and acceptor. Although, C_{60} can be dissolved in Chlorobenzene (CB) and Dichlorobenzene (DCB), it exhibits very limited solubility in most of the commonly used organic solvents. In order to improve its solubility and also to avoid severe phase separation of Donor/Acceptor blend, [6,6]-phenyl-C61-butyric acid methyl ester (PC₆₀BM) was applied in OPVs. In 1995 *Yu et al.* showed that charge separation is greatly improved when donor and acceptor materials are mixed in a bicontinuous interpenetrating network¹³⁸. In the past decade, PC₆₀BM and its corresponding C_{70} derivative (PC₇₀BM) have been dominantly used as acceptors in OPVs. In comparison with PC₆₀BM, PC₇₀BM possesses stronger absorption in visible range, and hence it attracted much interest recently.¹³⁹

However, C_{70} is much expensive than that of C_{60} due to its tedious purification process, which limits its application. The molecular structures of PC₆₀BM, PC₇₀BM are shown in Fig. 2.9. PC₆₀BM is crystalline dark-brown powder, and possesses good solubility in common organic solvents such as Chloroform, Toluene and o-Dichlorobenzene (O-DCB).

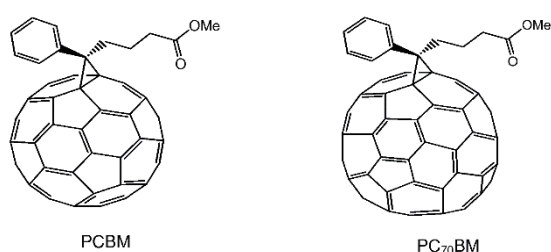


Figure 2.9 Fullerene derivatives a) PC₆₀BM b) PC₇₀BM¹⁴⁰.

Both the two materials show strong absorption at ultraviolet region, from 200 to 400 nm, but PC₇₀BM shows stronger absorption in visible region compared to

PC₆₀BM.

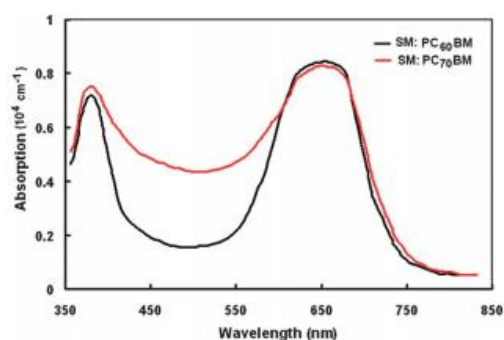


Figure 2.10 Optical absorption spectra of small molecule (SM):PC₆₀BM and SM:PC₇₀BM blends in thin film form.¹⁴¹

Thus, OPV devices use PC₇₀BM as acceptor in order to harvest more sunlight and as a result it is shown higher J_{sc} and hence better PCE values¹⁴² than that of PC₆₀BM-based devices.¹⁴³

The electrochemical properties and energy level of the fullerene derivatives is very important for OPVs. As it is shown in Fig. 2.10, PC₆₀BM has a 4.2 eV LUMO and 6.0 eV HOMO level and PC₇₀BM 4.2 eV and 6.1 eV respectively.

¹³⁷ Katz, E.A. *Phys. Solid State*, 2002, 44, 647.

¹³⁸ G. Yu, J. Gao, J. C. Hummelen, F. Wudl, and A. J. Heeger, *Science*, 1995, 270, 1789.

¹³⁹ J.-F. Nierengarten, *Fullerenes and Other Carbon-Rich Nanostructures*, 2014.

¹⁴⁰ <http://www.google.com/patents/WO2008060716A2?cl=en>

¹⁴¹ G. D. Sharma, J. A. Mikroyannidis, R. Kurchaniac, K. R. J. Thomas, 28, 2012.

¹⁴²

¹⁴³ F. Liu, W. Zhao, J. R. Tumbleston, C. Wang, Y. Gu, D. Wang, A. L. Briseno, H. Ade, T. P. Russell, *Adv. Energy Mater.*, 2014, 4, 301377.

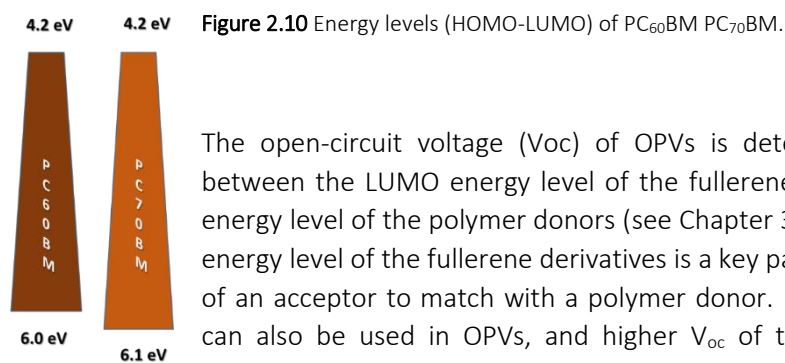


Figure 2.10 Energy levels (HOMO-LUMO) of PC₆₀BM PC₇₀BM.

The open-circuit voltage (V_{oc}) of OPVs is determined by the difference between the LUMO energy level of the fullerene acceptors and the HOMO energy level of the polymer donors (see Chapter 3.2.2). Therefore, the LUMO energy level of the fullerene derivatives is a key parameter for the application of an acceptor to match with a polymer donor. Furthermore, multi-adducts can also be used in OPVs, and higher V_{oc} of the device can be realized. Therefore, [6,6]-phenyl-C60-butyric acid methylester¹⁴⁴ (PC₆₀BM) and [6,6]-phenyl-C71-butyric acid methylester¹⁴⁵ (PC₇₀BM) are still employed in most efficient polymer solar cells.

2.3 Buffer layers

One problem with BHJ solar cells is that both the donor polymer and the acceptor molecule (PCBM) are “touching” both electrodes. This means that electrons in the PCBM may be formed at an interface very close to the ITO cathode, which typically collects the electrons (referring to an Inverted structure). Any electrons transferred to the ITO would essentially recombine (losses) with holes and reduce the working voltage of the device. Thus the Open circuit voltage, V_{oc} (Ch. 3.2.2), would also be reduced. A similar effect should take place at the cathode if holes are produced in the High occupied molecular orbital, HOMO, of the polymer near the Negative electrode (Ch. 2.6). So it is quite clear, that there are needed materials that would abort the impact of those losses. Therefore, the structure of OSCs usually includes functional layers at the active layer/electrode interfaces. These additional layers, called buffer layers or interfacial layers or interlayers, can no more be consider as “optional”, but are essential for achieving maximum performance in OSCs. So, the usual structures include always a Cathode Buffer layer (CBL) and an Anode Buffer layer (ABL), as shown in Fig. 210.

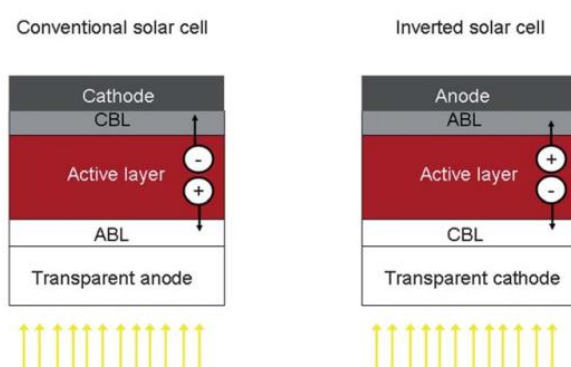


Figure 2.10 Typical device structures of single-junction conventional and inverted polymer solar cells.¹⁴⁶

¹⁴⁴ J. C. Hummelen, B. W. Knight, F. LePeq, F. Wudl, J. Yao and C. L. Wilkins, *J. Org. Chem.*, 1995, 60, 532.

¹⁴⁵ M. M. Wienk, J. M. Kroon, W. J. H. Verhees, J. Knol, J. C. Hummelen, P. A. van Hal and R. A. J. Janssen, *Angew. Chem., Int. Ed.*, 2003, 42, 3371.

¹⁴⁶ P. Riccardo, C. Carbonera, A. Bernardia, N. Camaioni, *Energy Environ. Sci.*, 2011, 4, 285.

2.3.1 Electron Transport/Hole Blocking material

Hole Blocking layer (HBL), when placed between the active layer blend and the ITO cathode, serves to prevent holes in the Polymer from traveling to the ITO cathode, thus forcing the holes to flow in the correct direction for collection, at the Aluminum (Al) Anode (see Ch. 3.1.2.1). Thus only electrons are allowed to travel through this material and reach the ITO Cathode.

In general, LiF¹⁴⁷ and Ca¹⁴⁸ are the most widely used electron-transport layers (ETLs). However, the Ca/Al electrode is very unstable if exposed to air without encapsulation of the device active area. The thickness and evaporation rate of LiF are also difficult to control ($\approx 0.8\text{--}1$ nm). For solution-processed ETLs, transition metal oxides (e.g., ZnO, TiOx)^{149,150} and some interesting polar organic ETLs such as fullerene derivatives (neutral or surfactant),^{151,152,153} non-conjugated polyelectrolytes (polyethylenimine derivatives such as PEIE, PEI structures shown in Fig. 2.4)^{154,155}, and conjugated polyelectrolytes such as polyfluorene derivatives, PFN, and PFCn6K (structures shown in Fig. 2.4)^{156,157,158,159,160,161} have been introduced into both conventional and inverted devices, and exciting performances have been achieved.

All inverted devices that fabricated during this thesis included a PFN ETL. PFN or full named Poly [(9,9-bis(3'-(N,N-dimethylamino)propyl)-2,7-fluorene)-alt-2,7-(9,9-dioctyl-fluorene)] exhibits good solubility in polar solvents such as methanol (MeOH), dimethylformamide (DMF) and dimethyl sulfoxide (DMSO) in the presence of a small quantity of Acetic acid (AA), which improved the solubility due to the weak interaction between the nitrogen atoms in the side chain and the AA.^{162,163}

¹⁴⁷ C. J. Brabec, S. E. Shaheen, C. Winder, N. S. Sariciftci, P. Denk, *Appl. Phys. Lett.*, 2002, 80, 1288.

¹⁴⁸ A. K. K. Kyaw, D. H. Wang, V. Gupta, W. L. Leong, L. Ke, G. C. Bazan, A. J. Heeger, *ACS Nano*, 2013, 7, 4569.

¹⁴⁹ H. L. Yip, S. K. Hau, N. S. Baek, H. Ma, A. K.-Y. Jen, *Adv. Mater.*, 2008, 20, 2376.

¹⁵⁰ J. Y. Kim, S. H. Kim, H. H. Lee, K. Lee, W. Ma, X. Gong, A. J. Heeger, *Adv. Mater.*, 2006, 18, 572.

¹⁵¹ C. E. Song, K. Y. Ryu, S. J. Hong, C. Bathula, S. K. Lee, W. S. Shin, J. C. Lee, S. K. Choi, J. H. Kim, S. J. Moon, *ChemSusChem*, 2013, 6, 1445.

¹⁵² C. H. Hsieh, Y. J. Cheng, P. J. Li, C. H. Chen, M. Dubosc, R. M. Liang, C. S. Hsu, *J. Am. Chem. Soc.*, 2010, 132, 4887.

¹⁵³ K. M. O'Malley, C. Z. Li, H. L. Yip, A. K.-Y. Jen, *Adv. Energy Mater.*, 2012, 2, 82.

¹⁵⁴ B. Kippelen, *Science*, 2012, 336, 327.

¹⁵⁵ H. Kang, S. Hong, J. Lee, K. Lee, *Adv. Mater.*, 2012, 24, 3005.

¹⁵⁶ Z. He, C. Zhong, S. Su, M. Xu, H. Wu, Y. Cao, *Nat. Photonics*, 2012, 6, 591.

¹⁵⁷ Z. He, C. Zhong, X. Huang, W. Y. Wong, H. Wu, L. Chen, S. Su, Y. Cao, *Adv. Mater.*, 2011, 23, 4636.

¹⁵⁸ J. H. Seo, A. Gutacker, Y. Sun, H. Wu, F. Huang, Y. Cao, U. Scherf, A. J. Heeger, G. C. Bazan, *J. Am. Chem. Soc.*, 2011, 133, 8416.

¹⁵⁹ S. H. Liao, Y. L. Li, T. H. Jen, Y. S. Cheng, S. A. Chen, *J. Am. Chem. Soc.*, 2012, 134, 14271.

¹⁶⁰ J. Kesters, T. Ghooos, H. Penxten, J. Drijkoningen, T. Vangerven, D. M. Lyons, B. Verreet, T. Aernouts, L. Lutsen, D. Vanderzande, J. Manca, W. Maes, *Adv. Energy Mater.*, 2013, 3, 1180.

¹⁶¹ Y. M. Chang, R. Zhu, E. Richard, C. C. Chen, G. Li, Y. Yang, *Adv. Funct. Mater.*, 2012, 22, 3284.

¹⁶² B. Liu, W. L. Yu, Y. H. Lai, W. Huang, *Macromolecules*, 2002, 35, 4975.

¹⁶³ B. Liu et al., *Conjugated polyelectrolytes : fundamentals and applications*, Wiley, 2013.

2.3.2 Hole transport/Electron Blocking material

This layer provides an electron blocker (EB) between the active layer blend and the AL anode that serves to prevent electrons in the Acceptor material from traveling to the Cathode, thus forcing the electrons to flow in the correct direction for collection at the ITO Cathode (see Ch. 3.1.2.1). Thus only holes are allowed to travel through this material and reach the AL Anode.

Poly(3,4-ethylenedioxythiophene):poly(styrenesulfonate) (PEDOT:PSS) is most often used as the hole transport layer (HTL) because of its advantages of:

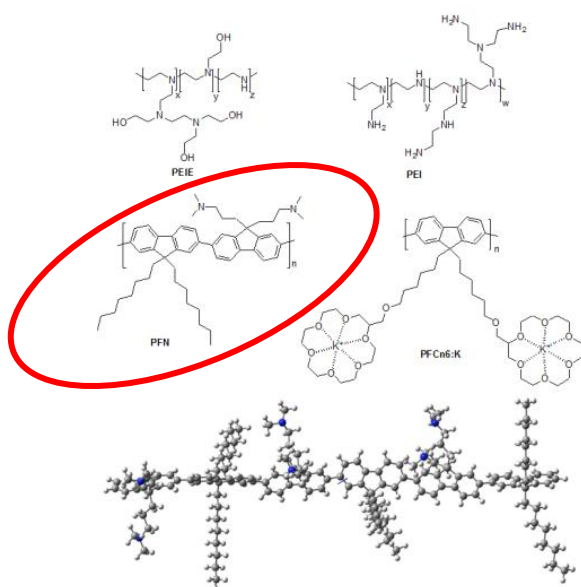


Figure 2.4 Chemical structures of the water/alcohol soluble non-conjugated and conjugated polyelectrolytes, the geometry for the **PFN** trimer is optimized by DFT calculation.¹⁶⁴

high transparency, high work function, smooth surface, high conductivity, and easy solution process.¹⁶⁵ However, the acidic (pH \approx 1) and hygroscopic properties of PEDOT:PSS¹⁶⁶ always result in a dramatic degradation of the PSCs in ambient conditions. Transition metal oxides, such as MoO₃, V₂O₅, NiO, WO₃, ReO₃, and RuO₂, have been successfully demonstrated as alternatives to PEDOT:PSS,^{167,168} based on their good stability in polymer solar cells. Among these transition metal oxides, MoO₃ has been

paid great attention for its high transmittance, nontoxicity, and high work function. The deposition of MoO₃ before the positive aluminum electrode (referring to inverted structure) is occurred mainly through thermal evaporation (Ch. 6.5).

¹⁶⁴ G. Long, X. Wan, B. Kan, Z. Hu, X. Yang, Y. Zhang, M. Zhang, H. Wu, F. Huang, S. Su, Y. Cao, Y. Chen, *ChemSusChem*, 2014, 7, 2358.

¹⁶⁵ Y. Cao, G. Yu, C. Zhang, R. Menon, A. J. Heeger, *Synth. Met.*, 1997, 87, 171.

¹⁶⁶ E. Voroshazi, B. Verreet, A. Buri, R. Müller, D. Di Nuzzo, P. Heremans, *Org. Electron.*, 2011, 12, 736.

¹⁶⁷ J. Meyer, A. Shu, M. Kröger, A. Kahn, *Appl. Phys. Lett.*, 2010, 96, 133308.

¹⁶⁸ M. T. Greiner, M. G. Helander, W.-M. Tang, Z.-B. Wang, J. Qiu, Z.-H. Lu, *Nat. Mater.*, 2012, 11, 76.

Chapter 3: Organic Solar Cells



Figure 3.1 A typical OSC¹⁶⁹.

Polymer solar cells have drawn a great deal of attention due to the attractiveness of their remarkable properties: potentially lightweight, semitransparent and low fabrication cost. Recently,

numerous significant research efforts have resulted in polymer solar cells with power conversion efficiencies in up to 10%¹⁷⁰.

3.1 Structure and general operating principles of OPVs

3.1.1 Device structure

Careful selection of device architecture could improve OPV performance and increase its stability. OPV devices are comprised of a number of layers as it is shown in Figure 3.2. In the normal/conventional configuration (Fig. 3.2a,b), a transparent substrate (glass or plastic) is coated with a transparent conductor that serves as the anode and its role is first to allow light to pass through, and second to collect holes from the device, in our case ITO is the material used. In between the anode and the absorbing active layer is a hole-transport buffer layer (or HTL) for conventional devices, that prevents electrons from reaching the anode, in most cases PEDOT:PSS has that role, which is detailed referred in the previous chapter. On the contrary, for inverted devices, there is an ETL that blocks holes reaching cathode. Then, the light absorbing photoactive BHJ layer containing the donor and acceptor material is sandwiched between two electrodes, where the second buffer layer is an ETL and a HTL for conventional and inverted devices, respectively. The last layer is the opposite electrode, the (optically reflective) metal cathode, where in most cases is Aluminum (AL). This layer is deposited by thermal evaporation (see Ch. 2.5.2.1 and Ch. 6.5). On the contrary, for Inverted OPVs, the device polarity is reversed compared to that based on the conventional structure, this means that the Anode/Cathode and HTL/ETL have opposite positions (compared to the conventional structure), so in this case the light path is: Cathode/ETL/Active layer/HTL/Anode. The aforementioned layers are detailed explained in the previous Chapter, where the materials used at the fabrication are presented.

¹⁶⁹ <http://spectrum.ieee.org/nanoclast/green-tech/solar/quantum-dot-solar-cells-break-conversion-efficiency-record>

¹⁷⁰ Nho. et al., *Energy Environ. Sci.*, 2016, 9, 240.

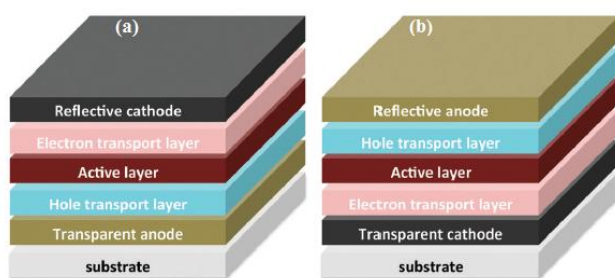


Figure 3.2 (a) a typical bulk hetero-junction device structure and (b) an inverted device architecture¹⁷¹.

Inverted polymer solar cells,¹⁷² showing power conversion efficiency comparable to those exhibited by conventional solar

cells,¹⁷³ present two main advantages: they often exhibit higher environmental stability with respect to the conventional structure and furthermore, they provide higher flexibility in the design of multi-junction or tandem polymer solar cells (Ch. 1.11). Inverted architectures are also generally more compatible with roll-to-roll processing, which is another substrate deposition method¹⁷⁴.

3.1.2 Device operation

Charge generation in organic semiconductors can take place by different means other than thermal excitation across the band-gap. Charges can be generated by either of the following mechanisms: (i) impurity excitation i.e. by introducing p-type and n-type dopants that create sub-gap levels from which thermal excitation can be efficient, this happens in conducting polymers and organic sensors (ii) through injection from electrodes e.g. this charge carrier generation is mainly observed in OLEDs and OTFTs (iii) or through photo-excitation i.e. excitons can be photo-induced and get dissociated into free electrons and holes either through electron transfer-induced dissociation or electric field-induced dissociation, this mechanism is mainly occurring in OPVs and photoconductors. Efficient photovoltaic operation, whether organic or inorganic based devices, relies upon the efficient separation of charges and their collection at the device electrodes. Unlike inorganic based PV devices where an electron and a hole are generated by an immediate light absorption (oppositely charged carriers are only weakly bound due to an efficient electrostatic screening), the charge generation (separation) in organic photovoltaic devices is a multistep process.

¹⁷¹ K. A. Mazzi, C. K. Luscombe, *Chemical Society Reviews*, 2015, 44, 78.

¹⁷² L.-M. Chen, Z. Hong, G. Li, Y. Yang, *Adv. Mater.*, 2009, 21, 1.

¹⁷³ S. Nam, J. Seo, S. Woo, W. H. Kim, H. Kim, D. D. C. Bradley, Y. Kim, *Nat. Comm.*, 2016, 8929, 6.

¹⁷⁴ S. B. Darling and F. You, *RSC Adv.*, 2013, 3, 17633–17648.

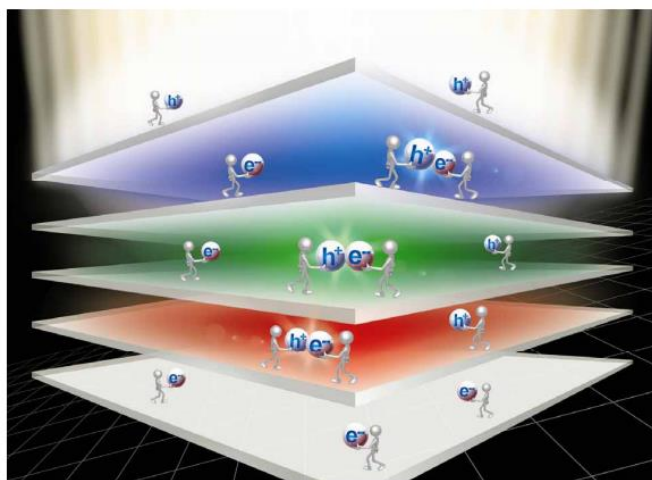


Figure 3.3 Exciton generation, dissociation and charge collection¹⁷⁵.

3.1.2.1 Exciton: generation, dissociation and charge collection.

In some applications it is useful to consider electronic excitation as if a quasi-particle, capable of migrating, were involved. This is termed as *exciton*. In organic materials two models are used: the band or wave model (low temperature, high crystalline order) and the hopping model (higher temperature, low crystalline order or amorphous state). Energy transfer in the hopping limit is identical with energy migration.

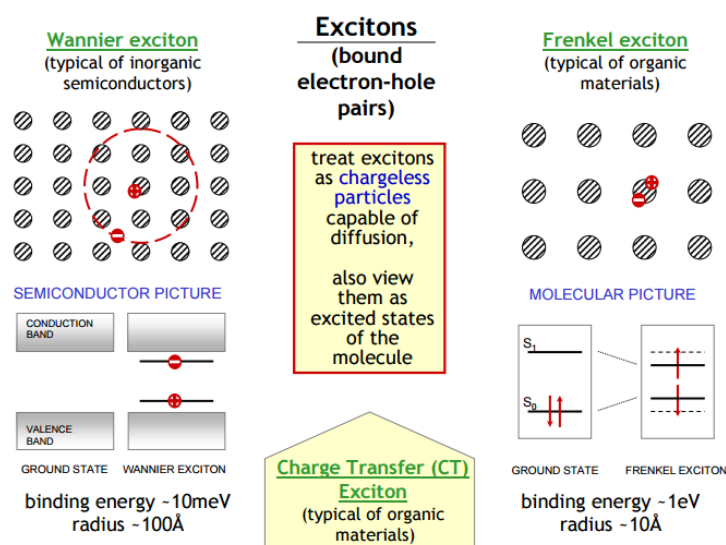


Figure 3.4 Differences of “organic” Frenkel and “inorganic” Wannier excitons¹⁷⁶.

As a result of the low dielectric constant ($n \approx 3$) in semiconducting polymer (organic) materials, the coulombic forces of attraction between electrons and holes are very high¹⁷⁷. This implies that unlike inorganic semiconductors, in which photo excitation generally

forms a free electron and hole excited states in semiconducting polymers form bound electron-hole pairs.

Bulk heterojunction (BHJ) structure is the most successful structure invented, in which a blend of donor and acceptor with a bi-continual phase separation can be formed. When the sunlight (photons) getting through the transparent electrode (ITO) is absorbed by the semiconducting donor and acceptor materials in the photoactive layer, excitons (bounded electron-hole pairs) are formed (an electron is excited from the polymer HOMO to its LUMO i.e. π to π^* transition)

¹⁷⁵ J. S. Brooks, 2010, *Chem. Soc. Rev.*, 39, 2667–94.

¹⁷⁶ *Electronic Processes in Organic Crystals and Polymers*, M. Pope, C.E. Swenberg

¹⁷⁷ W. Cai, X. Gong, Y. Cao, *Solar Energy Materials and Solar Cells*, 94 (2010) 114-127.

and then they diffuse to the interfaces of the donor/acceptor where the excitons dissociate into electrons on the LUMO level of the acceptor and holes on the HOMO level of the donor (Fig. 3.5). A driving force is required to overcome this excitonic binding energy (Coulomb bonding) so that free charge carriers can be produced and transported throughout the device, as it is illustrated in Fig. 3.5. The dissociated electrons and holes are driven by built-in electric field and then moved to negative and positive electrode, respectively, and then collected by the electrodes to realize the photon-to-electron conversion (Fig. 3.5).

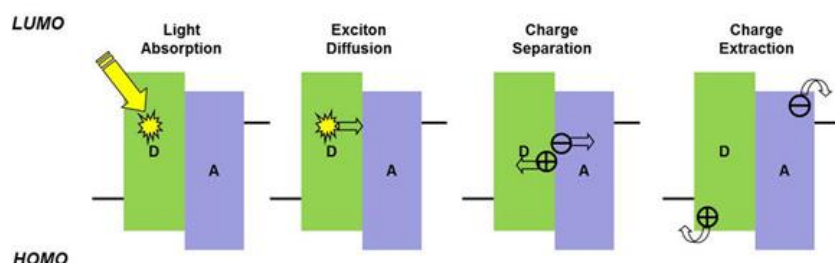


Figure 3.5 Steps from photon absorption to charge collection.¹⁷⁸

The force required to overcome the exciton binding energy (exciton dissociation) is provided by the energy level offset of the LUMO of the donor and the LUMO of the acceptor material (higher electron affinity of acceptor). Fig. 3.6 displays an energy band diagram of organic solar cells. This energy offset used to dissociate excitons is illustrated as ΔE_{ES} in Fig. 3.6, which is the excited state energy offset.

In order to dissociate excitons formed in the acceptor material, the energy offset of the highest occupied molecular orbital (HOMO) of the acceptor and the HOMO of the donor material is required. This energy offset used to dissociate excitons is illustrated as ΔE_{GS} in Fig. 3.6, which is the ground state energy offset. Excitonic dissociation due to these energy offsets occurs at the interface between the donor and acceptor phase, therefore, the arrangement of the two materials in the active layer is crucial for the successful operation of the device.

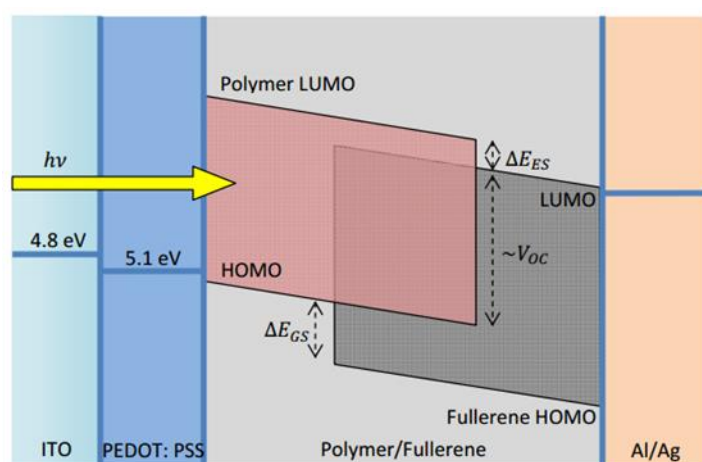


Figure 3.6 Energy band diagram of donor-acceptor materials in bulk heterojunction (BHJ) organic solar cells (SCs). Light path through the different layers of an OSC.

Exciton diffusion in organic semiconductors is crucial to the performance of organic solar cells. The diffusion length of excitons is very small, in order of 10 nm^{179,180}. The BHJ

structure is a successful approach in order to significantly increase the interfacial area. A device with a large dispersion of interfaces throughout the photoactive layer requires smaller exciton diffusion distances, and thus, a larger exciton dissociation yield is achieved. There exists a trade-

¹⁷⁸ <http://www.sigmaaldrich.com/materials-science/organic-electronics/opv-tutorial.html>

¹⁷⁹ N.S. Sariciftci, L. Smilowitz, A.J. Heeger, F. Wudl, *Science*, 1992, 258, 1474.

¹⁸⁰ C. J. Brabec, S. Gowrisanker, J. J. M. Halls, D. Laird, S. Jia, S. P. Williams, *Adv. Mater*, 2010, 22, 3839.

off between increasing interfacial area via the intimate dispersion of phases and the creation of efficient conductive pathways through which free electrons and holes may be transported. The arrangement of donor and acceptor phase is thus crucial to device performance.

All of the steps in the flow diagram of Figure 3.5 are influenced by a large number of factors such as the optical properties of the semiconductor polymer (i.e. how much of the solar spectrum is absorbed by the conjugated polymer or the mismatch with respect to the light spectrum), the organization of the photoactive material in solid state (or film), the device structure, the type of electrodes, etc. As no material can absorb across the whole solar spectrum, there will always be wasted photons. Therefore, the first prerequisite for an efficient solar cell is to capture a large fraction of the incoming sun light by the conjugated polymer in the active layer. Hence, the semiconducting polymer is expected to have an optimum band-gap to absorb enough photons from the solar spectrum. However, most solution processable semiconducting polymers have band gaps larger than 1.9 eV, meaning that most conjugated polymers absorb in the green or blue regions of the spectrum (i.e. absorption at higher wavelength; in the red or infrared regions is harder to achieve). Additionally, the low charge carrier mobilities in conjugated polymers limit the useful thickness of devices to approximately 100 nm, which in turn leads to the absorption of only about 60 % of the incident light at the absorption maximum. This indicates that performance of an organic PV device is highly dependent on the absorption efficiency of the conjugated semiconductor polymer. To harvest the wasted photons, a number of researches are ongoing through the development of new donor conjugated polymers with tailored energy levels and good processability (such as the “**low band gap**” conjugated polymers).

As such, in this thesis some low band gap alternating copolymers were used as donor materials (see Ch. 2.2.2 and Ch. 7) and fullerene derivative as an acceptor under AM 1.5G irradiation of $100 \text{ mW} \cdot \text{cm}^{-2}$ illumination intensity¹⁸¹.

3.2 Parameters of Device Characterization

A solar cell is characterized on a basic level by the graph of its current as a function of voltage, known as its I-V curve, as Figure 3.7. Any inference taken from those parameters could show the possible mistake be made during the experimental procedure or a new clue/discovery. Except of I-V, there also some other standard parameters that have to be calculated after the experiment as, density of short circuit current (J_{sc}), open circuit voltage (V_{oc}), fill factor (FF), external quantum efficiency (EQE) and of course power conventional efficiency (PCE), which are going to be presented below in detail.

¹⁸¹ <http://www.greenrhinoenergy.com/solar/radiation/spectra.php>

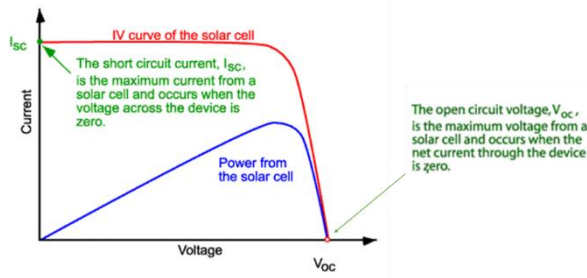


Figure 3.7 A typical I-V curve, where the Short circuit current and Open circuit voltage are shown¹⁸².

3.2.1 Short Circuit Current, I_{sc} /Density of Short Circuit Current, J_{sc}

The short circuit current, the current when the voltage has a zero value, increases with light intensity, as higher intensity means more photons, which in turn means more electrons. Since the short circuit current I_{sc} is roughly proportional to the area of the solar cell, the short circuit current density,

$J_{sc} = I_{sc}/A$, (A = Active Area ($A.A$) = 4mm^2 , in our case), is often used to compare solar cells.

When a load is connected to the solar cell, the current decreases and a voltage develops as charge builds up at the terminals. The resulting current can be viewed as a superposition of the short circuit current, caused by the absorption of photons, and a *dark current*, which is caused by the potential built up over the load and flows in the opposite direction. As a solar cell contains a PN-junction, just as a diode, it may be treated as a diode. For an ideal diode, the dark current density is given by:

$$J_{dark}(V) = J_0 \left[\exp\left(\frac{q*V}{n*K*R}\right) - 1 \right] \quad (1.1)$$

where, J_0 is a constant, q is the electron charge, V is the voltage between the terminals, n is the diode ideality factor, k is the Boltzmann constant and T the temperature.

$$J = J_{sc} - J_0 \left[\exp\left(\frac{q*V}{n*K*R}\right) - 1 \right] \quad (1.2)$$

The resulting current can be approximated as a superposition of the short circuit current and the dark current¹⁸³:

$$I_{dark} = I_L - I_s \left[\exp\left(\frac{V}{nKR}\right) - 1 \right] \quad (1.3)$$

where, I_L is the electric current or the light-generated current and I_s is the saturation current of the diode.

¹⁸² <http://www.pveducation.org/pvcdrom/solar-cell-operation/open-circuit-voltage>

¹⁸³ <http://org.ntnu.no/solarcells/pages/introduction.php>

3.2.2 Open circuit voltage, V_{oc}

The open-circuit voltage, V_{oc} , is the maximum voltage available from a solar cell, and this occurs at zero current. The open-circuit voltage corresponds to the amount of forward bias on the solar cell due to the bias of the solar cell junction with the light-generated current.

To find an expression for the open circuit voltage, V_{oc} , we use (1.2) setting $J = 0$. This means that the two currents cancel out so that no current flows, which exactly is the case in an open circuit¹⁸⁴. The resulting expression is:

$$V_{OC} = \frac{K_B * T}{q} \ln \left(\frac{J_{SC}}{J_0} + 1 \right) \quad (1.4)$$

The built-in electric field separating the photogenerated electrons and holes can at most provide the **built-in potential, V_{bi}** . Hence, the built-in voltage gives the upper bound of the open circuit voltage. The effect of the parasitic series and shunt resistances, R_S and R_{SH} due to its bulk resistivity and presence of defects can included in the **Schockley equation**¹⁸⁵ as:

$$I = I_s \exp \left(\frac{q}{nKT} (V - IR_s) \right) - 1 + \frac{V - IR_s}{R_{SH}} - I_L \quad (1.5)$$

Figure 3.8 shows the equivalent circuit of p-n junction solar cell, in which the I-V curve of this circuit is described by the equation above. The circuit consists of the following three parts. A current source I_L that considers the light-generated current, a diode that accounts for the nonlinear voltage dependence and a shunt as well as a series resistor.

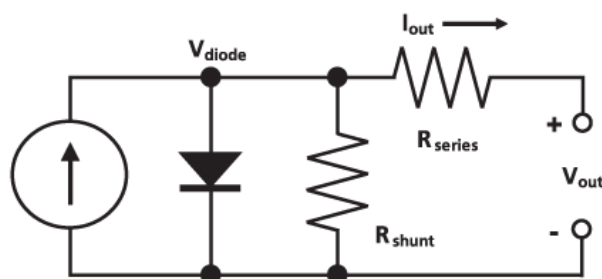


Figure 3.8 Equivalent circuit of a p-n junction solar cell¹⁸⁶.

The current source generates a current I_L up on illumination. I_L can be described as the number of free electron/hole pairs immediately after generation - before any recombination can take place. The series resistance R_S is due to the bulk resistance of the semiconductor material, the bulk resistance of the metallic contacts and the contact resistance between the metallic contacts and the semiconductor. The shunt resistance R_{SH} is caused by leakage across the p-n junction around the edge of the cell and in non-peripheral regions in the presence of defects and precipitates of foreign impurities in the junction region.

¹⁸⁴ <http://org.ntnu.no/solarcells/pages/introduction.php>

¹⁸⁵ <http://www.ni.com/white-paper/7230/en/>

¹⁸⁶ <http://www4.evaluationengineering.com/articles/201005/lights-out-solar-power.php>

In conclusion, in the standard p-n junction solar cell, light absorption occurs via band gap excitation of electrons in the bulk of the semiconductor, charge separation in the internal electric field of the p-n junction and charge collection by transport of electrons and holes through the bulk of the semiconductor to the electrical contacts. As anybody can see from Fig. 3.6, there is another way to find the V_{OC} from the difference of the $LUMO_{ACCEPTOR}$ and $HOMO_{DONOR}$, where then:

$$V_{OC} = \frac{1}{e} * (LUMO_{ACCEPT} - HOMO_{DONOR}) - 0.3^{187} \quad (1.6)$$

Studies have shown that the value of V_{oc} depends largely on the relative energy levels of the donor and acceptor species that form the essential heterojunction.

3.2.3 Fill factor, FF

The short-circuit current and the open-circuit voltage are the maximum current and voltage respectively from a solar cell. However, at both of these operating points, the power from the solar cell is zero. The "fill factor", more commonly known by its abbreviation "FF", is a parameter which, in conjunction with V_{oc} and I_{sc} , determines the maximum power from a solar cell. The FF is defined as the ratio of the maximum power from the solar cell to the product of V_{oc} and I_{sc} . Graphically, the FF is a measure of the "squareness" of the solar cell and is also the area of the largest rectangle which will fit in the I-V curve. Basically, with higher FF, the performance of a solar cell is better. The FF is illustrated below:

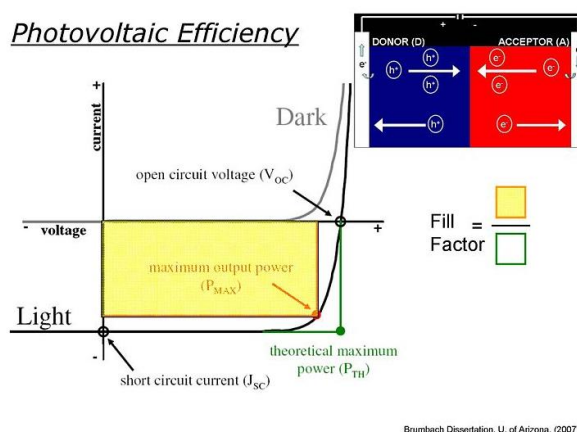


Figure 3.9 I-V curve with the schematic representation and the equation of Fill Factor, FF¹⁸⁸.

¹⁸⁷ **0.3 is an average value for organic materials

¹⁸⁸ http://photonicswiki.org/index.php?title=Physics_of_Solar_Cells

3.2.4 Power conversion efficiency, PCE

The efficiency is one of the three key factors for an efficient OSC device. It is the most commonly used parameter to compare the performance of one solar cell to another. Efficiency is defined as the ratio of energy output from the solar cell to input energy from the sun. In addition to reflecting the performance of the solar cell itself, the efficiency depends on the spectrum and intensity of the incident sunlight and the temperature of the solar cell. Therefore, conditions under which efficiency is measured must be carefully controlled in order to compare the performance of one device to another. Terrestrial solar cells are measured under AM1.5 conditions and at a temperature of 25°C. The efficiency (η) of a solar cell is determined as the fraction of incident power which is converted to electricity and is defined as:

$$\eta = \frac{V_{OC} * I_{SC} * FF}{P_{INC}} * 100\% \quad (1.7)$$

$$P_{MAX} = V_{OC} * I_{SC} * FF \quad (1.8)$$

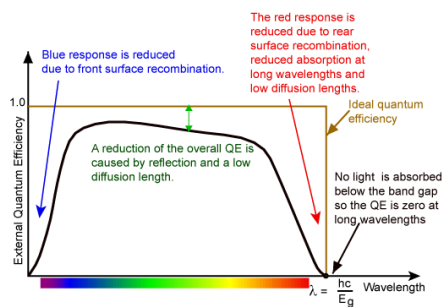
where, P_{INC} is the incident power density (sun power) = 100 mW/cm².

3.2.5 External quantum efficiency, EQE or Incident photon-to-current efficiency, IPCE

IPCE or Quantum Efficiency (QE) is a measure of how efficiently the device converts the incident light into electrical energy at a given wavelength. There are two types of QE: External Quantum Efficiency (EQE) and Internal Quantum Efficiency (IQE).

- **EQE** is the ratio between the number of collected carriers and the number of all the incident photons on the device active area at a given wavelength.
- **IQE** is the ratio between the number of collected carriers and the number of all the absorbed photons by only the active absorber at a given wavelength.

The principle of EQE measurement is based on illuminating the sample by a monochromatic light and recording the device electrical current (number of generated carriers). By varying the frequency of the light the entire curve of the current as a function of wavelength can then be established. Figure 3.6 shows an example of an EQE curve for a typical silicon based solar device. The area under the curve will then represent the total number of carriers created by the device under full spectrum white light illumination. In other words, the integration of the curve will give the electrical current density.



The quantum efficiency of a silicon solar cell. Quantum efficiency is usually not measured much below 350 nm as the power from the AM1.5 contained in such low wavelengths is low.

Figure 3.10 A typical External Quantum Efficiency curve of a silicon based solar device¹⁸⁹.

In order to determine IQE the light absorbed by the active layer stack has to be identified. This is typically done by recording and excluding the light reflected from the device and using only the absorbed

portion of light for the calculation of quantum efficiency. Since the absorbed light is typically less than the total incident light (as there will always be some loss of light due to reflections) then EQE will typically be less than IQE. The difference between IQE and EQE is important for distinguishing loss mechanisms between optical absorption properties of the entire device and photo-conversion properties of the absorbing materials. IPCE is also useful for studying degradation properties of devices. The general reduction in the IPCE during time points to deterioration of photo-conversion properties of the active material, while the change of the shape of the IPCE curve may point to morphological alterations in the absorbing layer.

¹⁸⁹ <http://plasticphotovoltaics.org/lc/characterization/lc-advanced-c/lc-ipce.html>

Chapter 4: Introduction to 2D Materials

“The initial studies on 2D materials are focusing a lot on their electronic properties, because these are close to physicists’ hearts,” says Kinaret. “But I think that the applications, if and when they come, are likely to be in a completely unpredicted area.”¹⁹⁰

2D Materials, sometimes referred to as *Single layer materials*, are crystalline materials consisting of a single layer of atoms. They are substances with a thickness of a few nanometers or less. Electrons in these materials are free to move (as usually happens to crystalline semiconducting materials) in the two-dimensional plane, but their restricted motion in the third direction is governed by quantum mechanics. Prominent examples include quantum wells and graphene, which Andre Geim and Konstantin Novoselov found in 2004 when they first reported isolating graphene¹⁹¹ in their laboratory at the University of Manchester, UK.

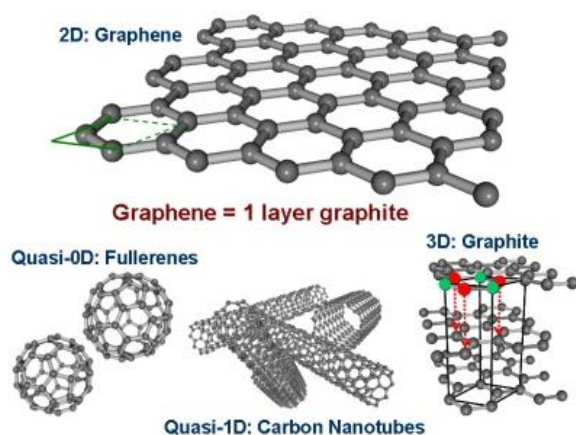


Figure 4.1 Honeycomb lattice of graphene. Graphene layers can be stacked into graphite or rolled up into carbon nanotubes. The formation of fullerenes requires the incorporation of five-membered rings¹⁹².

4.1 Graphite-Graphite Oxide-Graphene Oxide-Reduced Graphene Oxide

When Lavoisier listed “Carbone” in his “Traite’ Ele’mentaire de Chimie” as one of the newly identified chemical elements, for the first time just 220 years ago, he had already identified the versatility of carbon since he had shown that it was the elementary component of both diamond and graphite.¹⁹³ Since then, more allotropes of carbon have been reported and a large scientific community has been passionate about deciphering the properties of this element that can adopt many structures^{194,195} ranging from diamond and graphite (3D) to graphene (2D), nanotubes (1D) or fullerenes (0D) as illustrated in Fig. 4.1.

Study of carbon nanostructures is very extensive due to their unmatched properties and numerous applications. Among the various species of carbon, graphene is one of the most talked about in the present era due to its remarkably excellent properties¹⁹⁶. It has been paid

¹⁹⁰ G. R. Bhimanapati et al., ACS Nano, 2015, 9, 12, 11509.

¹⁹¹ K. S. Novoselov et al., Science, 2004, 306, 666.

¹⁹² <http://www.graphene.nat.uni-erlangen.de/grapheneng.htm>

¹⁹³ A. Lavoisier, *Traite’ ele’mentaire de chimie, presente’ dans un ordre nouveau et d’apre’s les decouvertes modernes*, 2, 1789.

¹⁹⁴ L.-C. Xu et al., Nanoscale, 2014, 6, 1113.

¹⁹⁵ H. Lu, S.-D. Li, J. Mater. Chem. C, 2013, 1, 3677

¹⁹⁶ X. Lin, J. Jia, N. Yousefi, X. Shen, J.-K. Kim, J. Mater. Chem. C, 2013, 1, 6869.

much attention since its first appearance in 2004 when Geim et al. obtained one atomic layer thickness graphene from graphite by peeling with adhesive tape.²⁰⁴ (Fig. 4.2) Their groundbreaking experiments on graphene were honored with the Nobel Prize in Physics in 2010.^{197,198,199}

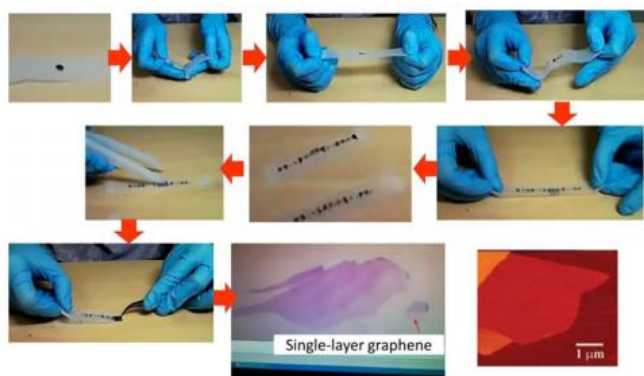


Figure 4.2 Schematic representation of the Graphene mechanical exfoliation process and a Microscope image of Graphene flake.

Graphene presents great potential applications in various fields, including electrodes,²⁰⁰ supercapacitors,²⁰¹ composite materials²⁰² and sensors²⁰³. As well,

it has excellent electronic, mechanical and thermal properties as, a specific surface area of 2620 m²/g, a Young's modulus of 1 TPa and intrinsic strength of 130 GPa. It has a very high electronic conductivity at room temperature, and its electron mobility is 2.5 × 10⁵ cm²/V*s. Its thermal conductivity is around 3000 Wm/K. Graphene has a unique two-dimensional structure consisting of a single atomic layer of sp² hybridized carbon atoms. The identification of graphene among mechanically exfoliated graphite sheets and the subsequent discovery of its unusual electronic properties have led to an extraordinary amount of interest from both academia and industry²⁰⁴. Because of its remarkable properties^{205,206} applications using graphene in a wide range of areas, including high-speed electronic²⁰⁷ and optical devices²⁰⁸, energy generation and storage²⁰⁹, hybrid materials²¹⁰, chemical sensors²¹¹, and even DNA sequencing²¹², have all been explored. A variety of proof-of-concept devices have also been demonstrated²¹³. However, pristine graphene itself is unlikely to be used for the fabrication of logical circuits operated at room temperature with low standby power dissipation because graphene has no band gap (E_g).!! The result is a small current on/off ratio in graphene field-effect transistors (FETs)²¹⁴. The prerequisite for such applications is the mass production of

¹⁹⁷ K. S. Novoselov, A. K. Geim, S. V. Morozov, D. Jiang, M. I. Katsnelson, I. V. Grigorieva, S. V. Dubonos, A. A. Firsov, *Nature*, 2005, 438, 197.

¹⁹⁸ K. S. Novoselov, D. Jiang, F. Schedin, T. J. Booth, V. V. Khotkevich, S. V. Morozov, A. K. Geim, *Proc. Natl. Acad. Sci. USA*, 2005, 102, 10451.

¹⁹⁹ A. K. Geim, *Angew. Chem.*, 2011, 123, 7100.

²⁰⁰ Y. Gao, W. Shi, W. Wang, Y. Leng, *Ind Eng Chem Res.*, 2014, 53, 43, 16777.

²⁰¹ Y. Shao et al., *Chem Soc Rev.*, 2015, 44, 11, 3639

²⁰² X. Yang, L. Li, S. Shang, X.-M. Tao, *Polymer*, 2010, 51, 15, 3431.

²⁰³ X. Zhou, Y. Wei, Q. He, F. Boey, Q. Zhang, H. Zhang, *Chem. Commun.*, 2010, 46, 37, 6974.

²⁰⁵ A. Geim, *Nat. Mater.* 2007, 6, 183.

²⁰⁶ K. S. Novoselov, V. I. Fal'ko, L. Colombo, P. R. Gellert, M. G. Schwab, K. Kim, *Nature*, 2012, 490, 192.

²⁰⁷ Y. M. Lin, C. Dimitrakopoulos, K. A. Jenkins, D. B. Farmer, H. Y. Chiu, A. Grill, P. Avouris, *Science* 2010, 327, 662.

²⁰⁸ M. Liu, X. B. Yin, E. Ulin-Avila, B. S. Geng, T. Zentgraf, L. Lu, F. Wang, X. Zhang, *Nature*, 2011, 474, 64.

²⁰⁹ K. S. Kim, Y. Zhao, H. Jang, S. Y. Lee, J. M. Kim, K. S. Kim, J. Y. Ahn, P. Kim, J. Y. Choi, B. H. Hong, *Nature*, 2009, 457, 706.

²¹⁰ X. Yang, M. S. Xu, W. M. Qiu, X. Q. Chen, M. Deng, J. L. Zhang, H. Iwai, E. Watanabe, H. Z. Chen, *J. Mater. Chem.* 2011, 21, 8096

²¹¹ M. Deng, X. Yang, M. Silke, W. M. Qiu, M. S. Xu, G. Borghs, H. Z. Chen, *Sens. Actuat. B: Chem.*, 2011, 158, 176

²¹² S. Garaj, W. Hubbard, A. Reina, J. Kong, D. Branton, J. A. Golovchenko, *Nature*, 2010, 467, 190

²¹³ M. H. Rummeli et al., *Adv. Mater.*, 2011, 23, 4471.

²¹⁴ K. Kim, J. Y. Choi, T. Kim, S. H. Cho, H. J. Chung, *Nature*, 2011, 479, 338.

graphene in a controlled manner because the number of graphene layers as well as the defects in these graphene layers significantly influence the subsequent transport properties.

There are several methods to obtain graphene, except mechanical exfoliation, as epitaxial growth,²¹⁵ liquid-phase exfoliation of graphite,²¹⁶ chemical vapor deposition,²¹⁷ as well as chemical reduction of **Graphene oxide (GO)**²¹⁸. Single-layer transferable graphene nanosheets were first obtained by mechanical exfoliation (**Scotch-tape method**) of bulk graphite and by epitaxial chemical vapor deposition²¹⁹, yet they are not suitable for the bulk production of graphene and not used for its large scale manufacturing. Among all these processes, chemical reduction of GO has been regarded as the fastest way to produce graphene in large quantities, and it also has an advantage of solution processable²²⁰.

Also another important factor is scalability, for the synthesis of graphene, and one of the most popular approaches towards graphite exfoliation is the use of strong oxidizing agents to obtain GO, a nonconductive hydrophilic carbon material^{221,222}. Chemical means are a practical approach for the bulk scale synthesis of graphene²²³. Although the exact structure of GO is difficult to determine, it is clear that for GO the previously contiguous aromatic lattice of graphene is interrupted by epoxides, alcohols, ketones, and carboxylic groups.

GO can be readily synthesized by the oxidation of the natural flake graphite (NFG) powder as the first step. GO is of great interest due to its low cost, easy access, and widespread ability to convert to graphene. The most common source of graphite is the flake graphite. Flake graphite is a naturally occurring mineral that is purified by removing the heteroatomic contamination. **Brodie** first demonstrated the synthesis of GO in 1859 by adding a portion of potassium chlorate to a slurry of graphite in fuming nitric acid²²⁴. In 1898, **Staudenmaier** improved on this protocol by using a mixture of concentrated sulfuric acid and fuming nitric acid followed by gradual addition of chlorate to the reaction mixture. This small change in the procedure provided a simple and revised protocol for the production of highly oxidized GO²²⁵. In 1958, **Hummers** reported an alternative method for the synthesis of graphene oxide by using KMnO_4 and NaNO_3

²¹⁵ P. Sutter, *Nat. Mater.*, 2009, 8, 171.

²¹⁶ Y. Hernandez, V. Nicolosi, M. Lotya, F. M. Blighe, Z. Sun, S. De, *Nat Nanotechnol.*, 2008, 3, 9, 563.

²¹⁷ A. Ismach, C. Druzgalski, S. Penwell, A. Schwartzberg, M. Zheng, A. Javey, *Nano Lett.*, 2010, 10, 5, 1542.

²¹⁸ P. Liu, Y. Huang, L. Wang, *Mater Lett.*, 2013, 91, 125.

²¹⁹ C. Berger, Z. Song, X. Li, X. Wu, N. Brown, C. Naud, D. Mayou, T. Li, J. Hass, A. N. Marchenkov, E. H. Conrad, P. N. First, W. A. De Heer, *Science*, 2006, 312, 1191.

²²⁰ Y. Wang, Z. Shi, J. Yin, *Appl. Mater. Interfaces*, 2011, 3, 4, 1127.

²²¹ A. L. Higginbotham, J. R. Lomeda, A. B. Morgan, J. M. Tour, *Appl. Mater. Interf.*, 2009, 1, 2256.

²²² A. Lerf, H. He, M. Forster, J. Klinowski, *Journal of Physical Chemistry B*, 1998, 102, 4477.

²²³ R. Ruoff, *Nat. Nanotechnol.*, 2008, 3, 10.

²²⁴ B. C. Brodie, *Philosophical Transactions of the Royal Society of London*, 1859, 149, 249.

²²⁵ L. Staudenmaier, *Berichte der Deutschen Chemischen Gesellschaft*, 1898, 31, 1481.

in concentrated H_2SO_4 ²²⁶. RGO prepared by this method could be used for preparing large graphitic films²²⁷ (Fig. 4.3).

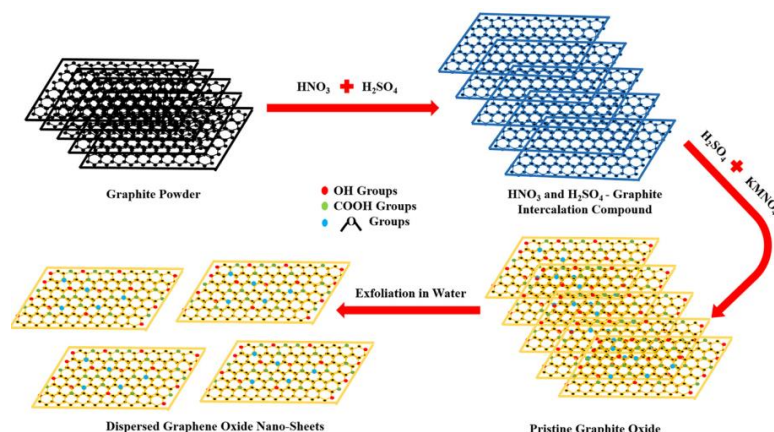


Figure 4.3 Preparation of chemically converted graphene (CCG) by reduction of GO²²⁸

Specifically RGO fabrication technique involves three steps^{229,230}. First, graphite oxide is obtained by oxidation of graphite powder using the Brodie

or Staudenmaier or Hummer's method²³¹ to produce **Graphite oxide (GrO)**. Second, GrO is exfoliated to GO by ultrasonication and third various reductants were used to obtain **Reduced Graphene oxide (RGO)**. Hydrazine (N_2H_4)²³², sodium borohydride (NaBH_4) and its derivatives²²⁹, oxalic acid ($\text{C}_2\text{H}_2\text{O}_4$)²³³, sodium hydrosulfite ($\text{Na}_2\text{S}_2\text{O}_4$)²³⁴, as well as Hydrohalic acids (**HI**, **HBr**, **HCL**)²³⁵ have been reported as reductants to remove oxygen-containing functional groups of GO and thus to restore the conjugate structure of graphene. In the present work, oxidation of Graphite has been done using the modified Hummers method (production of GrO) and thereafter GrO has been reduced using various reductants to obtain RGO. Specifically for RGO production, hydroiodic acid (HI) was used as the major reductant. Then the mixture was stored at 40 °C for 40 hours with constant stirring. Next, the product was isolated by filtration, washed with saturated sodium bicarbonate (NaHCO_3), distilled water and acetone, and then vacuum dried overnight at room temperature to yield $\text{RG-O}_{\text{HI-Ac-OH}}$.

Still, Geim's and Novoselov's success in making graphene spurred many to start investigating alternative 2D materials that could have band gaps, also due to their unusual characteristics and for use in applications such as photovoltaics, semiconductors, electrodes and water purification. Unlike graphene, for example, many TMDCs are semiconductors, meaning that they have the potential to be made into molecular-scale digital processors that are much more energy efficient than anything possible with silicon. Ironically, one of the most exciting frontiers in 2D materials is stacking them into 3D devices. Furthermore, 2D materials can generally be categorized as either 2D allotropes of various elements or compounds (usually consisting of two covalently bonding elements). The elemental 2D materials generally carry the -ene suffix in their names while the compounds have -ane or -ide suffixes. Layered combinations of different 2D materials are generally called van der Waals heterostructures. It has been speculated that there may be around 500 (!) 2D materials yet to be found²³⁶.

²²⁶ W. S. Hummers, R. E. Offeman, J. Am. Chem. Soc, 1958, 80, 1339.

²²⁷ T. Ishikawa, T. Nagaoki, New Carbon Industry (2nd Edition), 1986, 125.

²²⁸ H. M. Hegab, L. Zou, J. Membr. Sci., 2015, 484, 15, 95.

²²⁹ S. Stankovich et al., Carbon, 2007, 45, 1558.

²³⁰ I. K. Moon, J. Lee, R. S. Ruoff, H. Lee, Nat. Comm., 2010, 1, 73.

²³¹ G. Wang et al., J. Phys. Chem. C, 2008, 112, 8192.

²³² J. Chen et al., Carbon, 2013, 64, 225.

²³³ H. L. Guo, X. F. Wang, Q. Y. Qian, F. Wang, X. H. Xia, ACS Nano, 2009, 3, 2653.

²³⁴ A. Malas, C. K. Das, A. Das, G. Heinrich, Mater. Design, 2012, 39, 410.

²³⁵ C. K. Chuaa, M. Pumera, Chem. Soc. Rev., 2014, 43, 291.

²³⁶ "The super materials that could trump graphene", Nature, 17, 2015.

The **ideal material** would be a material that does not conduct electricity unless its electrons are boosted with a certain amount of energy from heat, light or an external voltage. The amount of energy needed varies with the material, and is known as the band gap (E_g).

4.2 Two-Dimensional (2D) Transition Metal Dichalcogenides (TMDs)

The application of graphene in semiconducting devices is hindered by its lack of a bandgap, therefore there was a high demand of graphene-like materials but with the effort of a band gap. This special part of this thesis is about two-dimensional transition metal dichalcogenides (2D TMDs), which category was established as a solution for the aforementioned issue. The family of 2D materials consisting of over 40 compounds with the generalized formula of MX_2 , where M is a transition metal typically from groups IV–VII, and X is a chalcogenide such as S, Se or Te (Fig. 4.4).

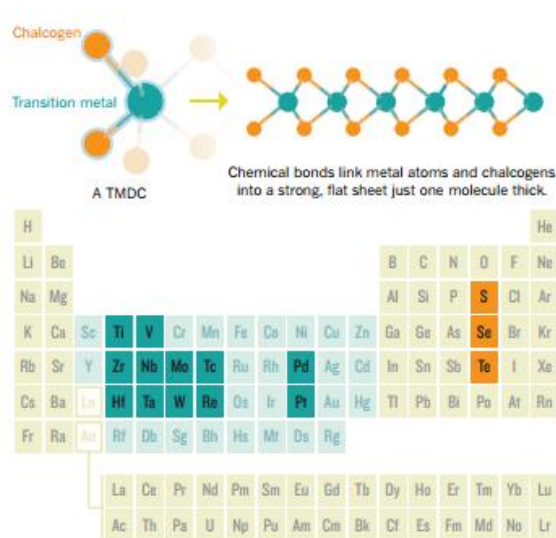


Figure 4.4 Typical structure of a TMD material²³⁷.

Like graphene and other van der Waals solids, TMDs are characterized by weak, noncovalent bonding between layers and strong in-plane covalent bonding. Therefore, bulk TMDs can be exfoliated into single- or few-layered structures by physical or chemical means, such as adhesive tape exfoliation,²³⁸ solvent assisted exfoliation,²³⁹ and chemical exfoliation via lithium intercalation.^{240,241}

Each individual layer of the TMDs consists of three atomic layers in which the transition metal is sandwiched by two chalcogens. Furthermore, the chalcogen atoms are saturated and therefore are not highly reactive. These features allow for the attainment of individual layers of the TMDs by several exfoliation, isolation of single layers via mechanical^{242,243} or chemical exfoliation²⁴⁴ or vapor deposition methods, specifically. The isolation of monolayers of TMDs leads to the dramatic changes in their properties, primarily due to the quantum confinement²⁴⁵ of charge carriers in two dimensions (x- and y-directions) due to the absence of interactions in the z-direction. Thus, single layered NS are two-dimensional materials that possess dramatically different fundamental properties compared to their bulk counterparts, making them

²³⁷ H. Terrones et al. *Sci. Rep.* 2013, 3, 1549.

²³⁸ X. Chen, A. R. McDonald, *Adv. Mater.*, 2016, 28, 5738.

²³⁹ F. Jiang et al., *J. Mater. Chem. A*, 2016, 4, 5265.

²⁴⁰ L. Yuwen et al., *Chem. Commun.*, 2016, 52, 529.

²⁴¹ Y. Jung, Y. Zhou, J. J. Cha, *Inorg. Chem. Front.*, 2016, 3, 452.

²⁴² H. Li, J. Wu, Z. Yin, H. Zhang, *Acc. Chem. Res.*, 2014, 47, 4, 1067.

²⁴³ J. Kang, S. Tongay, J. Zhou, J. Li, J. Wu, *Appl. Phys. Lett.*, 2013.

²⁴⁴ M. Chhowalla, H. S. Shin, G. Eda, L.-J. Li, K. P. Loh, H. Zhang, *Natur. Chem.*, 2013, 5, 263.

²⁴⁵ A. Kuc, N. Zibouche, T. Heine, *Phys. Rev. B*, 2011, 83, 24.

potentially interesting for wide-ranging applications such as catalysis, electronics and photonics. This has generated a tremendous amount of interest in these promising materials.

In contrast to graphene or silicon where the electronic properties are based on hybridization of s and p orbitals, the electronic structure of TMDs depends on the filling of d orbitals of the transition metals. Transition metals in MX_2 compounds have an oxidation state of +4 and the chalcogens have an oxidation state of -2. Thus the number of d orbital electrons varies between 0 and 6 for group 4 to group 10 TMDs, respectively.²⁴⁶ In addition to diverse electronic properties that can be achieved by choosing the appropriate combinations of the M and X elements, different phases in single layer TMDs can also be realized. A single layer of TMDs can have a trigonal prismatic phase or an octahedral phase. The trigonal prismatic phase is also referred to as the 2H phase (or 1H in the case of a single layer) and can be described by a hexagonal symmetry (the D_{3h} group) and corresponds to a trigonal prismatic coordination of the metal atoms. The octahedral phase has a tetragonal symmetry (D_{3d}) and corresponds to an octahedral coordination of the metal atoms.

The filling of the d orbitals of the metal directly influences the atomic structure of the TMD layers.²⁴⁶ Since the p-orbitals of chalcogens have been located at much lower energy than the Fermi level, only the filling of the d orbitals determines the nature of phases in MX_2 compounds. Completely filled orbitals give rise to semiconducting behavior while partial filling induces metallic behavior. The type of symmetry of the single layer also strongly depends on the filling of d orbitals. The group 4 (d^0) TMDs and most of the group 6 (d^2) TMDs have trigonal prismatic phases. Group 5 (d^1) TMDs can have both trigonal prismatic or octahedral phases whereas group 7 TMDs have a typically distorted octahedral structure (Fig. 4.5) Group 10 TMDs (d^6) have an octahedral phase.

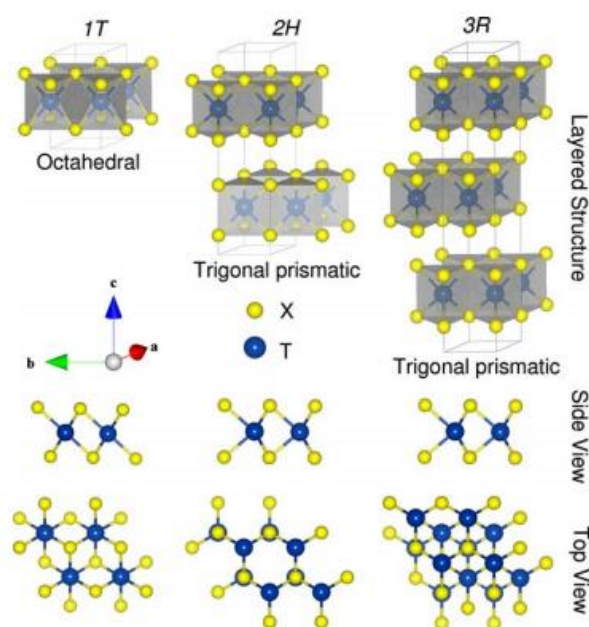


Figure 4.5 Structural representation of 1T, 2H and 3R TMC polytypes and their corresponding metal atoms coordination. The side and top views of layered forms are shown.²⁴⁷

The phase of single-layer TMDs depends strongly on the d orbital electron density of the transition metal. Tuning the filling of the d orbital enables phase engineering in TMDs. Several examples of phase modification via chemical reactions have been reported for group 6 TMDs

such as MoS_2 , MoSe_2 and WS_2 .^{248,249} Early experiments from Py et al. demonstrated the

²⁴⁶ D. Voiry, A. Mohite, M. Chhowalla, Chem. Soc. Rev., 2015, 44, 2702.

²⁴⁷ A. Kuc, Chemical Modelling, 2014, 11, 11, 1.

²⁴⁸ B. K. Miremadi, S. R. Morrison, J. Appl. Phys., 1988, 63, 4970.

²⁴⁹ R. A. Gordon, D. Yang, E. D. Crozier, D. T. Jiang, R. F. Frindt, Phys. Rev. B, 2002, 65, 125407.

formation of the metallic 1T phase of MoS₂ upon lithium intercalation,²⁵⁰ which induces reduction of MoS₂ and increases the electron density in the d orbital. As a consequence, group 6 TMDs with the 1T phase are typically negatively charged.²⁵¹ Several groups have predicted^{252,253} and verified^{254,255} the transition from an indirect band gap at the Γ -point to a direct band gap at the K-point of the Brillouin zone as the semiconducting TMDC thickness is reduced to a single layer. Besides the transformation to a direct band gap for a monolayer of STMD, a break of inversion symmetry also occurs,²⁵⁶ which has been confirmed experimentally by circularly polarized light experiments that lead to valley polarization effects.^{257,258}

In particular, bulk WS₂ has an indirect band gap of 0.88 eV, whereas single layer WS₂ has a direct band gap of 1.94 eV (see Fig. 4.6), that results in enhanced photoluminescence (PL) by up to 4 orders of magnitude²⁵⁹. Similar evidence for a direct band gap transition has also been reported for single layer MoSe₂, WS₂, and WSe₂.^{260,261}

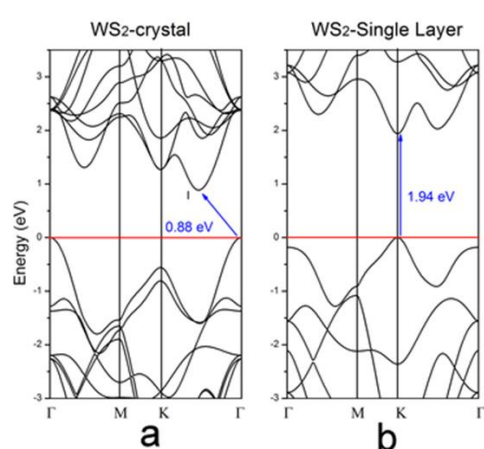


Figure 4.6 a) Band structure of bulk hexagonal WS₂ (The blue arrow shows the indirect gap Γ -I); (b) Band structure of a monolayer of WS₂ (note the blue arrow revealing the direct band gap location)²⁶².

By 2010, Kis's team had built its first single-layer transistor²⁶³ from the TMDC MoS₂, speculating that such devices could one day offer flexible electronics (like flexible OSCs) whose small component size and low voltage requirements would mean that they consumed much less power than conventional silicon transistors. Being

semiconducting was not their only advantage. Studies in 2010 showed that MoS₂ could both absorb and emit light²⁶⁴ efficiently, making it — and probably other TMDCs (Tungsten Disulfide, WS₂ and Tungsten Diselenide, WSe₂)— attractive for use in solar cells and photodetectors. “A single layer of TMDCs can capture more than 10% of incoming photons, an incredible figure for a material three atoms thick”, says Bernhard Urbaszek, a physicist at the Physics and Chemistry of NanoObjects Laboratory in Toulouse, France. This also helps them in another task: converting light into electricity. Specifically, when an incoming photon hits the three-layer crystal, it boosts an electron pass the E_g, allowing it to move through an external circuit. Each

²⁵⁰ M. A. Py, R. R. Haering, *Can. J. Phys.*, 1983, 61, 76.

²⁵¹ J. Heising, M. G. Kanatzidis, *J. Am. Chem. Soc.*, 1999, 121, 11720.

²⁵² A. Kuc, N. Zibouche, T. Heine, *Phys. Rev. B*, 2011, 83, 245213.

²⁵³ J. K. Ellis, M. J. Lucero, G. E. Scuseria, *Appl. Phys. Lett.*, 2011, 99, 261908.

²⁵⁴ G. Eda, H. Yamaguchi, D. Voiry, T. Fujita, M. Chen, M. Chhowalla, *Nano Lett.*, 2011, 11, 5111.

²⁵⁵ A. Splendiani, L. Sun, Y. Zhang, T. Li, J. Kim, C.-Y. Chim, G. Galli, F. Wang, *Nano Lett.*, 2010, 10, 1271.

²⁵⁶ D. Xiao, G. B. Liu, W. X. Feng, X. D. Xu, W. Yao, *Phys. Rev. Lett.*, 2012, 108.

²⁵⁷ H. L. Zeng, J. F. Dai, W. Yao, D. Xiao, X. D. Cui, *Nat. Nano.*, 2012, 7, 490.

²⁵⁸ C. Tan et al., *Chem. Rev.*, 2017, 117, 9, 6225.

²⁵⁹ K.F. Mak, C. Lee, J. Hone, J. Shan, T.F. Heinz.

²⁶⁰ S. Tongay, J. Zhou, C. Ataca, K. Lo, T. S. Matthews, J. Li, J. C. Grossman, J. Wu, *Nano Lett.*, 2012, 12, 5576.

²⁶¹ W. Zhao, Z. Ghorannevis, L. Chu, M. Toh, C. Kloc, P.-H. Tan, G. Eda, *ACS Nano*, 2012, 7, 791.

²⁶² H. Terrones, F. Lopez-Urriás & M. Terrones, *Sci. Rep.*, 2013, 3, 1549.

²⁶³ B. Radisavljevic, A. Radenovic, J. Brivio, V. Giacometti, A. Kis A., *Nature Nanotechnol.*, 2011, 6, 147.

²⁶⁴ R. S. Sundaram, M. Engel, A. Lombardo, R. Krupke, A. C. Ferrari, P. Avouris, M. Steiner, *Nano Lett.* 2013, 13, 1416.

free electron leaves behind a kind of empty space in the crystal — a positively charged ‘hole’ where an electron ought to be. Apply a voltage, and these holes and electrons circulate in opposite directions to produce a net flow of electric current. This ability to convert light to electricity and vice versa makes TMDCs promising candidates for applications that involve transmitting information using light.

4.2.1 Tungsten Diselenide, WSe₂

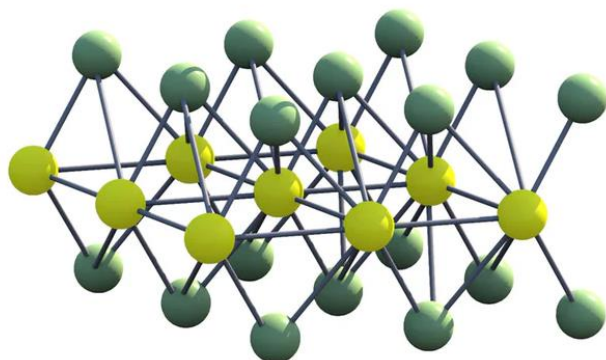


Figure 4.7 Depiction of WSe₂ Crystal Structure.²⁶⁵

Tungsten diselenide (WSe₂) has a hexagonal structure consisting of single sandwiched Se and W layers with thickness of about 3.3 Å. WSe₂ is a semiconductor with a band gap in the range of 1.2 eV - 2eV (Fig. 4.8), depending on how the nonstoichiometry differs from the

ideal W:Se ratio of 1:2, WSe₂ is a black or gray odorless material, has good thermal stability and a high melting point.

Figure 4.8 The exciton binding energy vs. band gap energy for different monolayer TMDs.²⁶⁶

Because of its high optical absorption in the visible range (Fig. 4.9), the layered arrangement between the cations, the high resistance against photocorrosion, and the magnitude of its band gap, WSe₂ is an important material in photoelectrochemical energy conversion devices such as photovoltaic solar cells. WSe₂ also play an important role in a number of technologies such as high temperature solid lubricants and rechargeable batteries. Very recently ultra-low thermal conductivity has been reported in disordered, layered WSe₂ crystals.²⁶⁷

²⁶⁵ <http://newatlas.com/tungsten-diselenide-solar-cells/31161/>

²⁶⁶ H.-L. Liu, C.-C. Shen, S.-H. Su, C.-L. Hsu, M.-Y. Li, L.-J. Li, *Appl. Phys. Lett.*, 2014, 105, 201905.

²⁶⁷ C. A. Patel Kaushik Patel, *Properties of Tungsten Diselenide Single Crystals*, 2014.

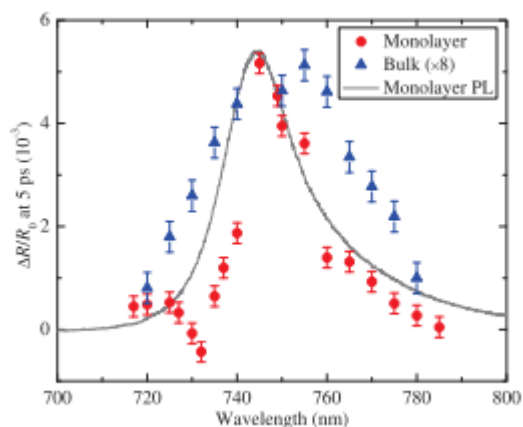


Figure 4.9 Differential reflection signals as a function of the probe wavelength measured in the monolayer (red circles) and bulk (blue triangles, multiplied by 8) WSe₂ samples.²⁶⁸

T. Mueller, from the Vienna University of Technology, had stated that “electronic states in graphene are not very practical for creating photovoltaics”. That’s why he and his coworkers went looking elsewhere and sandwiched a layer of tungsten atoms

between two layers of selenium atoms.²⁶⁹ The resulting tungsten diselenide (WSe₂) monolayer was found to absorb light, similar to graphene, but was also able to use the light to generate electrical power. The tungsten diselenide material is so thin that 95 percent of light hitting it passes straight through, with a tenth of the remaining five percent that is absorbed by the material converted into electrical power. Although this is a small amount overall, the researchers point out that this equates to a quite high internal conversion efficiency and that greater amounts of electricity can be generated by stacking multiple layers on top of each other.

However, the high transparency of the material can also be seen as a benefit, with the potential for solar cell layers to be placed on windows to generate electricity while letting light into the building. The material is also flexible, opening up the potential for it to be used in flexible solar cells and displays.

²⁶⁸ Q. Cui, F. Ceballos, N. Kumar, H. Zhao, *ACS Nano*, 2014, 8, 3, 2970

²⁶⁹ A. Pospischil, M. M. Furchi, T. Mueller, *Nat. Nanotechnol.*, 2014, 9, 257.

Chapter 5: Ternary Organic Solar Cells

As organic semiconducting materials typically exhibit low charge carrier mobility, the active layer, that is, the BHJ blend of the donor material and the acceptor material, is usually very thin (~100 nm) to achieve efficient charge collection. Such a thin film, unfortunately, leads to limited absorption, especially in the wavelength region away from the absorption peaks. To address this issue with binary PSCs (that is, those consisting of one donor material and one acceptor material), tandem PSCs consisting of multiple active layers with complementary absorptions have been introduced (Fig. 5.1, Fig. 1.11, Ch. 1.2.3). It has been shown that light harvest and conversion can indeed be improved with a tandem structure (Fig. 5.1), but the fabrication cost of such tandem PSCs is also significantly increased due to the complexity of these devices, so an elegant alternative would be something close to that but with lower cost, named Ternary structure (Fig. 5.1).

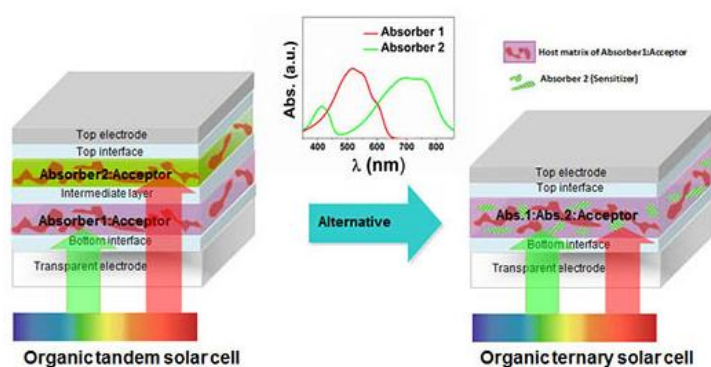


Figure 5.1 The alternative of an expensive Tandem expensive structure, the Ternary structure.²⁷⁰

An effective, yet simple way, to enhance light harvesting and conversion is to use a ternary structure that combines the simplicity of binary PSCs with complementary absorption

from tandem PSCs (Fig. 5.2a, Ch. 1.2.3). A typical ternary blend PSC could offer the aforementioned obligations. Structurally, it contains one additional electron donor or acceptor material compared with its traditional binary counterpart, where this third component is often chosen to have complementary absorption with respect to that of the reference device. As a result, light absorption can be extended to the near infrared (IR) region for wide or medium-bandgap polymers, whereas for low-bandgap polymers the absorption strength for shorter wavelengths could be improved by carefully selecting the third component²⁷¹.

²⁷⁰ <https://www.elitenetzwerk.bayern.de/elite-network-home/forschungsarbeiten/naturwissenschaften/2014/khoram-organic-solar-cells/?L=2>

²⁷¹ L. Lu, T. Xu, W. Chen, E. S. Landry, L. Yu, Nat. Photon., 2014, 8, 716.

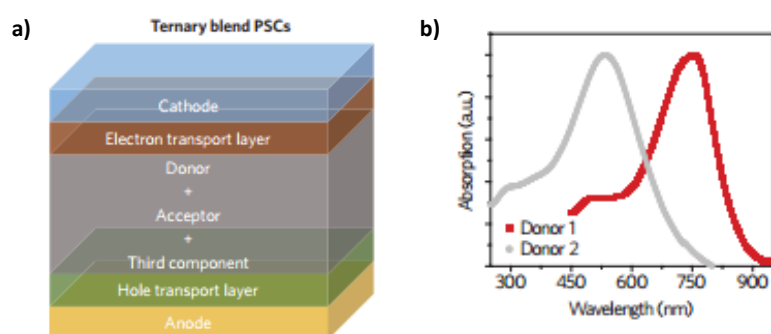


Figure 5.2 (a) Structure of ternary blend bulk heterojunction PSCs with (b) a complementary absorption spectra of the donor and the third component (2nd donor).²⁷²

The charge transfer and transport is governed by various mechanisms,

depending on the sensitizer content, electronic energy levels and bandgap of the three components, sensitizer location in the binary photoactive layer as well as final microstructure of the film. Furthermore, relatively narrow spectral overlap of organic polymer absorption bands within the solar spectrum is one of the major limitations of organic solar cells (Fig. 5.2b).

In general, there are two cases that the third component enhances the PCE of OPV solar cells: through electronic and/or structural (morphological) effects. Electronically, the third component can act as an **energy transfer agent (antenna)** and/or a **charge relay component**. Structurally, it can play the role of a template to facilitate supramolecular assembly in the blend film (preferred for achieving the ideal BHJ morphology) to favour charge dissociation and transport. For effective donor or acceptor sensitization, the third component also needs to be in the appropriate phase (in this case solution processed).

In the cases where the **charge transfer** mechanism dominates (Fig. 5.3a), the third component needs to be located at the interface of the host donor and the acceptor for efficient charge transfer (Fig. 5.3c), this is called an energy level “Cascade” phenomenon of the different materials inside the active layer. Careful design of the third component and judicious selection of its energy levels (for example, in a cascade) are required to ensure efficient charge transfer between the components. As all holes will likely transfer to the donor with a higher HOMO energy level before extraction, the V_{oc} of such systems is pinned by the HOMO level of the two-donor materials.²⁷³ However, when the energy gap of the third component (for example, a second electron donor) is larger than the corresponding components in the binary system, the third component can act as a sensitizer to extend the absorption range.

In **energy transfer** dominated cases, the excited sensitizer transfers energy to either the donor or the acceptor through the **Dexter or Förster resonance energy transfer (FRET)** mechanism^{274,275} (Fig. 5.3b). Therefore, a critical requirement emerges: the emission of the sensitizer and absorption of the donor or acceptor must overlap so as to allow for efficient energy transfer (and vice versa).

Both charge transfer and energy transfer can lead to increases in the short-circuit current density (J_{sc}) by extended absorption and more efficient charge generation. In reality, these two mechanisms are often intertwined, and it is not uncommon that both energy transfer and charge relay processes occur in the same ternary system. Careful photoluminescence (PL) or

²⁷² L. Lu, M. A. Kelly, W. You, L. Yu, *Nat. Photon.*, 2015, 9, 491.

²⁷³ T. Ameri, et al., *Adv. Energy Mater.* 2012, 2, 1198.

²⁷⁴ I. L. Medintz, N. Hildebrandt, *FRET - Förster Resonance Energy Transfer: From Theory to Applications*, 2013.

²⁷⁵ V. Gupta, V. Bharti, M. Kumar, S. Chand, A. J. Heeger, *Adv. Mater.*, 2015, 27, 4398.

transient absorption spectroscopy experiments can help to differentiate these processes. For example, Lu et al. demonstrated that when the energy levels of two donor polymers aligned in a cascade, the PL of the third component with low energy levels (both HOMO and LUMO) was quenched.

In addition, the solar cells made with the **two-donor polymers** (without fullerene as an acceptor) also exhibited photovoltaic performance. Although the emission of the third component matches well with the absorption of the primary donor polymer, these results suggest a charge transfer mechanism operating in this ternary PSC. The third mechanism in ternary blends is still a little be controversial. It is marked by a V_{oc} that scales with the composition of the blend, rather than being pinned by the HOMO level of the donors or the LUMO level of the acceptors. Because of this, it was first suggested that this blend behaved in a manner similar to a parallel-linked tandem cell: the complimentary donors absorb light, split excitons and transport holes²⁷⁶ (Fig. 5.3c). This would imply that each donor forms its own independent transport network (Fig. 5.3c).

However, it has also been suggested that such systems are better explained by an **organic alloy model**^{277,278} (Fig. 5.3d). This would require an intimate mixing of the donor components (that is, alloys) (Fig. 5.3c) such that they become electronically coupled to form a new state. The CT state energy of such a system was shown to be a function of the blend composition and followed the shift in V_{oc} . However, a thorough understanding of the photophysical process in both models is currently still far from accomplished.

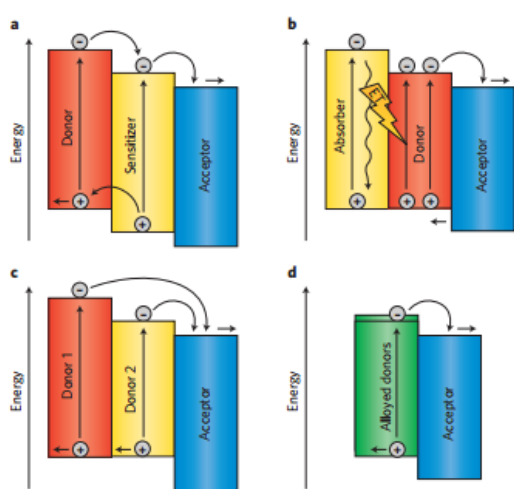


Figure 5.3 Operating mechanisms of ternary blend PSCs. **a**, The charge transfer mechanism. The third component works as a charge relay for electron and hole transport. **b**, The energy transfer (ET) mechanism, where ET occurs between the third component and the host donor material. **c**, The parallel-like model. In this model, the third component forms independent hole-transport channels. **d**, The alloy-like model. The third component and the host donor material are electronically coupled and a new charge transfer state occurs. The vertical arrows show the formation of excitons. The wavy line and the lightning bolt in **b** illustrate ET from the third component to the host donor material.²⁷²

The ternary approach would not tackle the detailed balance limit, but rather improve the photon harvesting in thickness limited photoactive layers, resulting in higher short circuit current densities (J_{sc}) and therefore higher PCEs in a simple single-junction. As such, the ternary solar cell concept avoids the demanding challenges of multi-junction solar cells (tandem) processing for spectrally broad light harvesting.

²⁷⁶ L. Yang, H. Zhou, S. C. Price, W. You, J. Am. Chem. Soc., 2012, 134, 5432.

²⁷⁷ P. P. Khlyabich, B. Burkhardt, B. C. Thompson, J. Am. Chem. Soc., 2012, 134, 9074.

²⁷⁸ R. A. Street, D. Davies, P. P. Khlyabich, B. Burkhardt, B. C. Thompson, J. Am. Chem. Soc., 2013, 135, 986.

Chapter 6: Experimental Procedure

6.1 Basics

In this chapter, the process of manufacturing of Ternary BHJ OPV devices will be described and analyzed. There are some crucial steps, as:

- 4-step cleaning of Anode-ITO substrate
- Deposition of (PFN) ETL
- Preparation and Deposition of Active layer
- Deposition of (MoO_3) HTL
- Aluminum-Cathode deposition

In general, it is desirable to fabricate OPV devices in a cleanroom to produce results with as high a consistency as possible. OPVs are relatively tolerant to atmosphere conditions like air, humidity because of the sensitivity of organic materials. The active layer can also be degraded by oxygen and water, especially in the presence of light. Processing under low intensity red light significantly improves stability of thin films of active layers but it is still essential to minimize the exposure time. Therefore all OPV fabrication steps were proceed inside a Nitrogen (N_2) filled Glove Box.



Figure 6.1 Nitrogen (N_2) filled MBraun glove box for OPVs fabrication.

One of the most important factors in a fabrication run is the handling of the substrates. Substrates should in general only be handled with tweezers (Fig. 7.2) and care must be taken to avoid touching the active areas as this will scratch the films

and cause failures due to shorting of the anode and cathode.



Figure 6.2 Tweezer for device safe handling

The figure below (Fig. 6.3) shows the active areas, which must not be touched by tweezers and also the safe handling zone.

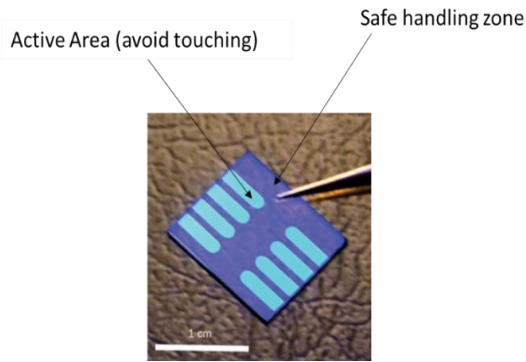


Figure 6.3 Illustration of safe handling zone and active area of an OPV device²⁷⁹.

It is also important the substrates to be kept the right side up. The right side is easy found by using a multimeter as such the ITO layer is not visible to the naked eye.

Even though a surface can look clean this is not the same as a surface being chemically clean. Where the active surface has been in contact with other surfaces (even clean surfaces such as cleanroom tissues) this typically leads to device defects and device “pollution” (e.g. dust). As such, substrates that have been dropped and landed active face down should be discarded for best device data.

6.2 Substrate Cleaning Process

As it was above referred, there is a 4-step cleaning process followed for ITO-coated substrates. First we insert the substrates into a holder with the ITO-coated side of all substrates to the same direction and then immersion of them into a beaker with soap water, (10%)-deionized water (First step of substrate cleaning process), as it is seen in Fig. 6.4. Then ultrasonic bath follows for 10 min (Fig. 6.5).



Figure 6.4 Preparation for substrate cleaning and the first step of substrate cleaning process.



Figure 6.5 Ultrasonic bath.

Next, follows rinsing of substrates with deionized water in order to fend off soap from the surface. Second step is immersion in acetone and then again ultrasonic bath for 10 minutes. Third step is to rinse substrates with Isopropyl alcohol or Isopropanol (2-propanol, IPA) and then to immerse them in a beaker with IPA. Last ultrasonic bath for 10 min. Then,

²⁷⁹ <http://www.photonics.com/m/Article.aspx?AID=54750>

substrates are transferred from the holder to a Petri-dish with the ITO-coated side upwards and then placed in oven at 120 °C for 15 minutes for drying (Fig. 6.6).



Figure 6.6 Substrates are placed to an oven for drying.

Last step is placement of the substrates inside a vacuum UV-ozone cleaner chamber (Fig. 6.7) for 15 min. at $\sim 1\text{mW}/\text{cm}^2$ in order to remove any residual organic contamination.



Figure 6.7 Manual MBRAUN MB-UV-O₃-Cleaner²⁸⁰.

6.3 Deposition of Electron transport layer (ETL), PFN

6.3.1 Solutions of HTL, PEDOT:PSS, and HTL, PFN.

- **PEDOT:PSS** (HTL, Conventional structure)

PEDOT:PSS (Heraeus, Ch. 2.3.2) is dispersed in distilled water and was kept in a fridge at approximately 5 °C.

- **PFN** (ETL, Inverted structure)

²⁸⁰ <http://mbraun.de/products/encapsulation-equipment/uv-cleaning/mb-uv-o3-cleaner>

PFN (see Ch. 2.3.1) solution (powder, purchased from Solaris) with concentration 0.5mg/1ml, was dispersed in 1ml of methanol (MeOH) and 2µl of Acetic acid (CH₃COOH, in gastronomy “vinegar”) and let stirring overnight.

6.3.2 Spin-coating technique

The deposition occurred by spin coating (Fig. 6.10). Spin coating is a very useful technique for deposition of thin uniform films on planar substrates. It's a very simple process, illustrated in Fig. 6.11. A solution is placed on the substrate, the substrate is rotated at an adjustable angular velocity resulting to the spreading of the liquid due to centripetal force.

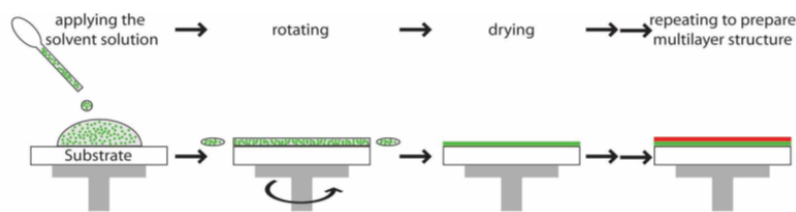


Figure 6.11 Spin coating Procedure

The rotation continues for an adjustable time.

The time and the speed of rotation determine the amount of solution that will remain on the substrate (and hence the layer thickness) as shown by the formula 6.1 with layer thickness (t), the (c) the viscosity of material in connection with the concentration and angular rotational velocity. (6.1)

$$t = \frac{\eta(c)}{\sqrt{\omega}}$$

Once the rotation terminates the sample is allowed to dry and the procedure repeated with another solution for the manufacture of multilayer. This technique was used for the deposition of both buffer layers, between the ITO and the active layer, (HTL and ETL for the conventional and the inverted structure, respectively) and also the active layer of the different devices (in atmosphere and in inert conditions (N₂) for the conventional and inverted structures, respectively).

The next layer after the ITO Anode for a Conventional structure is the HTL, PEDOT:PSS, and for an Inverted is the ETL, PFN, as referred in the Ch. 2. Experiments have shown that this type of PEDOT:PSS layer is optimal at 5000rpm for 60 sec in order to achieve a thickness of ~ 30nm (and surface resistance <800/sq) for PCDTBT:PC₇₁BM system. To minimize the use of material (and therefore the cost) deposition can be done by pipetting, leaving only 50µl at the center of the substrate. To maximize the performance, the samples with imperfections that can be observed by the naked eye, rejected. The results are presented in the next chapter.

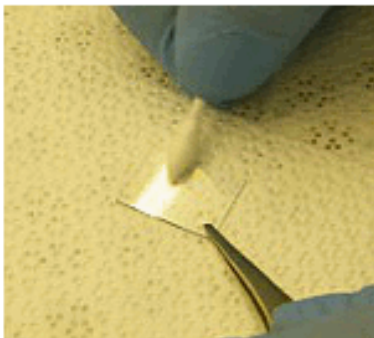


Figure 6.12 Cleaning PEDOT:PSS with a cotton swab

Following the spin coating process, a stripe of PEDOT: PSS layer at both edges of the square substrate, swabbed with a cotton bud wetted with deionized water (Fig. 6.12). This strip is removed in order to ensure the contact of the electrode with the ITO layer and not with PEDOT: PSS. The PEDOT: PSS removal is very easy, since it is water soluble. The whole process carried out outside glove box since there was no infrastructure. Finally, the substrates were placed in an oven at 120°C for 15 minutes in order to

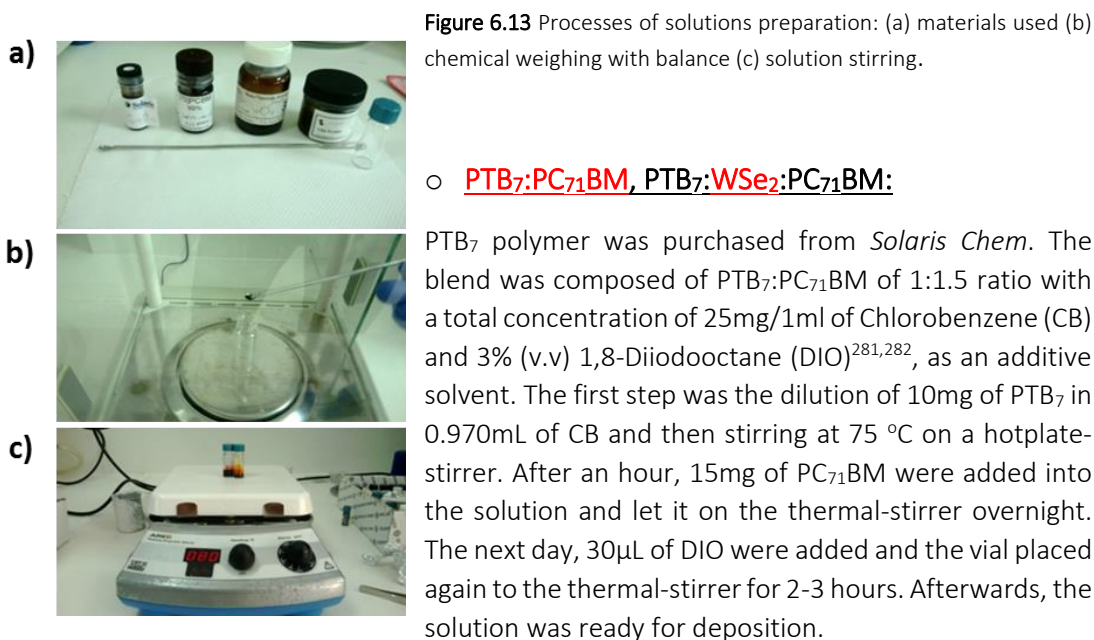
remove any humidity residues. It is extremely important to note that the exposure time of PEDOT: PSS in the air should be minimized because the performance deteriorates rapidly. The humidity of the atmosphere is a negative factor because can lead to morphological changes due to the creation of an insulating layer on the surface, which is rich in PSS and deteriorate the performance.

On the other hand for the Inverted structure and PFN layer (ETL), the optimal spin-coating conditions were at 1000 rpm for 65sec but, in order to achieve layer thickness of approximately ~10nm multilayers were used. Specifically, 4 layers of PFN solution were deposited with a thermal treatment of 150°C for 30sec between each spin-coating. Similarly, 50µl were used at each spin coating.

6.4 Blends and deposition of the Active layer (A.L)

6.4.1 Solutions' Preparation

A big amount of different blend solutions were prepared with different polymers and extra components inside the active layer. The only material that was common to all prepared blends was the acceptor material, the fullerene derivative PC₇₁BM.



Addition of WSe₂ flakes into the binary PTB₇:PC₇₁BM active layer:

The WSe₂ based ternary blends, are prepared by separately adding the different WSe₂ samples (sample 1, sample 2 and sample 3), in different concentrations (1.5%, 2.0%, 2.5% v/v), in the as prepared binary dispersions. All the ternary blends are stirred for at least 3 hours at 75 °C before their deposition in order to ensure the dispersion of the WSe₂ flakes in the polymer:fullerene matrix and the removal of the residual ethanol solvent.²⁸³

○ PTB₇:Compound T:PC₇₁BM:

Initially, PTB₇:PC₇₁BM solution was prepared by the same procedure as mentioned above. In addition, 10 mg of small molecule, Compound T, were diluted in 0.5 ml of CB in a different vial and let overnight at thermal-stirring at 75 °C. The next day, different concentrations (3, 5, 10, 15 % (v.v) with respect to the total concentration of the binary blend, PTB₇:PC₇₁BM) of T were added in the as prepared binary dispersion. During the experimental procedure, the ternary blend was spin-coated for 35 s at 1500 rpm. Then the substrates were dried in active vacuum for 15 min. Notable is that no thermal treatment was used during the deposition of the active layers.

○ c44/cc52/cc72/SD5/SD6:PC₇₁BM:

Five different solutions were prepared with polymer:fullerene ratio of 1:3 (3.75 mg : 11.25 mg, respectively). As a first step each LBG polymer was dissolved in 980 μl CB and stirred for an hour at 90 °C. Afterwards, the fullerene derivative, PC₇₁BM added and the solution stirred overnight at the same temperature. The procedure followed by the addition of 20 μl of DIO

²⁸¹http://www.sigmaaldrich.com/catalog/product/aldrich/250295?lang=en®ion=GR&gclid=CjwKEAjw3pTJBRC hgZ3e7s_YhAkSJAASG9VrZc_bgpWXR6JbmRWUTcN3WWpvq0UCx1-SjmmVFCzTkRoC9OHw_wcB

²⁸² L. Zhao, S. Zhao, Z. Xu, B. Qiao, D. Huang, X. Xu, *Organic Electronics*, 2016, 34, 188.

(2%). At least 3 hours before the deposition the temperature has to be increased to 110 °C and also the substrates have to be at same temperature for a homogeneous film. As well, the experimentalist has to be really quick during the spin-coating because if there is a big difference between the solution and the substrate temperatures, then the film is going to have a lot of inhomogeneities, which is an undesirable result. This was a very anxious situation, every time an experiment was taking place.

- cc165:PC₇₁BM, cc165:RGO:PC₇₁BM:

A cc165:PC₇₁BM was prepared with same steps as the previous LBG polymers solutions.

Addition of RGO into the binary cc165:PC₇₁BM active layer:

RGO was fabricated due to the method described in Ch. 4.1, afterwards it was dispersed in CB solvent and then for ultrasonication for a couple of hours. Then, different quantities of the dispersion was added into the cc165:PC₇₁BM solution.

6.4.2 Deposition of the Active layer (A.L)



Figure 6.14 Spin coating the active layer.

The third step during the manufacturing of an organic solar cell is the deposition of the “OSC engine”, the photoactive layer. After the preparation of active layers (6.4) an approximate thickness of 100nm of **a)** PCDTBT:PC₇₁BM, **b)** PCDTBT:WS₂:PC₇₁BM, **c)** PCDTBT:WS₂-Au:PC₇₁BM, **d)** PTB₇:PC₇₁BM, **e)** PTB₇:T:PC₇₁BM, **f)** cc165:PC₇₁BM and **g)** cc165:RGO:PC₇₁BM were deposited by spin coating method Error! Bookmark not defined. inside the glove box. For each different structure were prepared at least 50 devices and it

took a lot of time for detecting the best fabrication conditions and also reaching the best efficiencies because some materials were tested for the first time like cc165 LBG polymer. The most efficient devices are presented in the next chapter (Ch. 7).

Afterwards, the stripe of photoactive layer, was swabbed by the same procedure as previously described for PEDOT:PSS but, with chloroform (CF) solvent. First, for cases a), b) and c) the fabricated devices were dried at 60 °C for 1 min and subsequently a Ca interlayer. For d) and e) there was no thermal treatment. As well, for cases f) and g) the devices were dried at 85°C for 5min. Furthermore, for d), e), f) and g) inverted structures 8nm of MoO₃ were deposited via thermal evaporation using a shadow mask (Fig. 6.18). Commonly, for all different structures an Al top electrode of 100nm was deposited through the same shadow mask by thermal evaporation (see below) to complete device architecture, creating an active area of 0.04 cm² or 4mm².

6.5 Deposition of Ca, MoO₃ Interface layers and Al negative electrode using Vacuum Thermal Evaporation (VTE) method.

In the laboratory of Prof. E. Kymakis,²⁸⁴ a thermal vacuum evaporator into a glove box is provided, which is very important as it ensures that a TVE of atmosphere sensitive materials (in this case Aluminum and Calcium) will be possible to be achieved as they stay unharmed into the glove box (Fig. 6.15).



Figure 6.15 Our thermal evaporator into the MBrown glove box.

A different deposition technique is the vacuum thermal evaporation (VTE). In this process, small pieces of material (in this case Ca, MoO₃ and Al pellets), are placed in a cavity enclosed within a vacuum chamber. The substrate that is to become the coating is placed on a special base, which is known as

the “boat”, over the cavity. If the chamber is under the appropriate vacuum conditions (around $2 \cdot 10^{-6}$ bar), then the cavity is supplied with current and due to its Ohmic resistance it is heated and the material pieces melt and evaporate. The vaporized molecules of the material overlay on the substrate and form the coating. The coating thickness depends on the distance of the substrate from the cavity (source evaporation) and the time of supply with electricity. The overlay can be made on specific parts of the substrate with the use of shadow masks (Fig. 6.16), leaving uncovered the points we want cover with the material.



Figure 6.16 Placing the substrates in a cathode deposition mask.

6.6 Device Characterization

The performance of cells and modules can be described by their current versus voltage ($I-V$) characteristics under conditions of darkness and light. Measurement equipment, procedures, and artifacts are discussed for $I-V$. The most common performance indicator is the photovoltaic (PV) efficiency under standard reporting conditions (SRC)

²⁸⁴ <http://nano.teicrete.gr/#facilities>

(temperature, spectral irradiance, total irradiance). The efficiency is the maximum electrical power divided by the total irradiance.

A computer controlled voltage and current sources provide the voltage difference and the current across the device. The software that is used is the *Easy EXPERT* (Fig. 6.19). A lamp that simulates the solar spectrum illuminates (under AM 1.5 conditions) the OPV device under characterization. As a matter of shorthand, the global and direct terrestrial reference spectra are often referred to as AM1.5 G and AM1.5 D, respectively. Many groups often just refer to the reference spectrum as AM1.5. This can be confusing without a reference because numerous different AM1.5 reference spectra have been proposed and used in the past. It should be noted that neither the direct reference spectrum nor the global reference spectrum actually integrates to exactly 1000 W/m^2 ^{285,286,287,288}. The global reference spectrum integrates to approximately 963 W/m^2 and the direct reference spectrum integrates to approximately 768 W/m^2 . Different numerical integration methods give differences in the integrated or total irradiance of the reference spectra at the 0.1% level because of the relatively small number of data points (120) and the large variations in the spectral irradiance with wavelength. The structure in the spectral irradiance is a function of bandwidth. The bandwidth in the spectral irradiance at any given wavelength is approximately the difference in wavelength between adjacent points. The PV community has arbitrarily taken the term “one sun” to mean a total irradiance of 1000 W/m^2 (100 mW/cm^2)²⁸⁸. In fact, the spectral irradiance of the global reference spectrum normalized to 1000 W/m^2 in Figure 6.17 exceeds the AM0 spectral irradiance in the infrared, which is not physically possible without concentration. The term *global* refers to the spectral irradiance distribution on a 37° tilted south-facing surface with a solar zenith angle of 48.19° (AM1.5). The term *direct* refers to the direct-normal component (5° field of view) of the global spectral irradiance distribution²⁸⁹. The term AM1 or AM1.5 is often used to refer to standard spectra, but the relative optical air mass (AM) is a geometrical quantity and can be obtained by taking the secant of the zenith angle. For AM1, the zenith angle is 0° . The relative optical air mass can be pressure-corrected to an absolute air mass by multiplying by the barometric pressure and dividing by the sea level pressure. In outer space the pressure is zero so the absolute air mass is always zero. The internationally accepted global reference spectrum is based upon the 1962 US standard atmosphere with a rural aerosol distribution as input to a sophisticated Monte Carlo ray tracing model for wavelengths up to 2500 nm and an undocumented simple direct-normal spectral model for the irradiances from 2500 nm to 4050 nm^{286,287,289}. The fact that the reference spectrum only approximates the “real-world” spectra at solar noon is unimportant as long as the differences between the photocurrents are the same for various PV.

²⁸⁵ Standard ASTM E891-92, *Standard for Terrestrial Solar Direct Normal Solar Spectral Irradiance Tables for Air Mass 1.5*, American Society for Testing and Materials, West Conshocken, PA, USA.

²⁸⁶ Standard ASTM E892-92, *Standard for Terrestrial Solar Spectral Irradiance Tables at Air Mass 1.5 for a 37° Tilted Surface*, American Society for Testing and Materials, West Conshocken PA, USA.

²⁸⁷ Standard IEC 60904-3, *Measurement Principles for Terrestrial PV Solar Devices with Reference Spectral Irradiance Data*, International Electrotechnical Commission, Geneva, Switzerland.

²⁸⁸ Bird R, Hulstrom R, Riordan C, *Sol. Cells*, 1985, 14, 193.

²⁸⁹ Bird R, Hulstrom R, Lewis L, *Sol. Energy*, 1983, 39, 563.

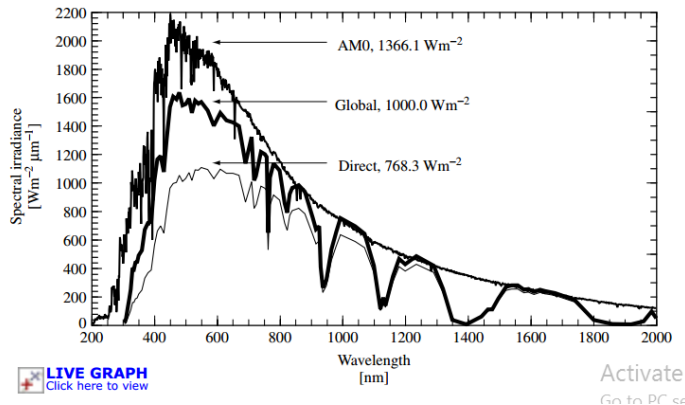


Figure 6.17 Global, Direct, and AM0 reference spectra listed (Annual Book of ASTM Standards, Copyright ASTM).

Returning to the experimental procedure, the OPV device is placed in a specific direction such as the different deposited layers side to face the illumination lamp.

6.6.1 Optical absorption spectroscopy (OAS)

Optical absorption spectroscopy (OAS) of all different devices was carried out in a Cary Varian 5000UV-Visspectrophotometer. With this measurement, a lot of information about the absorption pics and range of the active layer materials was collected (Ch. 7).

6.6.2 (I-V) measurement

The procedure during this measurement starts with: the lamp is turned on and the power is set in order to act as sun simulator ($100\text{mW}/\text{cm}^2$). A reference monocrystalline silicon solar cell from *Newport* was used to calibrate the lamp in “one sun” (it needs almost 15 min.), as referred above. Then, a similar procedure occurs to obtain the current-voltage curve under illumination. After the device placing into the characterization set-up, the necessary wiring follows. Initially, we bring together two metal probes of Ossila test board (Fig. 6.18) the one is conducted with the ITO electrode (Anode), while the other is also connected with ITO legs in order to avoid aluminum cathode scratching, due to its sensitivity when touching with the probe. ITO patterning allows to use ITO legs as the Cathode electrode, as thankfully there is binding between the Al electrodes and the ITO legs. On the other hand, it is inefficient as a 100nm ITO layer has a sheet resistance of $20\ \Omega/\text{sq}$ (referred in Ch. 2.1.1) and a 100nm Aluminum layer $2.5\text{--}3\ \Omega/\text{sq}$, thus we lose in conductivity but we avoid the possibility of a short circuit phenomenon after a scratch to the Al electrodes.



Figure 6.18 A test board for making electrical connections to the photovoltaic (8 pixel substrates) substrates.²⁹⁰

Afterwards, the whole layout is covered with a black cloth to start the measurement process under dark conditions. We launch the *Easy EXPERT software*, select solar cell mode, set the range and step voltage and the time that will elapse between the measurements and finally we obtain the corresponding current-voltage curve in the dark. The algorithm of the program calculates important values for solar cells like current density (J)

²⁹⁰ <http://www.ossila.com/products/pv-test-board-push-fit>

and short circuit current density (J_{sc}), open circuit voltage (V_{oc}), maximum efficiency (P_{max}), fill factor (FF), cell efficiency (PCE%).



Figure 6.19 Easy Expert program for I-V measurements.

6.6.3 External Quantum Efficiency measurement

The external quantum efficiency (EQE) measurements were conducted immediately after device fabrication using an integrated system (Enlitech, Taiwan) and a lock-in amplifier with a current preamplifier under short-circuit conditions (Fig. 6.20). The light spectrum was calibrated using a monocrystalline photodetector of known spectral response. The OPV devices were measured using a Xe lamp passing through a monochromator and an optical chopper at low frequencies (~ 200 Hz) in order to maximize the signal/noise (S/N) ratio.

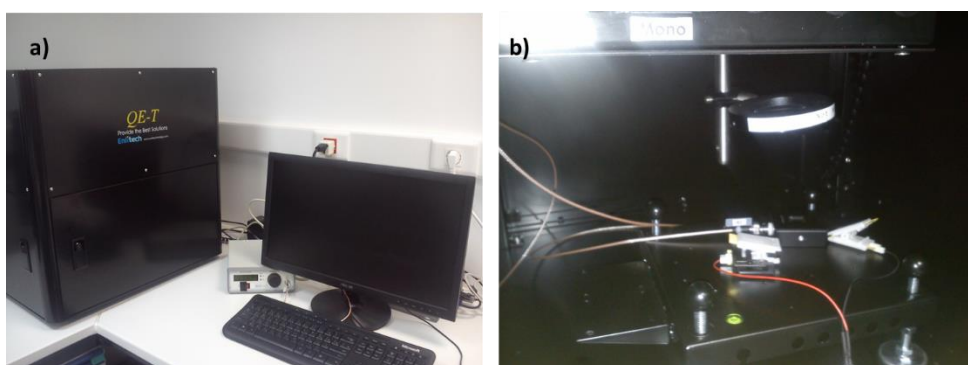


Figure 6.20 a) Enlitech system for external quantum efficiency (EQE) measurements b) Interior of Enlitech system.

Finally the curves and the values which obtained by Easy Expert software are processed by *Origin 9 Pro*.

6.6.4 Calculation of Hole/Electron mobilities via SCLC method

Many different methods have been used to determine charge carrier mobility in organic materials such as *Hall effect measurement*,²⁹¹ conductivity/concentration method,²⁹² space-charge-limited-current (SCLC),²⁹³ transient space-charge-limited-current,²⁹⁴ organic field effect

²⁹¹ K. Morgan, R. Pethig, *Conduction in Low Mobility Materials*, 391, 1971.

²⁹² P. H. Nguyen, G. Paasch, W. Brütting, W. Riess, *Phys. Rev. B*, 1994, 49, 5172.

²⁹³ A. J. Campbell, D. D. C. Bradley, H. Antoniadis, *J. Appl. Phys.* 2001, 89, 3343.

²⁹⁴ A. Many, G. Rakavy, *Phys. Rev.* 126, 1980.

transistors (OFET),²⁹⁵ Admittance spectroscopy,²⁹⁶ Time-of-flight (TOF),²⁹⁷ transient electroluminescence²⁹⁸ and Charge extraction by linearly increasing voltage (CELIV).²⁹⁹

To clearly identify the electron mobility and the hole mobility in the different absorption layers, the electron-only devices and the hole-only devices with the corresponding absorption layers were analyzed, respectively, using the space-charge-limited current (SCLC) method. The dark current density-voltage characteristics of the electron-only devices and the hole-only devices with the absorption layers of various pentacene doping contents are presented in the next chapter (Ch.7). The electron mobility of the electron-only devices and the hole mobility of the hole-only devices were estimated based on **Mott-Gurney law** equation shown as follows³⁰⁰:

$$J_{SCLC} = \frac{9}{8} \epsilon_r \epsilon_0 \mu \frac{(V - V_{bi})^2}{d^3} \quad (6.1)$$

in which, ϵ_r is the relative dielectric constant of the active layer, ϵ_0 is the permittivity of free-space, μ is the charge carrier mobility, V is the applied voltage, V_{bi} is the built-in potential and d is the thickness of the active layer.

6.6.5 Conductivity measurement

The direct current conductivity (σ_0) represents an extra clue to better understand the origin of the performance enhancement in the graphene-based inverted PSC and it can be determined from the slope of I–V plot, using the equation:^{301,302}

$$I = \sigma_0 A d^{-1} V \quad (6.2)$$

where A is the active area (0.04 cm²) and d is the thickness of sample (≈ 100 nm), respectively.

6.6.6 Atomic Force Microscopy

What is an AFM?

The atomic force microscope (AFM) is one kind of scanning probe microscopes (SPM)³⁰³. SPMs are designed to measure local properties, such as height, friction, magnetism, with a probe. To acquire an image, the SPM raster-scans the probe over a small area of the sample, measuring the local property simultaneously.

²⁹⁵ G. Horowitz, R. Hajlaoui, D. Fichou, A. El Kassmi, J. Appl. Phys, 1999, 85, 3202.

²⁹⁶ S. W. Tsang, S. K. So, J. B. J. Xu, J. Appl. Phys, 2006, 99, 013706.

²⁹⁷ C. Hosokawa, H. Tokailin, H. Higashi, T. Kusumoto, Appl. Phys. Lett, 1992, 60, 1220.

²⁹⁸ W. E. J. Spear, Non-Cryst. Solids, 1969, 1, 197.

²⁹⁹ J. Lorrmann, B. H. Badada, O. Inganäs, V. Dyakonov, C. Deibel, J. Appl. Phys., 2010, 108, 113705.

³⁰⁰ P. N. Murgatroyd, J. Phys. D: Appl. Phys., 1970, 3, 2, 308, 151.

³⁰¹ Y. Shao, Z. Xiao, C. Bi, Y. Yuan, J. Huang, Nat. Commun., 2014, 5, 5784.

³⁰² J. H. Heo, H. J. Han, D. Kim, T. K. Ahn, S. H. Im, Energy Environ. Sci., 2015, 8, 1602.

³⁰³ <https://www.mobot.org/jwccross/spm/>

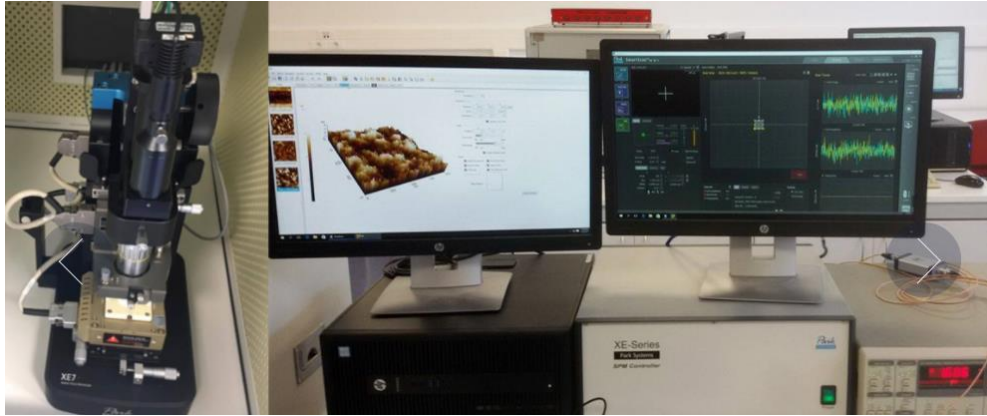


Figure 6.21 Park XE7 AFM³⁰⁴ with Scanning Kelvin Probe Microscopy (SKPM), Dynamic Contact EFM (DC-EFM) and Piezoresponse Force Microscopy (PFM) modes.

How does an AFM work?

AFMs operate by measuring force between a probe and the sample. Normally, the probe is a sharp tip, which is a 3-6 μm tall pyramid with 15-40nm end radius (Figure 6.22).

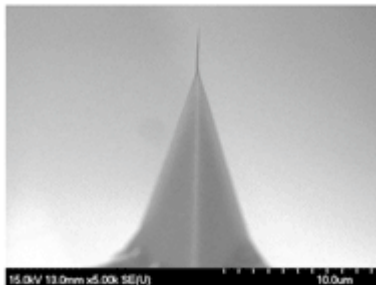


Figure 6.22 The AFM tip. The sharp end of an AFM tip is so brittle that once it touches a sample, it becomes instantly blunt and limits the resolution of an AFM and reduces the quality of the image.

To acquire the image resolution, AFMs can generally measure the vertical and lateral deflections of the cantilever by using the optical lever. The optical lever operates by reflecting a laser beam off the cantilever. The reflected laser beam strikes a position-sensitive photo-detector consisting of four-segment photo-detector. The differences between the segments of photo-detector of signals indicate the position of the laser spot on the detector and thus the angular deflections of the cantilever (Figure 6.23).

³⁰⁴ <http://www.parkafm.com/index.php/products/small-sample-afm/park-xe7/afm-modes>

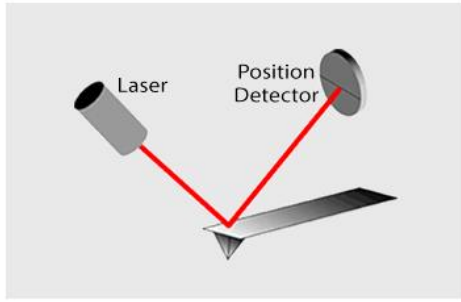


Figure 6.23 Laser beam deflection for atomic force microscopes.³⁰⁵

³⁰⁵ <http://www.nanoscience.com/technology/afm-technology/how-afm-works/>

Chapter 7: Results and Discussion

Thin film photovoltaic cells based on solution processable organic semiconductors have attracted remarkable interest as a possible alternative to conventional, inorganic photovoltaic technologies. The introduction of bulk-heterojunction (BHJ) architecture acquired a potentiality because combines the high absorption coefficient of the organic materials and the efficient generation of photo-induced charge carriers (electron-hole pairs/excitons) under the condition of using a thin film³⁰⁶. Furthermore, a thin AL would increase the exciton dissociation in the D:A interface but, absorption of BHJ thin film would be significantly decreased³⁰⁷. The promising approach of Ternary solar cells was developed as a solution to to overcome some of the main limitations of OSC technology, as: broad absorption bandwidth and efficient charge collection.

7.1 PROJECT 1: PTB7:WSe₂:PC₇₁BM

An ambitious solution to overcome the limitations of binary BHJ OSCs, and thus improve their PCE, is the use of a third component material into the active layer,²⁷² to form a ternary BHJ OSC structure. A big amount of materials have been utilized, yielding PCE enhancement with respect to the binary blend in different ways: by broadening the absorption bandwidth of the active layer,³⁰⁸ by means of either the addition of a second acceptor³⁰⁹ or second donor material,³¹⁰ by contributing to energy or charge transfer,³¹¹ or, finally, by improving the photogenerated charge dissociation³¹² (see Ch. 5).

In this context, the 2D material WSe₂, which belongs to the family of TMD materials was used as an additional material inside the active layer. WSe₂ is owned significant properties, as the high charge carrier mobility (~ 202 and ~ 140 cm² V⁻¹ s⁻¹ for electrons and holes, respectively)³¹³ and the high absorption coefficient (10^5 to 10^6 cm⁻¹, in the visible^{314,315,316} and near-infrared region^{317,318,319}) of fulfill the requirements of a third component in a BHJ OSC. Most importantly, the valence band (VB) position of single-layer WSe₂ is calculated to be 4.9 eV, while its

³⁰⁶ C. J. Brabec, S. Gowrisanker, J.J.M. Halls, D. Laird, S. Jia, S.P Williams, *Adv. Mater.* 22, 3839 (2010).

³⁰⁷ S. H. Park, A. Roy, S. Beaupr_, S. Cho, N. Coates, J. S. Moon, D. Moses, M. Leclerc, K.Lee, A. J. Heeger, *Nat. Photonics*, 3, 297 (2009).

³⁰⁸ J. S. Huang, T. Goh, X. Li, M. Y. Sfeir, E. A. Bielinski, S. Tomasulo, M. L. Lee, N. Hazari, A. D. Taylor, *Nat. Photonics*, 2013, 7, 479.

³⁰⁹ Y.-Y. Lai, Y.-J. Cheng, C.-S. Hsu, *Energy Environ. Sci.*, 2014, 7, 1866.

³¹⁰ P. P. Khlyabich, B. Burkhart, B. C. Thompson, *J. Am. Chem. Soc.*, 2012, 134, 9074.

³¹¹ T. Liu, L. Huo, X. Sun, B. Fan, Y. Cai, T. Kim, J. Y. Kim, H. Choi, Y. Sun, *Adv. Energy Mater.*, 2016, 6, 1502109.

³¹² R. A. Street, D. Davies, P. P. Khlyabich, B. Burkhart, B. C. Thompson, *J. Am. Chem. Soc.*, 2013, 135, 986.

³¹³ W. Liu, J. Kang, D. Sarkar, Y. Khatami, D. Jena, K. Banerjee, *Nano Lett.*, 2013, 13, 1983.

³¹⁴ R. F. Frindt, *J. Phys. Chem. Solids*, 1963, 24, 1107.

³¹⁵ H. J. Lewerenz, A. Heller, F. J. DiSalvo, *J. Am. Chem. Soc.*, 1980, 102, 1877.

³¹⁶ D. Mahalu, L. Margulis, A. Wold, R. Tenne, *Phys. Rev. B*, 1992, 45, 1943.

³¹⁷ W. Zhao, Z. Ghorannevis, L. Chu, M. Toh, C. Kloc, P.-H. Tan, G. Eda, *ACS Nano*, 2013, 7, 791.

³¹⁸ M. Lotya, *J. Am. Chem. Soc.*, 2009, 131, 3611.

³¹⁹ U. Khan, A. O'Neill, M. Lotya, S. De, J. N. Coleman, *Small*, 2010, 6, 864.

conduction band (CB) is positioned at 3.6 eV with respect to the vacuum level.³²⁰ The valence band maximum shifts from Γ (single-layer WSe₂) to K (bulk WSe₂), determining a shrink of the energy band gap with a crossover from direct to indirect³²¹ (Fig. 7.1).

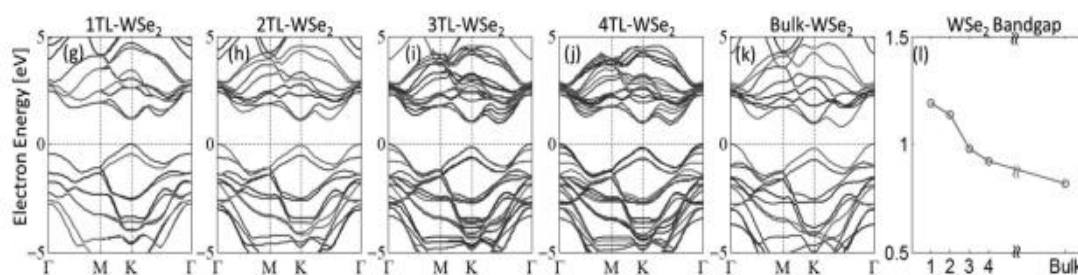


Figure 7.1 Electronic band structures of 1–4TL, bulk WSe₂ and their band gaps.³²²

Therefore, WSe₂ energy levels (see Fig. 7.2) are placed in between the ones of the PTB7-donor (3.3 eV) and PC₇₁BM-acceptor (4.3 eV), enabling an efficient **electron-cascade transfer (ECT)**. Critical to the optimization of the aforementioned processes is the morphology of the final blend and, thus, how the third component mixes with the other two materials.³²³



Figure 7.2 Energy level diagram of the layers consisted in the Ternary OSC.

For this purpose, WSe₂ flakes with controlled morphological properties (i.e., area and thickness) were homogeneously mixed in the thin layer (typically ~100 nm) of polymer–fullerene composite. ^{Error! Bookmark not defined.} The WSe₂ nanoflakes with different sizes were produced by liquid phase exfoliation (LPE)^{324,325,326} of bulk WSe₂ in ethanol (EtOH), and sorted by lateral size by means of ultracentrifugation, exploiting the sedimentation-based separation (SBS) approach (Fig. 7.3).^{327,328,329} EtOH was used as the main solvent in the 3 different WSe₂ solutions, a low boiling point organic solvent, and also compatible with the PTB7:PC₇₁BM blend

³²⁰ C. Gong et al., Appl. Phys. Lett., 2015, 107, 139904.

³²¹ P.-C. Yeh et al., Phys. Rev. B, 2015, 91, 041407.

³²² W. Huang, X. Luo, C. K. Gan, S. Y. Quek, G. Liang, Phys. Chem. Chem. Phys., 2014, 16, 10866.

³²³ G. J. Hedley, A. J. Ward, A. Alekseev, C. T. Howells, E. R. Martins, L. A. Serrano, G. Cooke, A. Ruseckas, I. D. W. Samuel, Nat. Commun., 2013, 4, 2867.

³²⁴ D. Gerchman, A. K. Alves, J. Colloid Interface Sci., 2016, 468, 247.

³²⁵ F. Bonaccorso, A. Bartolotta, J. N. Coleman, C. Backes, Adv. Mater., 2016, 28, 6136.

³²⁶ V. Nicolosi, M. Chhowalla, M. G. Kanatzidis, M. S. Strano, J. N. Coleman, Science, 2013, 340, 1226419.

³²⁷ F. Bonaccorso, A. Lombardo, T. Hasan, Z. Sun, L. Colombo, A. C. Ferrari, Mater. Today, 2012, 15, 12.

³²⁸ Y. Hernandez, V. Nicolosi, M. Lotya, F. M. Blighe, Z. Sun, S. De, I. T. McGovern, B. Holland, M. Byrne, Y. K. Gun'ko, J. J. Boland, P. Niraj, G. Duesberg, S. Krishnamurthy, R. Goodhue, J. Hutchison, V. Scardaci, A. C. Ferrari, J. N. Coleman, Nat. Nanotech., 2008, 3, 563.

³²⁹ O. M. Maragò, F. Bonaccorso, R. Saija, G. Privitera, P. G. Gucciardi, M. A. Iat'i, G. Calogero, P. H. Jones, F. Borghese, P. Denti, V. Nicolosi and A. C. Ferrari, ACS Nano, 2010, 4, 7515.

preparation and can be easily removed by low-temperature annealing or vacuum.^{330,331} The as-prepared WSe₂ samples are mixed with the host donor material PTB7 and the acceptor material PC₇₁BM to obtain ternary (PTB7:WSe₂:PC₇₁BM) blends used as the active materials for the OSCs. Finally, the resulting photovoltaic performance of the BHJ OSCs is measured to determine the impact of the different WSe₂ flake morphologies on the PCE of inverted ternary BHJ OSCs.

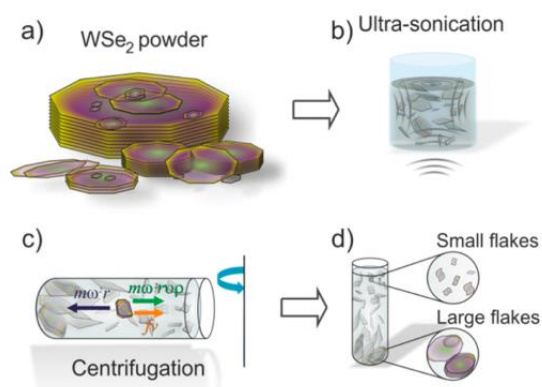


Figure 7.3 Schematic representation of the WSe₂ flakes liquid-phase exfoliation (LPE) process. (a) The bulk WSe₂ flakes are exfoliated and dispersed by (b) ultrasonic waves in a solvent and (c) purified by ultracentrifugation by means of the sedimentation-based separation (SBS)³³², promoting (d) the separation of different WSe₂ flake sizes.³³³

The broad distribution of 2D flakes obtained by LPE would make it not possible to get quantitative information on the interplay between WSe₂ flakes, as well as 2D crystals in general, and fullerene domain sizes. To address this issue, in this work there are exploited three different WSe₂ samples. Those with lateral size **below 20 nm** will be referred as **S-WSe₂** (Small), the ones having lateral size in the **30-50 nm** range as **M-WSe₂** (Medium), while the WSe₂ flakes with average lateral size **above 50 nm** as **L-WSe₂** (Large). Fig. 7.4 shows the transmission electron microscopy (TEM) images of the WSe₂ flakes with different lateral sizes, varying from ~10 to ~100 nm, see Fig. 7.5.

The broad distribution of 2D flakes obtained by LPE would make it not possible to get quantitative information on the interplay between WSe₂ flakes, as well as 2D crystals in general, and fullerene domain sizes.

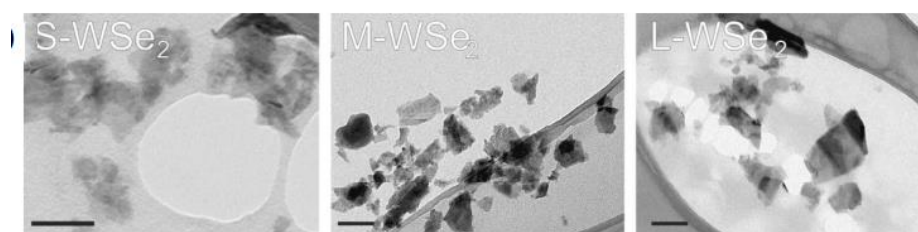


Figure 7.4 Low resolution TEM images of S-WSe₂, M-WSe₂ and L-WSe₂.

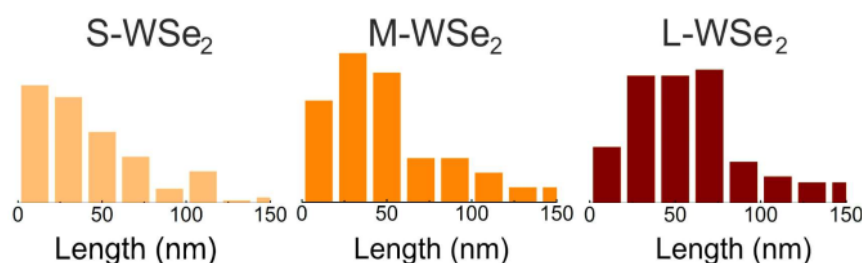


Figure 7.5 Lateral size histograms of the WSe₂ flakes, showing the difference in sizes between the three different samples.

³³⁰ A. Capasso, A. E. Del Rio Castillo, H. Sun, A. Ansaldo, V. Pellegrini, F. Bonaccorso, *Solid State Commun.* 2015, 224, 53.

³³¹ H. Sun, A. E. Del Rio Castillo, S. Monaco, A. Capasso, A. Ansaldo, M. Prato, D. A. Dinh, V. Pellegrini, B. Scrosati, L. Manna, F. Bonaccorso, *J. Mater. Chem. A* 2016, 4, 6886.

³³² J. Kang, V. K. Sangwan, J. D. Wood, M. C. Hersam, *Acc. Chem. Res.*, 2017, 50, 4, 943.

³³³ G. Kakavelakis, A. E. Del Rio Castillo, V. Pellegrini, A. Ansaldo, **P. Tzourmpakis**, R. Brescia, M. Prato, E. Stratakis, E. Kymakis, F. Bonaccorso, 2017, *ACS Nano*, 2017, 11, 4, 3517.

UV-vis absorption spectra of the binary and the ternary blend films with different size WSe₂ nanoflakes incorporated inside PTB7:PC₇₁BM are shown in Fig. 7.6a. As it is easy observed, the incorporation of M- and L-WSe₂ flakes enhances the absorption inside the BHJ, while the addition of S-WSe₂ flakes does not determine a change in the absorption spectrum of PTB7:S-WSe₂:PC₇₁BM, with respect to the one of PTB7:PC₇₁BM. This could be attributed to the low absorbance intensity of S-WSe₂, as reported in Figure 7.6b.

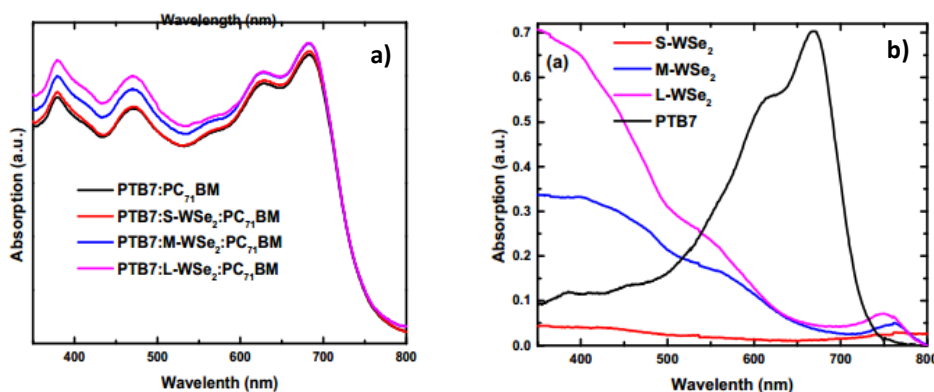


Figure 7.6 (a) UV-Vis absorption spectra of the pristine and S-M-L-WSe₂ nanoflakes doped PTB7:PC₇₁BM blends in solid films and (b) UV-Vis absorption spectra of S-M-L-WSe₂ nanoflakes and PTB7 polymer donor in ethanol and chlorobenzene solutions.

In addition, the PV performance of the above ternary system was investigated on the basis of the following conventional device structure: indium tin oxide (ITO)/poly(3,4-ethylene-dioxythiophene): poly(styrene-sulphonate) (PEDOT:PSS) / PTB7:WSe₂: PC₇₁BM /Ca/Al. The different WSe₂ samples were incorporated as additives in the photoactive layer, by simple mixing them in different ratio until the best characteristics were observed. The typical current density (current divided with the active area of each device, 0.04 cm²) versus voltage (J-V) graphs of each device with the 3 different lateral sizes of WSe₂ nanoflakes under simulated AM 1.5 G illumination at 100 mW*cm⁻² are been reported in Fig. 7.7a. The corresponding photovoltaic performance parameters are summarized in Table 7.1. The addition of S-WSe₂ into the host binary blend, determined an enhancement of PCE (~7.67%) with respect to the reference PTB7:PC₇₁BM-based cell. Ternary devices with M-WSe₂ exhibited the best photovoltaic performance with an average PCE of 8.56%, (maximum PCE of 8.78%). This represents more than 15% increase in PCE with respect to the reference PTB7:PC₇₁BM-based binary device. Ternary devices based on L-WSe₂ have shown an average PCE of 7.98% (maximum PCE=8.16%), which is higher with respect to the reference PTB7:PC₇₁BM-based cell, but lower if compared with the ternary BHJ OPVs based on M-WSe₂.

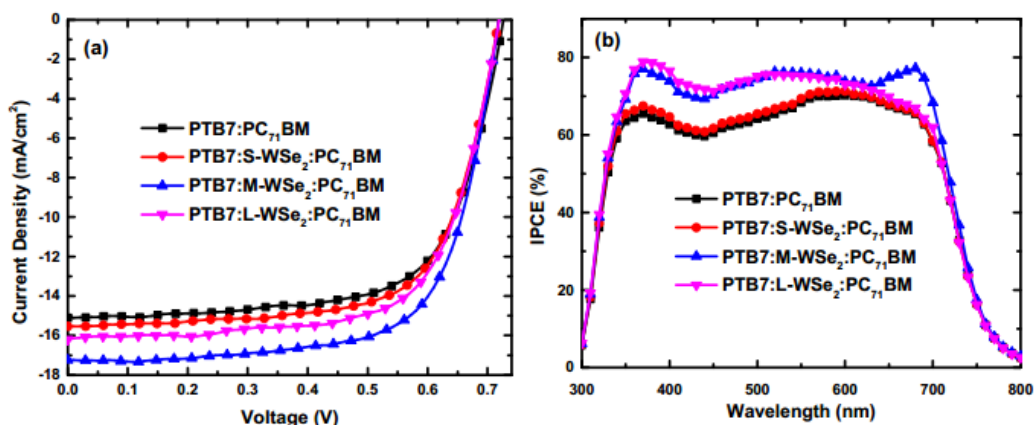


Figure 7.7 (a) Current density–voltage (J–V) curves for the pristine and the S-M-L WSe₂ based devices and (b) IPCE spectra for the devices with and without different sized WSe₂-based active layers.

Table 7.1. Photovoltaic parameters of the fabricated OPV devices with and without the different WSe₂ nanoflakes incorporated inside the photoactive layer.

Active layer	J _{sc} (mA*cm ⁻²)	Calculated J _{sc} (IPCE)	V _{oc} (V)	FF (%)	PCE _{MAX} (%)
PTB7:PC ₇₁ BM (Reference)	15.10 ± 0.19	14.88 ± 0.24	0.728 ± 0.03	67.2 ± 0.3	7.38 (7.54)
PTB7:S- WSe ₂ :PC ₇₁ BM	15.53 ± 0.24	15.07 ± 0.21	0.720 ± 0.02	68.6 ± 0.4	7.67 (7.86)
PTB7:M- WSe ₂ :PC ₇₁ BM	17.24 ± 0.25	16.69 ± 0.35	0.719 ± 0.0.3	69.1 ± 0.4	8.56 (8.78)
PTB7:L- WSe ₂ :PC ₇₁ BM	16.20 ± 0.23	15.92 ± 0.32	0.721 ± 0.02	68.4 ± 0.3	7.98 (8.16)

**Average photovoltaic characteristics and standard deviations for the different structured OPV devices. The numbers in parentheses represent the values obtained for the champion OPV cells. To account for experimental errors, the reported averages and deviations for each device are taken for 10 identical devices, consisting of six cells each.

Incident photon to current conversion efficiency (IPCE) or external quantum efficiency (EQE) spectra of the ternary devices are shown in Fig. 7.7b. IPCE spectra of M- and L-WSe₂-based OPV devices increased by ~10% with respect to the PTB7-PC₇₁BM-based reference OPV in a wide wavelength range, i.e., from 350 to 700 nm. Specifically, the reference OPV exhibits a maximum IPCE of ~70%, while the M- and L-WSe₂ based devices reached an IPCE of ~80%. It is important to note that the integrated J_{sc} values from the IPCE spectrum as presented in Table 7.1 for the reference and the WSe₂-based ternary devices are in good agreement with the actual J_{sc} values measured from the J-V curves, showing a less than 3% difference. By a direct comparison between the IPCE (Fig. 7.7b) and the UV–Vis absorption spectra of the BHJ films, shown in Fig. 7.7a, emerges that the IPCE enhancement is not entirely due to changes in the absorption properties upon WSe₂ nanoflakes addition. In addition, it is worth to mention that the addition of L-WSe₂ nanoflakes gives rise to higher light absorption intensity compared to the M-WSe₂ one but, on the other hand M-WSe₂ based device rises up better PV performance. Therefore it is understood that by exploring only the absorption spectra someone would not end up to an absolutely safe conclusion. This confusion of the aforementioned results indicates the presence of an additional mechanism responsible for the IPCE enhancement especially at the absorbance

region of PTB7 polymer (550-750nm). Furthermore, LUMO energy levels of PTB7, WSe₂ and PC₇₁BM constructed a cascade structure (Fig. 7.2). Thus, WSe₂ could act as electron cascade material to aid electron extraction from PTB7 to PC₇₁BM after photo-excitation and charge separation.³³⁴

In order to further investigate this assumption, devices designed for the evaluation of electron and hole only transport properties were fabricated. The two devices have the following structure: ITO/Al/PEDOT:PSS/Active layer/Ca/Al for electron-mobilities and ITO/PEDOT:PSS/Active layer/Au for hole-mobilities, respectively. These devices allow to study possible variations in charge carriers mobility of the reference PTB7:PC₇₁BM OPVs and the devices incorporating WSe₂ flakes. Calculations are based on *Mott–Gurney equation* as is analytically described in *Ch. 6.6.4*. The μ values for the tested devices are summarized in Table 7.2. The results demonstrate an increase of the electron mobility (μ_e) for the WSe₂ based devices with respect to the reference PTB7:PC₇₁BM-based OPV. The highest μ_e value was achieved with the M-WSe₂ ternary blend (see Fig. 7.8a). Contrary to the μ_e results, there is not significant difference in hole mobilities (μ_h) of the ternary OPVs compared to the reference PTB7:PC₇₁BM one (Fig. 7.8b). However, despite no variation upon WSe₂ addition to the PTB7:PC₇₁BM blend for the μ_h , the significant increase in μ_e determine a balancing of the μ_h and μ_e for the WSe₂-based devices. Furthermore, the ratio of μ_h/μ_e for the reference device is 1.65 while for the WSe₂-based device is significantly lower, e.g., 1.09 for the M-WSe₂-based device (see Table 7.2). The μ_h and μ_e balancing is fundamental to avoid charge accumulation in the device.^{335,336} This is an important result because electron transport is considered a limiting factor for the photocurrent generation in the conventional PTB7:PC₇₁BM-based devices, since the μ_e is, generally, much lower than μ_h . Also, table 7.3 presents the comparison between the μ_h/μ_e ratio of all devices, where M-WSe₂-based device have 13.5% and 10% improvement of the mobilities ratio compared to S- and L-WSe₂-based devices. This improvement is even higher valued in case of the reference device, where it is 34%.

Table 7.2. Electron and hole mobilities of the reference and the devices with WSe₂ based ternary OPVs.

Active layer	μ_h (cm ² V ⁻¹ s ⁻¹)	μ_e (cm ² V ⁻¹ s ⁻¹)	μ_h/μ_e
PTB7:PC ₇₁ BM (Reference)	(1.30±0.02) x 10 ⁻⁴	(7.86) x 10 ⁻⁵	1.65
PTB7:S- WSe ₂ :PC ₇₁ BM	(1.33±0.02) x 10 ⁻⁴	(1.05±0.02) x 10 ⁻⁴	1.26
PTB7:M- WSe ₂ :PC ₇₁ BM	1.31(±0.02) x 10 ⁻⁴	(1.20±0.02) x 10 ⁻⁴	1.09
PTB7:L- WSe ₂ :PC ₇₁ BM	(1.32±0.02) x 10 ⁻⁴	(1.09±0.01) x 10 ⁻⁴	1.21

Table 7.3. Comparison of μ_h/μ_e ratio of all devices.

³³⁴ F. Bonaccorso, N. Balis, M. M. Stylianakis, M. Savarese, C. Adamo, M. Gemmi, V. Pellegrini, E. Stratakis, E. Kymakis, *Adv. Funct. Mater.*, 2015, 25, 3870.

³³⁵ S. Foster, F. Deledalle, A. Mitani, T. Kimura, K.-B. Kim, T. Okachi, T. Kirchartz, J. Oguma, K. Miyake, J. R. Durrant, S. Doi, J. Nelson, *Adv. Energy Mater.*, 2014.

³³⁶ D. Konios, G. Kakavelakis, C. Petridis, E. Stratakis, E. Kymakis, *J. Mater. Chem. A*, 2016, 4, 1612.

	Reference	S-WSe ₂	W-WSe ₂	L-WSe ₂
S-WSe ₂	31.0%	----	13.5%	4.00%
W-WSe ₂	51.0%	15.6%	----	11.0%
L-WSe ₂	36.0%	4.10%	10.0%	----
Reference	----	23.7%	34.0%	26.7%

**GREEN: Improvement, RED: Deterioration

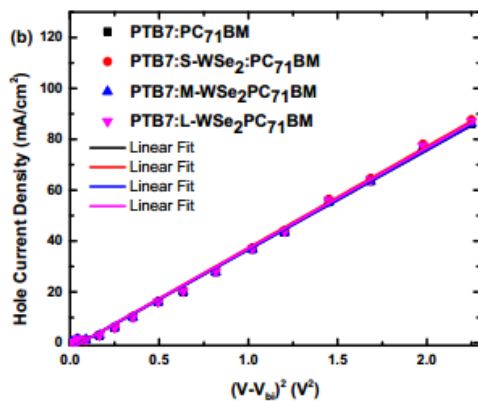
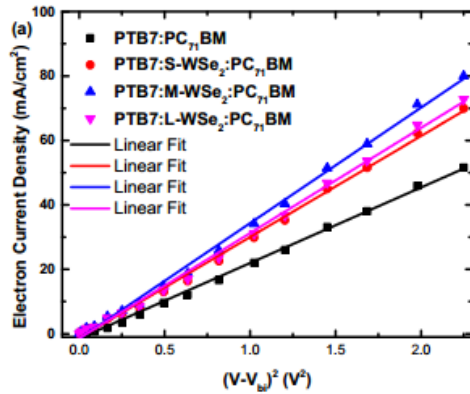


Figure 7.8 J - V^2 characteristics under dark conditions of the fabricated devices for the calculation of (a) electron and (b) hole mobilities using the *Mott–Gurney equation*.

As a result of the aforementioned observations, there is an increased exciton generation after the incorporation of WSe₂ due to the improved J_{sc} . This could be caused by two possible ways. Photoexcited excitons in WSe₂ could directly dissociate at the WSe₂:PC₇₁BM and collected in the electrodes (Two-donors mechanism). This can be observed in the enhancement of the IPCE spectra of ternary devices with M- and L-WSe₂ from 350 to 500 nm, where WSe₂ has shown high absorption intensity. Alternatively, in case that the WSe₂ nanoflakes are in close proximity to the PTB7 polymer, an energy transfer mechanism between PTB7 and WSe₂ can take place,³³⁷ followed by charge separation at the PTB7:PC₇₁BM interface. This explains the increase of the IPCE value from

~620 to ~720 nm for the M-WSe₂ ternary devices and therefore the better PV parameters compared to their “counterparts”, the L-WSe₂-based devices. Last but not least, the strong increase of the IPCE value, which is only observed in the case of M-WSe₂, could be possibly linked with the light emitting properties.³³³

³³⁷ P. H. Tan, T. Hasan, F. Bonaccorso, V. Scardaci, A. G. Rozhin, W. I. Milne, A.C. Ferrari, *Physica E*, 2008, 40, 2352.

7.2 PROJECT 2: PTB7:Compound_T:PC₇₁BM

Work within the field of OSCs started by utilization of organic small molecules^{338,339} and later on by using functional semiconducting polymers.^{340,341,342} The progress in OPVs in recent years has been tremendous, in particular for vacuum-processed solar cells with small molecules/oligomers as the electronically active material and efficiencies of 5.2% for single junction and 10.7% (*Heliatek*, Germany)³⁴³ for tandem cells have recently been achieved. In this project, a conjugated compound, named T³⁴⁴, (see Ch. 2.2.3), was added into the standard blended active layer PTB7:PC₇₁BM as an active semiconducting third component in order to tackle some of the limitations that binary OSCs, like PTB7:PC₇₁BM, present which are detailed mentioned in previous chapters.

Initially, in Figure 7.9a the UV-vis absorbance spectrum of pristine Comp. T is presented with the two main peaks be at 380 and 480 nm, respectively. In Figure 7.9b the absorption spectrum of the ternary active layer is illustrated. It is shown that as the concentration of Comp. T is increased the more decreased is the absorption peak of the host polymer, PTB7. Also, the common peak of Comp. T and fullerene derivative PC₇₁BM, is further increased as more Comp. T was added.

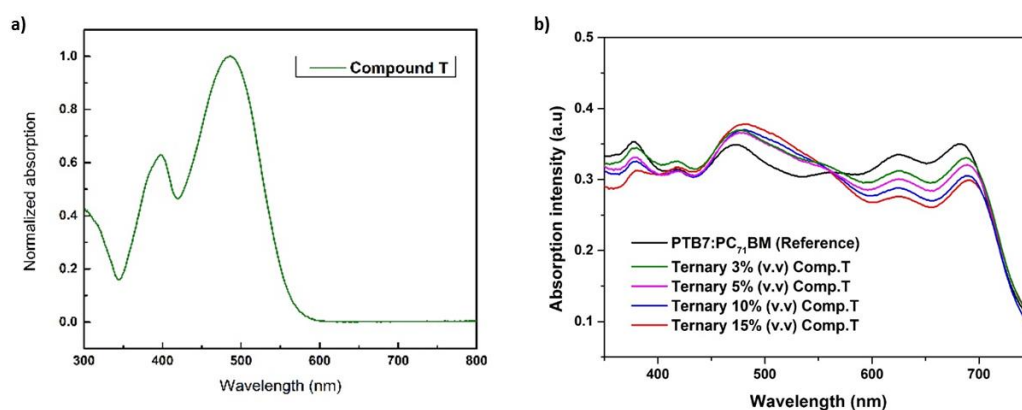


Figure 7.9 UV-vis absorbance spectrum of (a) compound T, (b) reference PTB7:PC₇₁BM and ternary 3, 5, 10, 15% (v.v) Compound T. Complementary absorption spectrums...

Four different ternary inverted devices with different Compound T (Comp. T) see Chapt. 2.2.3) concentration were prepared in order to compare with the inverted reference one. Among them, 5% (v.v) was the most efficient ternary device (see Table 7.4) and the only one

³³⁸ G. A. Chamberlain, *Solar Cells*, 1983, 8, 47.

³³⁹ C. W. Tang, *Appl. Phys. Lett.*, 1986, 48, 183.

³⁴⁰ C. Brabec, V. Dyakonov, U. Scherf, *Organic Photovoltaics: Materials, Device Physics and Manufacturing Technologies*, 2008.

³⁴¹ H. Spanggaard, F. C. Krebs, *Sol. Energy Mater. Sol. Cells*, 2004, 83, 125.

³⁴² H.-Y. Chen, J. Hou, S. Zhang, Y. Liang, G. Yang, Y. Yang, L. Yu, Y. Wu, G. Li, *Nat. Photonics*, 2009, 3, 649.

³⁴³ <http://www.heliatek.com/>

³⁴⁴ J. A. Mikroyannidis, M. M. Stylianakis, Q. Dong, Y. Zhou, W. Tian, *Synth. Met.*, 2009, 159, 14, 1471.

which delivers the highest J_{sc} , FF and PCE (V_{oc} is approximately equal to all). The current density versus voltage (J–V) characteristics of the devices with the 4 different Comp. T concentrations are illustrated and compared with the one obtained by the reference OSC in Figure 7.10a. From EQE graph (Fig. 7.10b) it is shown that 5% (v.v) has the best response at both main absorption peaks, which indicates that in this Comp. T ratio the most efficient charge collection occurs.

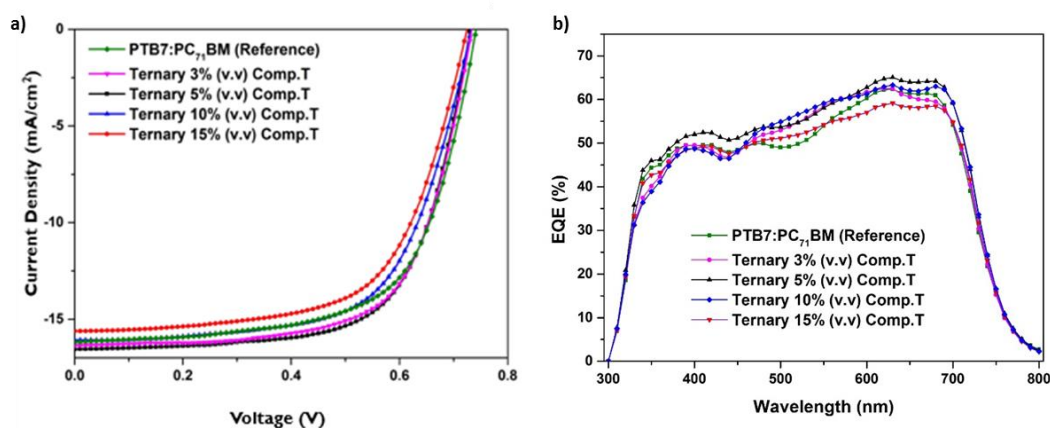


Figure 7.10 (a) Current density–voltage (J–V) and (b) EQE curves for the reference and the 3%-5%-10%-15% Compound T based devices.

The corresponding PV performance parameters are summarized in Table 7.4. The reference PTB7:PC₇₁BM device exhibited a short circuit current density (J_{sc}) of 16.10 mA cm^{-2} , an open circuit voltage (V_{oc}) at 0.729 V, a fill factor (FF) at 65.4% and a PCE of 7.69%. As shown in Table 7.4, J_{sc} was not increased monotonically by increasing the amount of T, instead it increased from 3 to 5% and then started to decay as the concentration of Comp. T increased inside the binary blend. Notably, the V_{oc} obtained in the ternary cells is identical to the binary PTB7:PC₇₁BM, reflecting an energy cascade between the HOMO and LUMO energy levels of the three components (Figure 7.11).

As it is presented in a lot of publications, two broad absorption peaks at around 614 and 682 nm are attributed to the characteristic π – π^* transition of the PTB7 polymer.^{345,346} On the other hand, in Figure 7.9a is shown the absorption spectrum and the absorption excitonic peaks at 398 and 486 for the Comp. Thus, Comp. A possible reason for the increased PV parameters in the case of 3% and 5% ternary devices is that, T could act as electron cascade material to aid electron extraction from PTB7 to PC₇₁BM after photo-excitation and charge separation. A further PL measurement of Comp. T emission may insight if there is also an energy transfer phenomenon.

Table 7.4. Photovoltaic parameters of the fabricated OPV devices with and without the different WSe₂ nanoflakes incorporated inside the photoactive layer.

Active layer	J_{sc} ($\text{mA}\cdot\text{cm}^{-2}$)	Calculated J_{sc} (IPCE)	V_{oc} (V)	FF (%)	PCE_{MAX} (%)
--------------	--	-------------------------------	-----------------	-----------	----------------------------------

³⁴⁵ Z. Liu, H. Ju, E.-C. Lee, Appl. Phys. Lett., 2013, 103, 133308.

³⁴⁶ S. Ochiai, S. Imamura, S. Kannappan, K. Palanisamy, P.-K. Shin, Curr. Appl. Phys., 2013, 13, S58.

PTB7:PC ₇₁ BM (Reference)	16.10	0.73	65.4	7.69
PTB7:3% (v.v) Comp.T:PC ₇₁ BM	16.44	0.73	65.9	7.96
PTB7:5% (v.v) Comp.T:PC ₇₁ BM	16.70	0.73	66.5	8.11
PTB7:10% (v.v) Comp.T:PC ₇₁ BM	16.06	0.73	64.0	7.50
PTB7:15% (v.v) Comp.T:PC ₇₁ BM	15.61	0.72	63.3	7.11

**Average photovoltaic characteristics and standard deviations for the different structured OPV devices. The numbers in parentheses represent the values obtained for the champion OPV cells. To account for experimental errors, the reported averages and deviations for each device are taken for 10 identical devices, consisting of six cells each.



Figure 7.11 Energy level diagram of the ternary blend components.

In Figure 7.12a, the Photoluminescence (PL) spectrum of the Comp. T ensures that in fact there is an energy transfer mechanism between Comp. T and PTB7, as the emission of the latter is included in the absorption spectrum of the host polymer PTB7 (see Fig. 7.12a and Fig. 2.8). Furthermore a PL intensity decay is observed after the addition of 5% Comp. T, which corresponds to a more efficient exciton dissociation compared to the reference one.

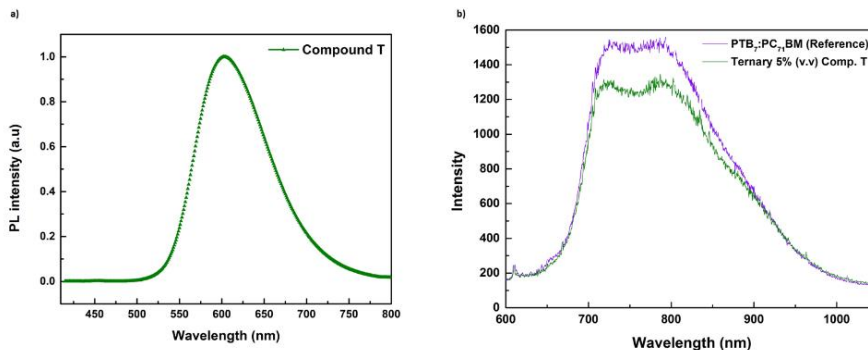


Figure 7.12 Photoluminescence spectra of (a) Comp. T and (b) reference PTB7:PC₇₁BM (violet) and ternary 5% (v.v) Compound T (green).

In order to ensure that Comp. T has the role of an electron cascade material, electron and hole only devices were fabricated (Fig. 13) designed for the evaluation of charge transport properties. The two devices had the following structure: ITO/PFN/Active layer/Ca/Al for electrons and ITO/PEDOT:PSS/Active layer/MoO₃/Au for holes, respectively. These devices allow to study possible variations in charge carriers mobility of the reference PTB7:PC₇₁BM OPVs and the devices incorporating small molecule Comp. T. Calculations were based again on *Mott–Gurney equation*.

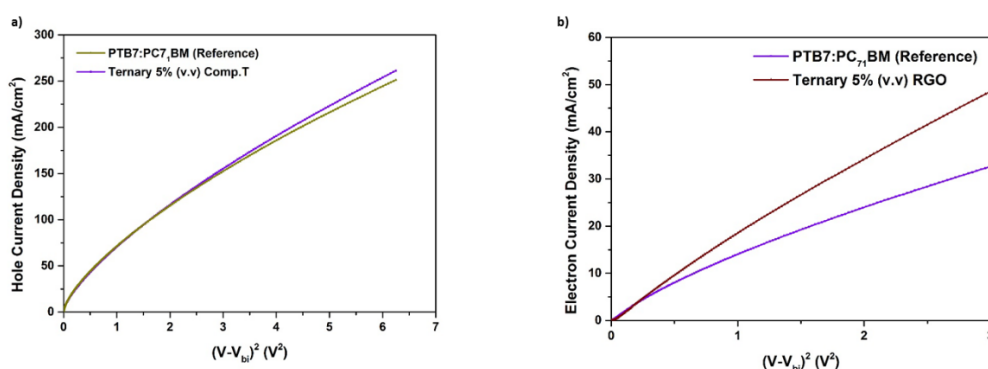


Figure 7.13 J - V^2 characteristics under dark conditions of the fabricated devices for the calculation of (a) electron and (b) hole mobilities using the *Mott–Gurney equation*.

The μ_h , μ_e values are summarized in Table 7.5, where it is obvious that the incorporation of Comp. T into the binary solution improved both but to a greater extent the μ_e , an outcome that confirms the previous assumption for an electron-cascade-role of Comp. T. As well the μ_h/μ_e ratio is closer to absolute one for the ternary device, so this addition helped to an improved μ_h - μ_e balancing, which is fundamental to avoid charge accumulation in the device, as has also been referred previously.

Table 7.5. Electron and hole mobilities of the reference and the devices with Comp.T based ternary OPVs.

Active layer	μ_h ($\text{cm}^2 \text{V}^{-1} \text{s}^{-1}$)	μ_e ($\text{cm}^2 \text{V}^{-1} \text{s}^{-1}$)	μ_h/μ_e
PTB7:PC ₇₁ BM (Reference)	9.91×10^{-5}	8.01×10^{-5}	1.24
Ternary 5% (v.v) Comp.T	1.01×10^{-4}	8.61×10^{-5}	1.17

Last two extra devices were fabricated, reference and ternary 5% (v.v), for a morphology test. The AFM results (Fig. 7.14) showed a better morphology or a lower roughness (Rms) for the ternary device in a portion of approximately 9.1%. In particular, the Rms for the reference was 1.4nm, on the contrary for the ternary, it showed an Rms of approximately 1.283nm. This is a proof that after the addition of Comp. T better interfaces between Donor-Acceptor were occurred, which indicates the improvement in FF and the other PV parameters.

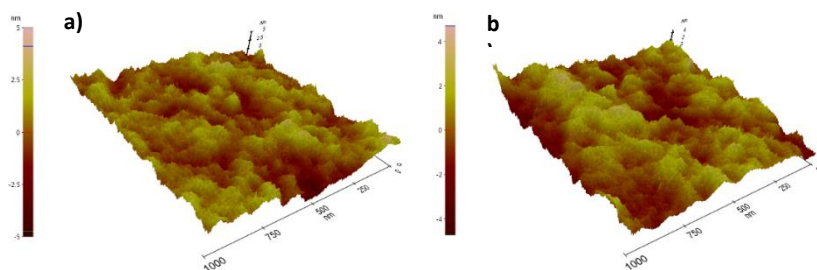


Figure 7.14 AFM images of **a)** reference and **b)** ternary device. The roughness for the reference is 1.4 nm. In addition, for the ternary device there is a significant decrease at 1.283 nm.

7.3 PROJECT 3: Integrated Hybrid Solar cells (IHSCs)

The IHSCs technology is in detail described in Ch. 1.2.4. The commonly used hybrid lead halide perovskite materials, such as MAPbI_3 , $\text{MAPbI}_{3-x}\text{Cl}_x$ and $(\text{FAPbI}_3)_{0.85}(\text{MAPbBr}_3)_{0.15}$ show a light response up to 800 nm due to its optical band gap of 1.55 eV,^{347,348,349} leaving a wide near-infrared region (NIR) untapped. One important strategy to further enhance the PCE of PSCs is to focus on the full utilization of the solar light below 800 nm and another strategy is to broaden the light response to the unexploited longer wavelength region (>800 nm).³⁵⁰

Another approach is the combination of hybrid lead halide perovskite materials with complementary absorbing organic materials with a broad spectral coverage using a tandem cell structure. Building on long charge-carrier diffusion length, high charge carrier mobility and the ambipolar properties of MAPbI_3 , Ding et al. fabricated an integrated solar cell by implanting a bulkheterojunction (BHJ) layer into PSCs.³⁵¹ The low bandgap polymer and PC_{60}BM mixture remarkably broadens the photo-response of PSCs BUT, disappointedly, the integrated device showed lower photovoltaic performance (8.8%) than the more simple PSC only containing PC_{60}BM as ETL (9.5%). Later, Yang et al. improved this concept and reported an interlayer free parallel tandem solar cell by simply integrating $\text{MAPbI}_{3-x}\text{Cl}_x/\text{BHJ}$ together with regular planar structure.³⁵² Correspondingly, the integrated device displayed extended response to solar spectrum and rendered a higher PCE (12.0%), compared with a PSC device based on PBDTT-SeDPP alone (9.7%). Recently, by optimizing the BHJ morphology with a novel n-type polymer (N2200) and a new solvent-processing additive (diphenyl ether), Lee and co-authors reported highly efficient integrated device (PCE = 16.36%) combining a

³⁴⁷ M. Grätzel and N. G. Park et al., *Sci. Rep.*, 2012, 2, 1.

³⁴⁸ A. Kojima, K. Teshima, Y. Shirai, T. Miyasaka, *J. Am. Chem. Soc.*, 2009, 131, 6050.

³⁴⁹ M. M. Lee, J. Teuscher, T. Miyasaka, T. N. Murakami, H. J. Snaith, *Science*, 2012, 338, 643.

³⁵⁰ W. S. Yang, J. H. Noh, N. J. Jeon, Y. C. Kim, S. Ryu, J. Seo, S. I. Seok, *Science* 2015, 348, 1234.

³⁵¹ C. Zuo, L. Ding, *J. Mater. Chem. A*, 2015, 3, 9063.

³⁵² Y. Liu et al., *Nano Lett.*, 2015, 15, 662.

MAPbI₃ layer and an NIR absorbing BHJ.³⁵³ The optimized perovskite/BHJ devices exhibit a dramatically increased current density (from 17.61 to 20.04 mA cm⁻²) due to the additional NIR harvesting, while maintaining the high FF and Voc characteristic of typical PSCs.

In all of above cases mentioned, polymer materials are used as light harvesting materials in BHJ. Additional, except to the polymer materials, small molecular materials have more promising properties, because of their well-defined molecular structure, high purity and smaller batch-to-batch variation. To date, many acceptor-donor-acceptor (A–D–A) structured small molecule materials have been explored as HTLs in PSCs.³⁵⁴ However, none of these reported A–D–A structured HTLs show strong absorption beyond 800 nm due to the fact that deliberate adjustments of the small molecule material's energy levels are needed. As discussed above, this issue can be to some extent solved by forming BHJ with those reported small molecule materials, but the improvement is very limited, because just very little sun-light before 800 nm escapes through perovskite layer.³⁵²

In this project, the main goal was to find the appropriate LBG polymer, which would be the candidate to consist the BHJ active layer that will be deposited up to the perovskite material and efficiently will broad the absorption spectrum of the integrated device, so that the IR region would not more be an “impregnable” region of the light spectrum.

This was the first time of using a LBG polymer as the donor material in BHJ OSC, in the laboratory of Prof. E. Kymakis.²⁸⁴ The DPP LBG polymer cc72 from the beginning seemed to be the right candidate as it has an absorption peak at approximately 791 nm with an offset at approximately 900nm (see Fig. 7.16a) and also from the first experiments, really promising results were observed compared to the other LBG polymers (cc44/cc52/cc72/SD5/SD6) as it is shown in Ch. 7.3.1. The only not satisfying PV parameter of this material was the J_{sc}, as it was lower than other published materials.¹⁰⁸ For this reason, another material was used, C1 or cc165, which from literature presents higher J_{sc} values and all results are shown in Ch. 7.3.2.

7.3.1 A] cc44/cc52/cc72/SD5/SD6:PC₇₁BM

Several research groups within the area of organic photovoltaics are focusing on low band gap polymers, a type of polymer which absorbs light with wavelengths longer than 620 nm.^{89,90,91} These systems are believed to increase the efficiency of organic PVs due to a better overlap of the absorption spectrum of the polymer with the solar spectrum. In this dissertation, different LBG polymers (see Table 7.4) based on diketopyrrolopyrrole (DPP) have been used inside the active layer. Their average band gap (E_g) is 1.4 eV (see Fig. 7.17) and also their maximum absorption pics are in the IR region. Those properties were the motivation for using them inside the binary active layer. For better name-handling, there are encoded names for each LBG and those are presents in Table 7.6.

³⁵³ J. Kim et al., *Adv. Mater.*, 2016, 28, 3159.

³⁵⁴ C. Chen, M. Cheng, P. Liu, J. Gao, L. Kloo, L. Sun, *Nano Energy*, 2016, 23, 40.

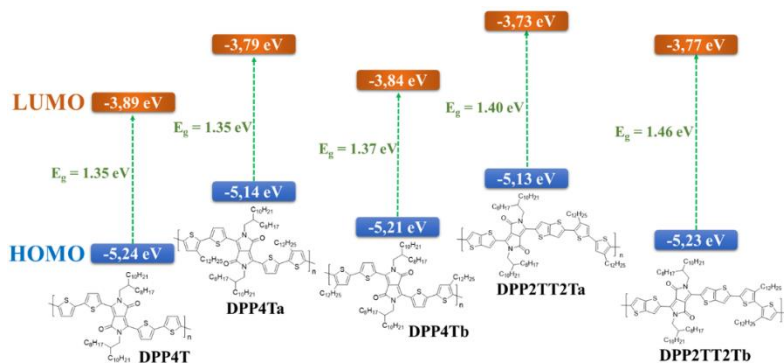
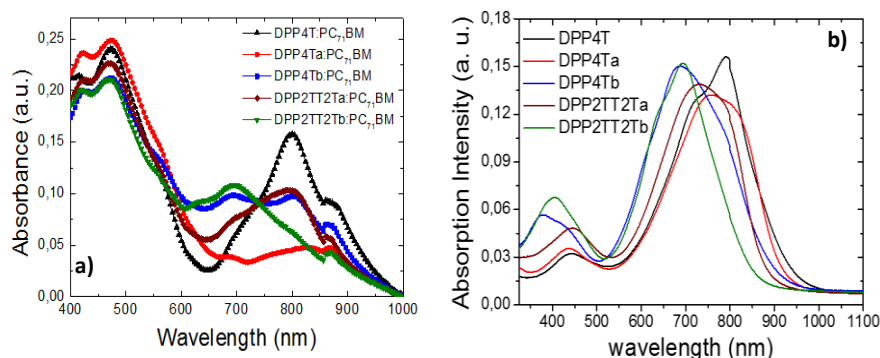


Figure 7.15 Schematic illustration of the IP and EA variation of the new synthesized copolymers.³⁵⁵

Table 7.6 The encoded names of the 5 different LBG polymers used.

Long name	Encoded name
DPP4T	cc72
DPP4Ta	cc52
DPP4Tb	cc44
DPP2TT2Ta	SD6
DPP2TT2Tb	SD5

Absorption spectra of the different LBG polymer donors blended with the PC₇₁BM electron acceptor and the absorption spectra of the copolymers as thin-films are presented in Figure 7.16a and b, respectively. For each copolymer, two major absorption peaks are observed, a characteristic which is commonly observed for alternating D-A copolymers. The low-wavelength peak observed at 442 nm for cc72, at 433 nm for cc52 and at 376 nm for cc44 can be attributed to a delocalized π - π^* transition while the high-wavelength transition is related to an intramolecular D-A charge transfer³⁵⁶ and is detected at 791 nm for cc72 (with an offset at approximately 950nm), at 752 nm for cc52 and at 687 nm for cc44. This shows that the introduction of the didodecyl side chains at the two different positions in the polymer backbone results to blue shifted absorption maxima as compared to the unsubstituted derivative cc72. Especially, the absorption maxima are blue shifted at higher extent when the didodecyl side chains are anchored onto the β -positions, indicating a higher degree of polymer chain distortion preventing the efficient overlapping between the molecular orbitals of the electron rich and electron deficient units as compared to α -positions.



³⁵⁵ C. Chochos, A. Katsouras, S. Drakopoulou, C. Miskaki, M. Krassas, P. Tzourmpakis, G. Kakavelakis, C. Sprau, A. Colmann, B. Squeo, V. Gregoriou, E. Kymakis, A. Avgeropoulos, *Effects of alkyl side chains positioning and presence of fused aromatic units in the backbone of low-bandgap diketopyrrolopyrrole copolymers on the optoelectronic properties of organic solar cells*, Eur. Polym. J., (Submitted).

³⁵⁶ S. Roquet, A. Cravino, P. Leriche, O. Alévêque, P. Frère and J. Roncali, J. Am. Chem. Soc., 2006, 128, 3459.

Figure 7.16 (a) Absorption spectra of the different low band gap polymer donors blended with the PC₇₁BM electron acceptor and **(b)** absorption spectra of DPP4T, DPP4Ta, DPP4Tb, DPP2TT2Ta and DPP2TT2Tb as thin films.³⁵⁵

Based on the J-V curves of Figure 7.17a and the OPV results in Table 7.7, a correlation between structure and OPV characteristics was obtained. By studying the cc52 – cc44 and the SD6 – SD5 pairs it is shown that when the alkyl side chains are introduced on the β-positions (cc44 and SD5) the recorded V_{oc} is higher by ~0.1 V as compared to the representative cc52 and DSD5 where the alkyl side chains are situated on the α-positions in agreement with the results of their HOMO levels alignment (Figure 7.15).

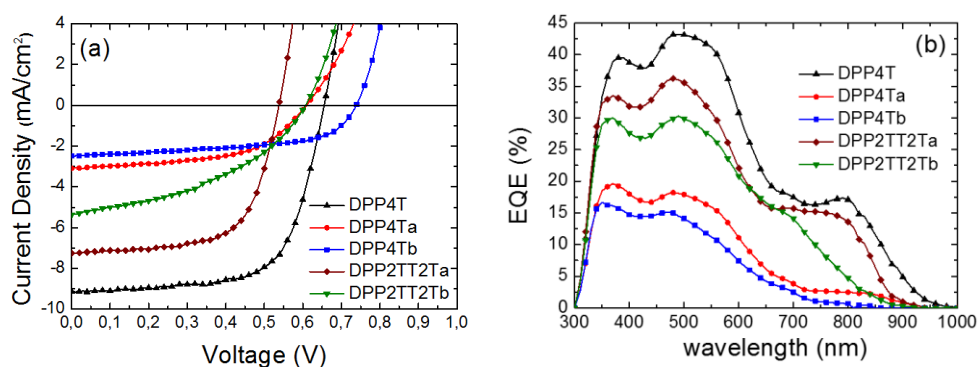


Figure 7.17 (a) Current density-Voltage characteristics and **(b)** external quantum efficiency (EQE) graphs of DPP4T:PC₇₁BM, DPP4Ta:PC₇₁BM, DPP4Tb:PC₇₁BM, DPP2TT2Ta:PC₇₁BM and DPP2TT2Tb:PC₇₁BM inverted solar cells under solar simulator illumination (100 mW cm⁻²).³⁵⁵

Table 7.7 Photovoltaic parameters of the fabricated OPV devices

Active layer	J _{sc} ^{J-V} (mA*cm ⁻²)	Calculated J _{sc} (IPCE)	V _{oc} (V)	FF (%)	PCE _{MAX} (%)
cc72:PC ₇₁ BM	9.2	8.6	0.66	65.5	4.0
cc52:PC ₇₁ BM	3.1	2.9	0.61	52.8	1.0
cc44: PC ₇₁ BM	2.5	2.1	0.74	56.7	1.1
SD6:PC ₇₁ BM	7.2	6.8	0.54	64.7	2.5
SD5:PC ₇₁ BM	5.3	5.5	0.61	42.4	1.4

**Average photovoltaic characteristics and standard deviations for the different structured OPV devices. The numbers in parentheses represent the values obtained for the champion OPV cells. To account for experimental errors, the reported averages and deviations for each device are taken for 10 identical devices, consisting of six cells each.

On the other hand, the J_{sc} values of cc52 and SD6 are higher than those of the representative cc44 and SD5 indicating that the alkyl side chains in the α-positions are the favorable positions towards improved photocurrents. Moreover, it is an evidence that both SD6 and SD5 which contain the fused thieno[3,2-b]thiophene next to the DPP core revealed increased PCEs than those of cc52 and cc44 bearing the thiophene ring around the DPP, mainly due to enhance J_{sc} even if they present slightly higher optical bandgaps versus cc52 and cc44 and lower V_{oc}. Finally, among all the studied DPP-based systems, the unsubstituted cc72 and the cc52 -based devices

demonstrate a photogeneration between 15 and 20% at wavelengths between 700 - 900 nm as clearly observed by the EQE spectra in Figure 7.16b.

Table 7.8 Charge carrier mobilities based on SCLC model of the LBG polymer:PC₇₁BM systems.

Active layer	μ_h (cm ² V ⁻¹ s ⁻¹)	μ_e (cm ² V ⁻¹ s ⁻¹)	μ_h/μ_e
cc72:PC ₇₁ BM	8.91 x 10 ⁻⁵	6.71 x 10 ⁻⁵	1.33
cc52:PC ₇₁ BM	6.03 x 10 ⁻⁵	3.21 x 10 ⁻⁵	1.88
cc44: PC ₇₁ BM	5.50 x 10 ⁻⁵	2.99 x 10 ⁻⁵	1.84
SD6:PC ₇₁ BM	9.10 x 10 ⁻⁵	6.57 x 10 ⁻⁵	1.39
SD5:PC ₇₁ BM	8.05 x 10 ⁻⁵	3.92 x 10 ⁻⁵	2.05

For each system, hole- and electron-only (unipolar) devices were fabricated and their dark J–V characteristics were recorded. For all systems studied, the carrier mobility values were determined based on the *Mott-Gurney equation* as the previous projects. The dark J-V curves are presented in Figure 7.18a, 7.18.b for electron- and hole-only devices, respectively. Table 7.8 summarizes the results of the charge transport characterization of all devices. Based on the results of Table 7.7 and Table 7.8, it is shown that the cc72 and SD6 systems with FF ~ 65% have a mobility ratio more close to 1, meaning that the hole and electron mobilities are balanced within one order of magnitude even though the measured charge carrier mobilities are in the range of 10⁻⁴ to 10⁻⁵ cm²/Vs. These results are partially in agreement with recently published results on solution processed small molecule-based bulk heterojunction (SSM BHJ) solar cells where it was reported that for high FF (> 65%) charge carrier mobilities above 10⁻⁴ cm²/Vs along with balanced hole and electron mobilities are required.³⁵⁷ On the contrary, the systems containing the cc52, cc44 and SD5 exhibited significantly lower FF due to the unbalanced hole and electron mobilities. More unbalanced the charge carrier mobilities, the lower the FF.

³⁵⁷ C. M. Proctor, J. A. Love and T.-Q. Nguyen, Adv. Mater., 2014, 26, 5957.

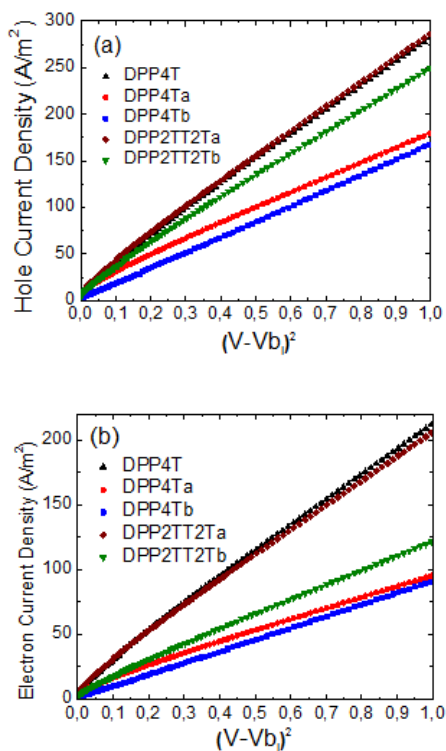
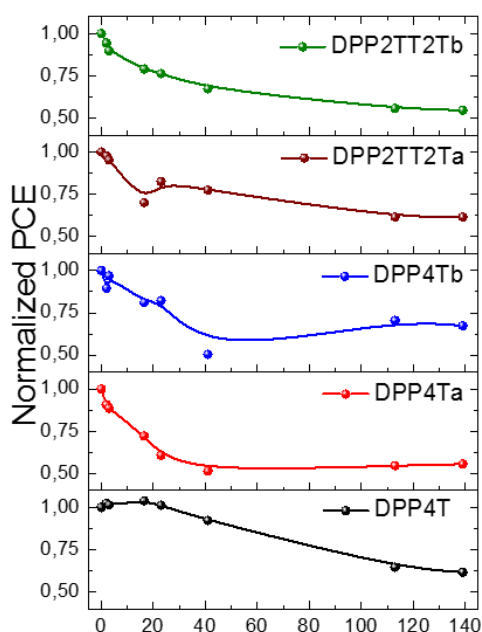


Figure 7.18 J - V^2 characteristics under dark conditions of the fabricated devices for the calculation of (a) electron and (b) hole mobilities using the *Mott–Gurney equation*.³⁵⁵

Research into OPV materials has recently been focused also on improving the photostability of semiconducting polymers. To address this concern, photostability of the synthesized polymers is examined by placing the polymer films under A.M1.5 sunlight illumination in a solar simulator.

The PCEs of the copolymers versus the photodegradation process is presented in Figure 7.19 and individually the photovoltaic parameters of each polymer as function of the photodegradation time are presented analytically in Figures 7.20a–e. After 40 h of illumination by 1 sunlight in air, it is clearly observed that the addition of alkyl side chains onto the polymer backbone, regardless the position, accelerates the photodegradation of the OPV devices as compared to the unsubstituted cc72 (Fig. 7.19). Moreover, it is shown the degradation rate is higher in the cc52 and cc44-based OPV devices than those of SD6 and SD5-based OPV devices (Fig. 7.19), suggesting that the incorporation of fused aromatic systems in the polymer backbone would delay the degradation process. These results demonstrate that the incorporation of fused aromatic rings along with the selection of alkyl side chains enabling the close packing of the polymer chains would contribute to the increased photostability, that is consistent with recently reported findings.³⁵⁸



³⁵⁸ H. S. Lee, H. G. Song, H. Jung, M. H. Kim, C. Cho, J.-Y. Lee, S. Park, H. J. Son, H.-J. Yun, S.-K. Kwon, Y.-H. Kim, B. Kim, *Macromolecules*, 2016, 49, 7844.

Figure 7.19 Photo-stability of polymers:PC₇₁BM solar cells (in air, encapsulated, under AM1.5 illumination at 1 sun) for 140 h.³⁵⁵

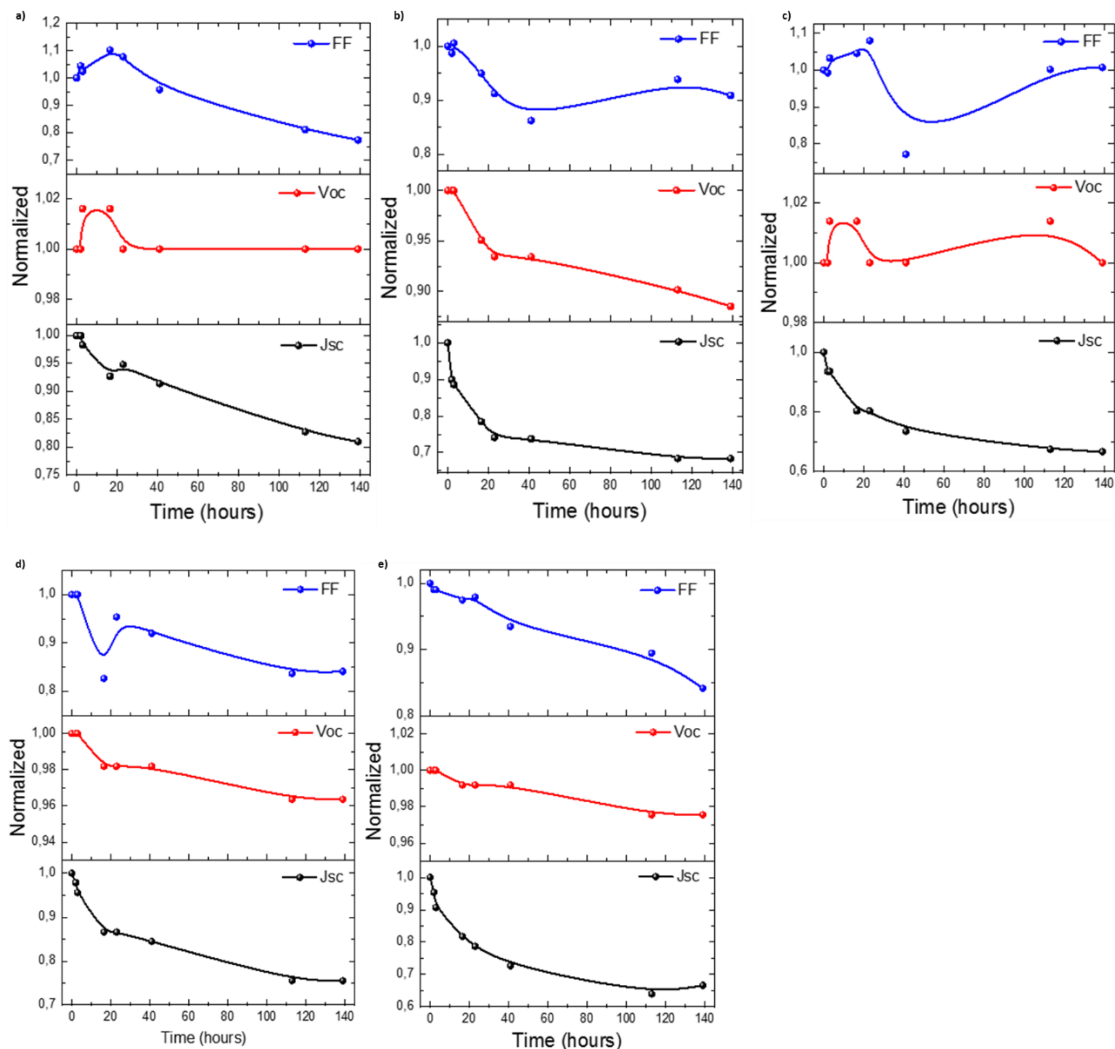


Figure 7.20 Photovoltaic characteristics of (a) cc72:PC₇₁BM (b) cc52:PC₇₁BM (c) cc44:PC₇₁BM (d) SD6:PC₇₁BM and (e) SD5:PC₇₁BM solar cells under photodegradation (in air, encapsulated, under AM1.5 illumination at 1 sun) for 140 h.³⁵⁵

7.3.2 B] cc165:PC₇₁BM, cc165:RGO:PC₇₁BM

To date, one of the most promising classes of LBG polymer materials are diketopyrrolopyrrole (DPP)-based copolymers, which have shown some of the highest solar cell efficiencies reported and have been used to fabricate transistor devices with good ambipolarity and mobilities that routinely surpass $1 \text{ cm}^2 \text{ V}^{-1} \text{ s}^{-1}$.⁸⁸ DPP-based copolymers family is described in detail in Chapter 2.2.2.

In this project, the goal was to use a LBG polymer similar to cc72 that presented promising results (see Ch. 7.3.1), that would give higher values of J_{sc} parameter. Figure 7.21 presents that

cc165 has a significant intensity improvement at the NIR which makes it a better candidate than cc72.

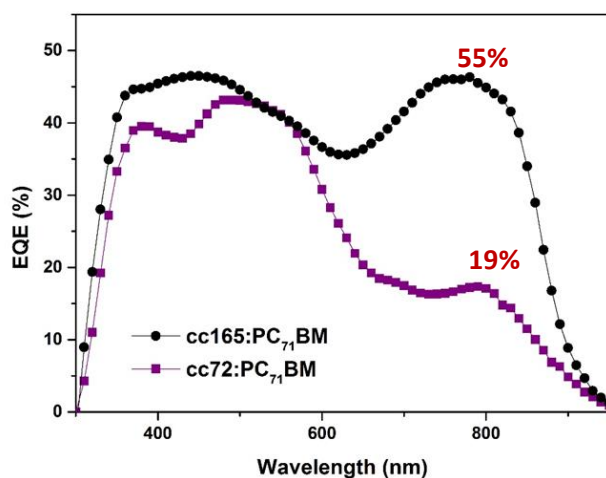


Figure 7.22a presents the UV-vis absorption of pristine cc165 LBG polymer in solution and film form. Pristine cc165 polymer was diluted in Chlorobenzene (5mg/0.5ml). It is shown that the peak at 780nm is slightly red-shifted to 804nm due to the transition from solution to film. In addition, in Figure 7.22 the absorption spectrum of reference and different ternary blend films are illustrated. It is shown that in the case of reference and Ternary 5% (v.v) blends there is an overlap in the whole range of the absorption intensity, which means that it is a very low quantity of RGO and that's why it didn't significantly affect to the absorption of the binary blend. On the other hand, as the concentration of RGO increases into the binary blend, an increase of the intensity is observed. This seems to be straight forward, since it is even obvious for the higher concentrations, 15% and 20%. This on sure, could not be attributed to a complementary absorption of RGO, as its absorption peak is located approximately at 250nm. This may happens because of better donor-acceptor domains, better solubility and so less film inhomogeneities (better film morphology). Film morphology is illustrated in Fig. 7.28 (AFM images).

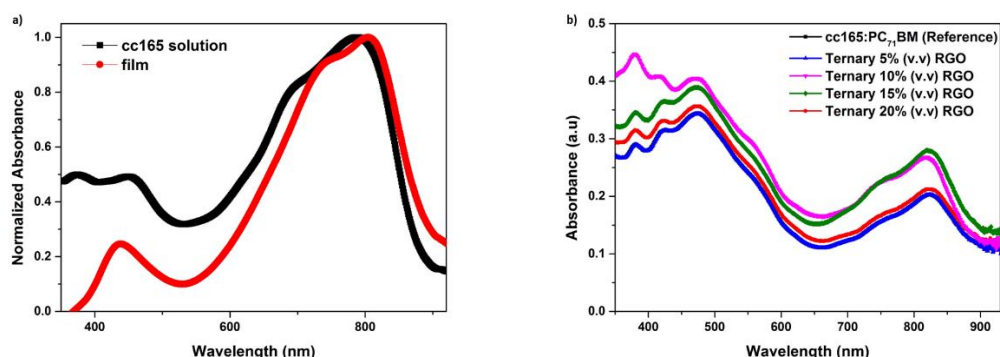


Figure 7.22 (a) Absorbance spectra of (a) pristine cc165 solution and film (b) reference cc165:PC₇₁BM and ternary 5%, 10%, 15% and 20% (v.v) RGO ternary films, respectively.

In addition, the PV performance of the above blend-systems was investigated on the basis of the following inverted device structure: ITO/PFN/cc165:PC₇₁BM/MoO₃/Al and ITO/PFN/cc165:RGO:PC₇₁BM/MoO₃/Al for reference and ternary devices, respectively. The 4 different RGO quantities were incorporated as additives (diluted in CB) in the photoactive layer, by simple mixing them in different volume ratio until the best characteristics were observed. Figure 7.23a illustrates the respective J-V curve for each device. In Figure 7.23b it is shown that 10% (v.v) has better intensity than the other cases, which indicates that 10% (v.v) RGO facilitates for better charge collection.

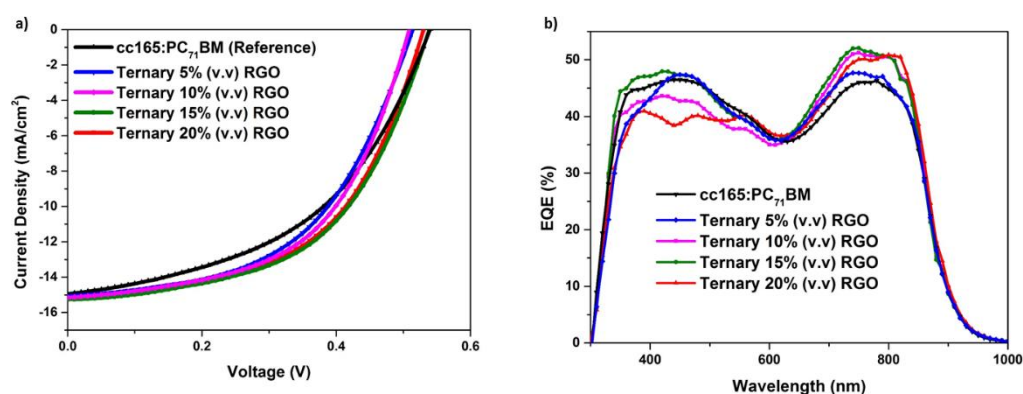


Figure 7.23 (a) Current density-Voltage (b) EQE characteristics of reference and ternary devices.

The corresponding photovoltaic performance parameters are summarized in Table 7.9, where it seems that despite ternary 20% (v.v) RGO exhibits a slight higher (0.4%) J_{sc} value it ends up with a 1.6% lower PCE compared to the 15% as a lower FF value is observed. In addition 15%, as the more efficient quantity, has three of the four parameters increased compared to the reference ones. Specifically J_{sc} increased 4%, FF 4.6% and PCE 8.5%. V_{oc} remained almost constant, which means that the blend was not affected negatively after the addition of RGO.

Table 7.9 Photovoltaic parameters of the fabricated OPV devices

Active layer	J_{sc}^{J-V} (mA*cm ⁻²)	Calculated J_{sc} (IPCE)	V_{oc} (V)	FF (%)	PCE _{MAX} (%)
Reference	15.08		0.53	51.8	4.14

Ternary 5% (v.v)	15.40	0.51	52.6	4.13
Ternary 10% (v.v)	15.52	0.51	53.4	4.23
Ternary 15% (v.v)	15.63	0.53	54.2	4.49
Ternary 20% (v.v)	15.70	0.53	53.1	4.42

**Average photovoltaic characteristics and standard deviations for the different structured OPV devices. The numbers in parentheses represent the values obtained for the champion OPV cells. To account for experimental errors, the reported averages and deviations for each device are taken for 10 identical devices, consisting of six cells each.

Furthermore an intensity decay is observed in the full range of the PL spectra after the addition of 15% RGO as shown in Figure 7.24, which corresponds to a more efficient exciton dissociation compared to the reference one.

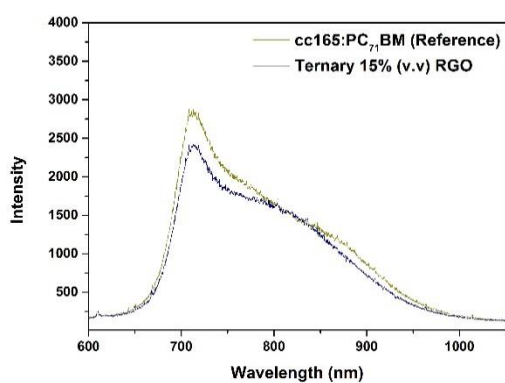


Figure 7.24 Photoluminescence spectra of reference PTB7:PC₇₁BM and ternary 5% (v.v) Compound T.

To better understand the origin of the performance enhancement in the graphene-based inverted PSC, the I–V characteristics were measured in sandwich cells composed by ITO/cc165:PC₇₁BM/Au and ITO/cc165:RGO:PC₇₁BM/Au as reference

and ternary cells, respectively (see Fig. 7.25). The direct current conductivity (σ_0) can be determined from the slope of I–V plot, using the equation $I = \sigma_0 A d^{-1} V$, where A is the area of sample (0.04 cm²) and d is the thickness (100 nm) of sample, respectively. The corresponding conductivity performance parameters are summarized in Table 7.10. The conductivity of reference was 5.12 mS cm⁻¹, whereas the addition of RGO increased dramatically the value of conductivity and almost reached 55% for 15% and 60% improvement for 20% (v.v) RGO. As a result, it is expected that the photogenerated charge carriers in cc165-based absorber are more efficiently transported to the RGO:PC₇₁BM electron conductor than to the pristine PC₇₁BM. The higher conductance of the RGO-based active layers justifies the observed PL quenching (Fig. 7.24), originating from the improved charge extraction from the LBG polymer-based absorber to the Acceptor and further to the HTL/Anode interface. This is not the first time that RGO is used as an additive to further increase the conductivity of an OSC. Kakavelakis and co-workers³⁵⁹ recently showed that by adding a small amount of RGO inside the buffer layer (PCBM) of a planar inverted perovskite SC, resulting in a fivefold higher conductivity. Therefore charge carriers in the perovskite absorber material were more efficiently transported to the RGO:PCBM electron conductor than to the pristine PCBM.

³⁵⁹ G. Kakavelakis, T. Maksudov, D. Konios, I. Paradisanos, G. Kioseoglou, E. Stratakis, E. Kymakis, Adv. Energy Mater., 2017, 7, 1602120.

Figure 7.25 I–V characteristics of ITO/cc165:PC₇₁BM/Au and ITO/cc165:RGO:PC₇₁BM/Au devices.

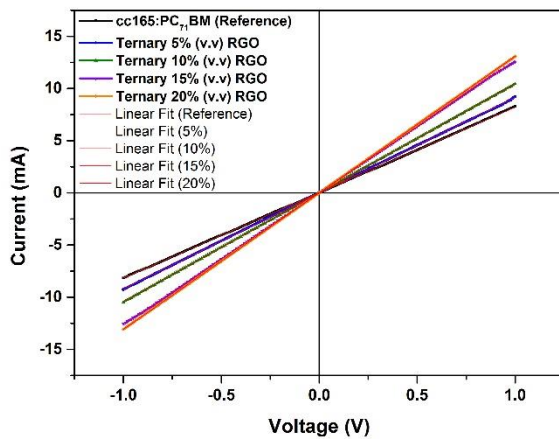


Table 7.10 Conductivity results for each cell and comparison between them.

Active layer	Conductivity (mS*cm ⁻¹)	Conductivity Improvement (REF/previous) (%)
Reference	5.12	—
Ternary 5% (v.v)	5.73	11.9
Ternary 10% (v.v)	6.53	27.5/14.0
Ternary 15% (v.v)	7.93	54.9/21.4
Ternary 20% (v.v)	8.18	59.8/3.15

In order to study the J_{sc} and PCE enhancement of ternary device in respect to the reference one, electron- and hole-only devices were fabricated designed for the evaluation of charge transport properties. The two devices had the following structure: ITO/PFN/Active layer/Ca/Al for electrons and ITO/PEDOT:PSS/Active layer/MoO₃/Au for holes, respectively. These devices allow to study possible variations in charge carriers mobility of the reference cc165:PC₇₁BM OPVs and the device incorporating 15% (v.v) RGO, which achieved the best PV parameters among the other ratio.

Calculations were based again on *Mott–Gurney equation*. The $J-V^2$ graphs for hole- and electron-only devices are illustrated in Fig. 7.26a and b, respectively. In both cases, ternary cell presents higher J values and therefore higher mobilities, indicating better charge transport than the reference device. The only issue for the ternary cell is that the μ_h/μ_e ratio is larger than those of the reference, indicating unbalanced charge carrier mobilities.

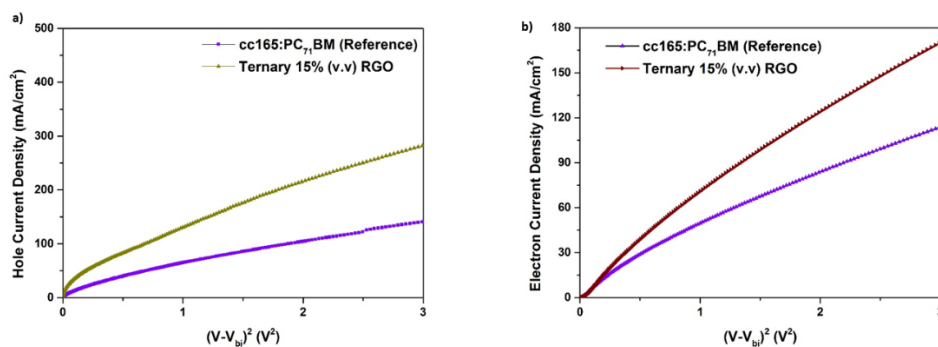


Figure 7.26 $J-V^2$ characteristics under dark conditions of the fabricated devices for the calculation of (a) electron and (b) hole mobilities using the *Mott–Gurney equation*.

Table 7.11 Electron and hole mobilities of the reference and the devices with RGO based ternary OPVs.

Active layer	μ_h ($\text{cm}^2 \text{V}^{-1} \text{s}^{-1}$)	μ_e ($\text{cm}^2 \text{V}^{-1} \text{s}^{-1}$)	μ_h/μ_e
cc165:PC ₇₁ BM (Reference)	$(1.22 \pm 0.02) \times 10^{-4}$	$(1.05 \pm 0.02) \times 10^{-4}$	1.16
Ternary 15% RGO	$(2.43 \pm 0.02) \times 10^{-4}$	$(1.62 \pm 0.02) \times 10^{-4}$	1.50

Research into OPV materials has recently been focused also on improving the photostability of semiconducting polymers. To address this concern, the photostability of the fabricated devices is examined by placing the polymer films under 1 sunlight illumination in a solar simulator. The normalized PCE, J_{sc} , V_{oc} and FF of the reference/15% (v.v) RGO ternary devices versus the photodegradation process are presented individually in Figure 7.27a-d, respectively. Photodegradation process carried out till the 70% of PCE for each device and then the PV parameters were examined. After 1000 min of illumination by 1 sun in air, it is clearly observed that the addition of RGO into the binary active layer, improves the stability of the OPV devices as compared to the reference. It is obvious that the ternary needed more than double time to degrade to the 70% of its initial PCE reported value, compared to the reference (Fig. 7.27a). At 400min both reference and ternary seemed to have almost 95% of J_{sc} value (Fig. 7.27b). On the contrary at 400min, the reference cell seemed to have 85% of its V_{oc} , but the ternary was at 90% of its initial V_{oc} calculated value. Last at the same time period, FF was almost 86% and 92% for the reference and the ternary cell, respectively.

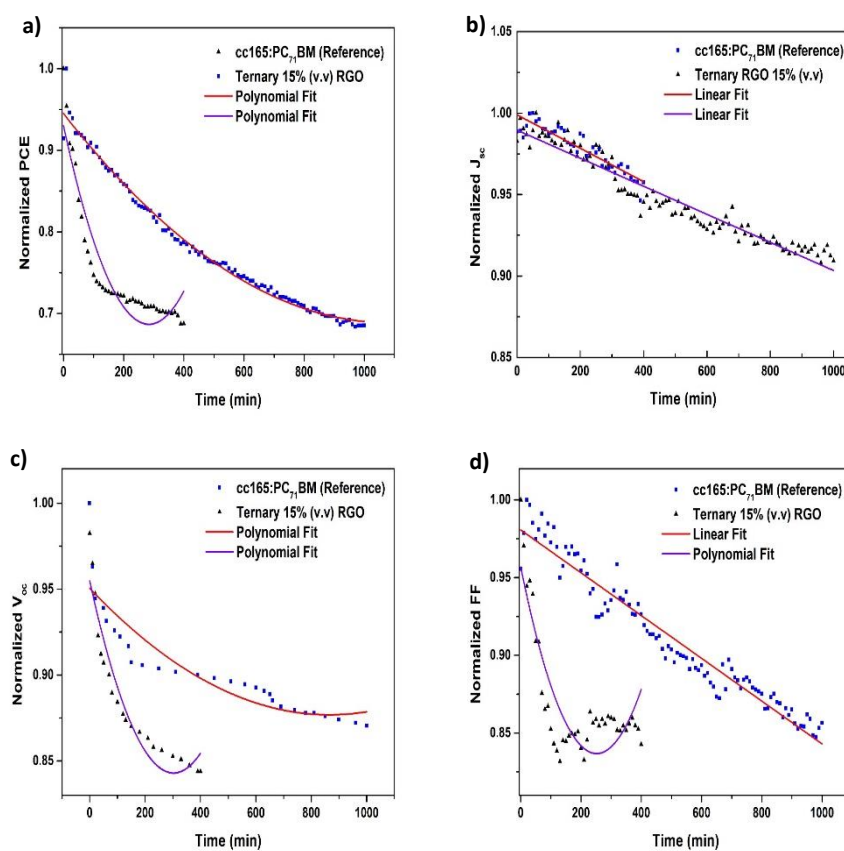


Figure 7.27 Photo-stability of reference:PC₇₁BM and Ternary 15% (v.v) RGO: PC₇₁BM solar cells (under AM1.5 illumination at 1 sun) for 1000min.

Finally, an AFM morphology measurement carried out and the outcome was really promising, as transition from the reference to the ternary 15% (v.v) RGO cell improved the morphology at almost 13%. This indicates that in case of the ternary cell, there is a more homogeneous film, which ensures the FF improvement of the ternary cell.

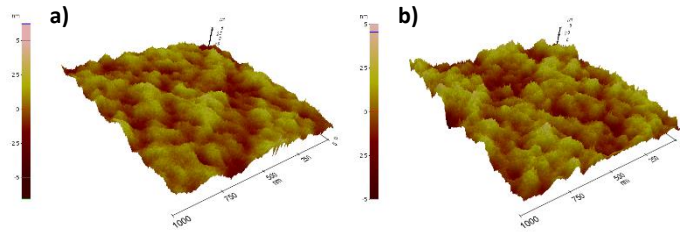


Figure 7.28 AFM images of **a)** reference and **b)** ternary device. The roughness for the reference is 1.133 nm, where for the ternary device there is a significant decrease at 1.003 nm.

Chapter 8: Conclusions

In summary, a lot of information about OSC history and present research was demonstrated in this thesis, divided in three different projects. As well, an extensive report was made about 2D materials and why it is beneficial to use them as an additive in the AL of a BHJ solar cell, forming a ternary solar cell. Furthermore, a lot of information presented about the hot area of LBG and small molecule polymers and how their important properties could be implemented in OSC technology. A highly efficient ternary blend OPV device is developed with the incorporation of solution processed WSe₂ flakes as the additive material into the PTB7:PC₇₁BM binary device. A maximum PCE of 8.78% was achieved with the incorporation of M-WSe₂ flakes having lateral size in the 30-50 nm range, which is one of highest PCE reported for OPVs with PTB7 as the polymer donor. The enhancement in PCE with respect to the standard PTB7:PC₇₁BM binary device (PCE=7.54%) is primarily due to synergistic effect of absorption and charge transfer processes. Excitons can also be generated inside the M-WSe₂ nanoflakes, increasing the overall exciton generation due to the complementary absorption bands of PTB7 and WSe₂ (Two-donors system). Also, the addition of the low dimensional WSe₂ flakes provides additional interfaces for exciton dissociation, as well as multiple routes for charge transfer, giving rise to enhanced exciton dissociation and electron mobility which is mainly observed in the S- and L-WSe₂ based devices. Those results demonstrate that solution processable 2D crystals could be a useful platform for their implementation as third components in ternary structures in order to significantly boost the PV performances of OPV devices. Next, a conjugated small molecule 4,7-dithienbenzothiadiazole (T) was incorporated as the third component inside PTB7:PC₇₁BM binary active layer indicating a 5.5% PCE improvement, reaching 8.11%. The enhancement in PCE with respect to the standard PTB7:PC₇₁BM inverted binary device (PCE=7.69%) is primarily due to synergistic effect of absorption and charge transfer mechanism. Also, the addition of small molecule T provides additional interfaces for exciton dissociation, as well as multiple routes for charge transfer, giving rise to enhanced exciton dissociation and electron mobility. Therefore, the prospect of small molecule-based OSCs is a very promising area of OPVs, which could further improve the PV performances of OPV devices. Five different LBG polymers, were studied also for the first time as the electron donor materials while PC₇₁BM was the acceptor. Among them cc72 presented the higher PV parameters but still the J_{sc} value was not favorable for the application above a perovskite layer, forming an integrated device. Therefore, another LBG polymer, cc165, from the same category was incorporated, as it presents higher J_{sc} values. The ternary 15% (v.v) RGO (cc165:15%(v.v)RGO:PC₇₁BM) was 8.5% more efficient than the reference (PCE=4.14%), reaching almost 4.5%. The goal of increased conductivity was achieved with the incorporation of RGO in the binary active layer cc165:PC₇₁BM reaching almost 55% and 60% improvement for 15% and 20% (v.v) RGO respectively, in respect to the reference.

Chapter 9

9.1 Present research

A part of our present research in our group is focused on the fabrication of a hybrid solar cell, consisting of a planar perovskite layer as the higher band gap material and an organic material, cc165:RGO:PC₇₁BM, as the lower band gap material. The goal in this project is to overcome the efficiencies of the current perovskite SCs reached in our lab, which reaches almost 17%.

9.2 Recommendations for future work

The research that has been undertaken for this thesis has highlighted a number of topics on which further research would be beneficial. As:

- Use of more efficient LBG polymers with broader absorption range (IR).
- Incorporation of other RGO derivatives in order to further enhance the OSC conductivity.

Chapter 10

10.1 List of Publications

M. Sygletou, **P. Tzourmpakis**, C. Petridis, D. Konios, C. Fotakis, E. Kymakis, E. Stratakis, *Laser induced nucleation of plasmonic nanoparticles on two-dimensional nanosheets for organic photovoltaics*, J. Mater. Chem. A, 2016, 4, 1020-1027.

C. Petridis, D. Konios, M. M. Stylianakis, G. Kakavelakis, M. Sygletou, K. Savva, **P. Tzourmpakis**, M. Krassas, N. Vaenas, E. Stratakis, E. Kymakis, *Solution processed reduced graphene oxide electrodes for organic photovoltaics*, Nanoscale Horiz., 2016, 1, 375-382.

G. Kakavelakis, A. E. Del Rio-Castillo, V. Pellegrini, A. Ansaldo, **P. Tzourmpakis**, R. Brescia, M. Prato, E. Stratakis, E. Kymakis, F. Bonaccorso, *Size-Tuning of WSe₂ Flakes for High Efficiency Inverted Organic Solar Cells*, ACS Nano, 2017, 11, 4, 3517–3531.

C. Chochos, A. Katsouras, S. Drakopoulou, C. Miskaki, M. Krassas, **P. Tzourmpakis**, G. Kakavelakis, C. Sprau, A. Colsmann, B. Squeo, V. Gregoriou, Emmanuel Kymakis, A. Avgeropoulos, *Effects of alkyl side chains positioning and presence of fused aromatic units in the backbone of low-bandgap diketopyrrolopyrrole copolymers on the optoelectronic properties of organic solar cells*, Eur. Polym. J., (Submitted).

10.2 Presentations in Conferences

- Participation in International Conference: HINT Annual Meeting: “Nanostructured Hybrid Materials II: reinforced 3D structures, smart composites, self-healing”, “WS₂ nanosheets decorated with Au nanoparticles (NPs) and their incorporation in Ternary Organic Photovoltaics (OPVs)”, P. Tzourmpakis, Constantinos Petridis, Emmanuel Stratakis, Emmanuel Kymakis, 22-24 April 2015, Agapi Beach Hotel, Heraklion, Crete (**Poster**)
- Participation in International Symposium: 6th International Symposium on Transparent Conductive Materials, “Ternary organic solar cells incorporating 2D materials”, P. Tzourmpakis, M. M. Stylianakis, D. Konios, C. Petridis, E. Kymakis, 09-13 October 2016, Chania, Crete (**Oral Presentation**)